Structure and Mechanics of Membrane-bound Vimentin Filaments and Networks under Strain

DISSERTATION

for the award of the degree

Doctor rerum naturalium

of the Georg-August-Universität Göttingen

within the doctoral program Chemistry

of the Georg-August University School of Science (GAUSS)

submitted by

Sarmini Nageswaran
born in Seesen

Göttingen 2022

Members of the Thesis Committee

Prof. Dr. Claudia Steinem
Institute for Organic and Biomoleculare Chemistry
Georg-August University Göttingen
& Max-Planck Institute for Dynamics and Self-Organization Göttingen

Prof. Dr. Sarah Köster
Institute for X-Ray Physics
Georg-August University Göttingen

Members of the Examination Board

First referee: Prof. Dr. Claudia Steinem
Institute for Organic and Biomoleculare Chemistry, Georg-August University Göttingen
& Max-Planck Institute for Dynamics and Self-Organization Göttingen

Second referee: Prof. Dr. Sarah Köster
Institute for X-Ray Physics, Georg-August University Göttingen

Further Members of the Examination Board

Prof. Dr. Burkhard Geil
Institute for Physical Chemistry, Georg-August University Göttingen

Prof. Dr. Timo Betz
Third Institute of Physics - Biophysics, Georg-August University Göttingen

Prof. Dr. Bert de Groot
Max Planck Institute for Multidisciplinary Sciences

Prof. Dr. Kai Tittmann
Deptartment of Molecular Enzymology, Georg-August University Göttingen
& Max-Planck Institute for Multidisciplinary Sciences Göttingen

Date of Oral Examination: 29th August 2022

"Science [...] never solves one problem,
without creating ten more!"

-GEORGE B. SHAW

To my friends and family.

Contents

List of Figures v

List of Tables ix

1 Introduction 1
- 1.1 The Eukaryotic Cell . . . 1
- 1.2 The Biological Membrane . . . 2
  - 1.2.1 Structure of Biological Membranes . . . 2
  - 1.2.2 Mechanics of Biological Membranes . . . 3
- 1.3 The Cytoskeleton . . . 4
- 1.4 Intermediate Filaments as Main Determinant of Cell Architecture and Mechanics . . . 6
  - 1.4.1 Structure of Intermediate Filaments . . . 6
    - 1.4.1.1 The Secondary Structure of all Intermediate Filaments . . 7
    - 1.4.1.2 Assembly of Intermediate Filaments . . . 8
  - 1.4.2 Mechanical Properties of Intermediate Filaments . . . 9
- 1.5 Vimentin Intermediate Filaments . . . 10
  - 1.5.1 Structural Organization of Vimentin Intermediate Filaments . . . 10
  - 1.5.2 Mechanical Properties of Vimentin Intermediate Filaments . . . 11
  - 1.5.3 *In vitro* Vimentin Filaments and Networks . . . 12

2 Scope 15

3 Materials and Methods 17
- 3.1 Materials . . . 17
  - 3.1.1 Polydimethylsiloxane . . . 17
  - 3.1.2 Uniaxial Motorized Stretching Device . . . 20
  - 3.1.3 Lipids . . . 21
  - 3.1.4 Fluorophores . . . 22
  - 3.1.5 Beads . . . 23
  - 3.1.6 Vimentin Intermediate Filament . . . 24

3.2 Preparative Methods 26
  3.2.1 Preparation of Polydimethylsiloxane Chambers 26
  3.2.2 Preparation of Small Unilamellar Vesicles 27
  3.2.3 Preparation of Vimentin Intermediate Filaments 28
    3.2.3.1 Labeling of Vimentin Monomers with ATTO647N and Biotin Maleimide 28
    3.2.3.2 Dialysis of Vimentin into Low Salt Buffer 29
    3.2.3.3 Assembly of Vimentin Tetramers 29
3.3 Biosensing Methods 31
  3.3.1 UV/vis Spectroscopy 31
3.4 Biophysical Methods 33
  3.4.1 Confocal Laser Scanning Microscopy 33
    3.4.1.1 Airyscan Microscopy 35
    3.4.1.2 Fluorescence Recovery After Photobleaching 37
  3.4.2 Atomic Force Microscopy 41
    3.4.2.1 Force Distance Curves 42
    3.4.2.2 Quantitative Imaging Mode 44
3.5 Data Evaluation and Processing 47
  3.5.1 Beads Evaluation 47
  3.5.2 Digital Image Correlation 48
  3.5.3 Determination of Contour and Apparent Persistence Lengths 51
  3.5.4 Theoretical Strain Displacement 52
  3.5.5 Segmentation of Vimentin Intermediate Filaments 53
  3.5.6 Pixel-wise Height Distribution 54

4 Results **57**
4.1 Characteristics of Uniaxial Stretching 58
4.2 Supported Lipid Bilayer under Strain 62
  4.2.1 Sliding and Sticky Membranes: A Study by Varying the Plasma Exposure 62
  4.2.2 Supported Lipid Bilayer under Strain Using Lipid Reservoir 67
4.3 Supported Membrane-bound Vimentin Intermediate Filaments under Strain 70
  4.3.1 Stretching of Membrane-bound Vimentin Intermediate Filaments Dependent on the Stretching Speed 70
  4.3.2 Stretching of Membrane-bound VIFs Dependent on the Pinning Point Density 72
  4.3.3 Reorientation of Membrane-bound VIFs during Stretching 75
4.4 Membrane-bound Vimentin Intermediate Filament Networks under Strain 78

4.4.1 Structure of Membrane-bound VIF Networks 78
4.4.2 Orientational Changes of Membrane-bound VIF Networks under Strain 80
4.5 Influence of Vimentin Intermediate Filaments and Networks on Lipid Bilayer 82

5 Discussion **87**
5.1 Anisotropic Stretching 88
5.2 Lipid Bilayers under Strain 91
5.2.1 Diffusive Reorganization of Lipids in the Lipid Bilayer 91
5.2.2 Excess of Membrane Area 92
5.3 Vimentin Intermediate Filaments under Strain 96
5.3.1 Properties and Interactions of the Membrane-bound VIF Networks 96
5.3.2 Mechanical Response of VIF Networks to External Strain 97
5.3.3 Mechanical and Entropic Contributions of Single VIFs to VIF Networks upon Stretching 98
5.4 Comparison to IF Networks in Cells 104

6 Summary and Outlook **109**

Bibliography **111**

A Appendix **I**
A.1 Amino Acid Sequence of the Cysteine Mutant of Vimentin Monomer . . . I
A.2 List of Symbols and Abbreviation II
A.3 List of Chemicals and Consumables VIII
A.4 List of Devices and Softwares IX

List of Figures

1.1 Schematic drawing of an eukaryotic cell. 1

1.2 Schematic drawing of a biological membrane. 3

1.3 Schematic drawing of the cytoskeleton in a cell. 4

1.4 Schematic representation of the rim-and-spoke organization of intermediate filaments. 7

1.5 Schematic illustration of the hierarchical assembly of intermediate filaments 9

1.6 Schematic representation of vimentin dimer and tetramer. 11

3.1 Chemical structure of the elastomer polydimethylsiloxane. 17

3.2 Hydrosilylation reaction scheme. 18

3.3 Detailed hydrosilylation mechanism proposed by CHALK and HARROD. . . 19

3.4 Oxygen plasma treatment of the polydimethylsiloxane surface. 20

3.5 Motorized uniaxial stretching device for lateral stretching of the membrane-bound vimentin intermediate filaments on PDMS. 20

3.6 Basic structure of lipids used to prepare solid-supported membranes on PDMS. 21

3.7 Structural scaffold of the fluorophores used to label the vesicles and vimentin protein. 23

3.8 Example fluoroscence micrograph of the blue beads (4 µm) 24

3.9 Mechanism of the MICHAEL-addition reaction. 25

3.10 Schematic drawing of the polydimethylsiloxane chamber used in this work. 26

3.11 Principle of confocal laser scanning microscopy. 35

3.12 Principle of airyscan microscopy. 36

3.13 Principle of fluorescence recovery after photobleaching (FRAP) to measure lateral diffusion of fluorescently labeled molecules. 38

3.14 Principle of the atmoic force microscopy (AFM). 42

3.15 Schematic representation of a typical force distance (FD) curve. 44

3.16 Schematic illustration of the quantitative imaging mode. 45

3.17 Electromicrographs of the cantilever used in this work. 46

3.18 Detection of beads (4 µm) by cellpose. 47

3.19 Steps of a digital image correlation (DIC) algorithm. 48
3.20 Scheme to find the initial guess. 50
3.21 Determination of the apparent persistence lengths of membrane-bound vimentin intermediate filaments based on Easyworm. 52
3.22 Segmentation of the filaments in the unstretched and stretched states. . . 53
3.23 Basic steps of the analysis of the pixel-wise height distribution of vimentin intermediate filament networks attached to the lipid bilayer. 55

4.1 *In vitro* experimental system. 57
4.2 Characteristic of uniaxial stretching. 59
4.3 Confocal fluorescence micrographs of the small beads. 60
4.4 Characteristics of uniaxial stretching using small bead size. 61
4.5 Sticky lipid bilayer under strain. 66
4.6 Behavior of polymethylsiloxane-supported lipid bilayers in the presence of lipid reservoir. 68
4.7 Supported lipid bilayers under strain in the presence of lipid reservoir. . . 69
4.8 Stretching of membrane-bound vimentin intermediate filaments (VIFs). . 71
4.9 Stretching of membrane-bound vimentin intermediate filaments (VIFs) connected by labeled neutravidin. 73
4.10 The strain of membrane-bound vimentin intermediate filaments in dependence of the biotin concentration within the filaments. 74
4.11 Theoretical displacements of contour of exemplary filaments by applying strain. 75
4.12 Persistence and contour lengths of membrane-bound vimentin intermediate filaments. 76
4.13 Analysis of the reorientation of membrane-bound vimentin intermediate filaments upon stretching. 77
4.14 Structure of membrane-bound vimentin intermediate filament networks. 79
4.15 Orientation analysis of membrane-bound vimentin intermediate filament networks under strain. 80
4.16 Lipid bilayer vs lipid bilayer with VIFs vs lipid bilayer with vimentin intermediate filament networks. 82
4.17 Relaxation of strained lipid bilayer. 83
4.18 Diffusion coefficient and mobile fraction determined by performing fluorescence recovery after photobleaching experiments. 84

5.1 Different Strain Definitions. 89
5.2 Proposed fusion mechanism. 94
5.3 Force-Strain curves of membrane-bound vimentin intermediate filaments.100

5.4 Reorientation of vimentin intermediate filaments by diffusive reorganization of lipids. 101
5.5 Contribution of vimentin intermediate filaments to VIF network. 103
5.6 Membrane-bound vimentin intermediate filaments networks under strain.106

List of Tables

3.1 Lipid composition for preparation of lipid bilayers. 27
3.2 Composition of vimentin buffer used in this work. 27
3.3 Composition of labeling buffer and storage buffer used in this work. 28
3.4 Composition of dialysis buffer and dilution buffer used in this work. 29
3.5 Composition of assembly buffer used in this work. 30
3.6 User settings for the microscopy to study the membrane-bound vimentin filaments and networks under strain. 37
3.7 User settings for the microscopy to study the mobility of the membrane. . 41

4.1 Confocal fluorescence micrographs of lipid bilayers on polymethylsiloxane treated with different plasma conditions in the unstretched and stretched states. 63
4.2 Mean diffusion coefficients and mobile fractions determined on different systems by fluorescence recovery after photobleaching experiments. . . . 85

Abstract. The shape and mechanical properties of eukaryotic cells are determined by the cytoskeleton, composed of actin filaments, microtubules and intermediate filaments (IFs). Among these, IFs are considered to be the main determinants of cell stiffness and strength. The reason for this is that they can withstand much larger deformations than the other two filament classes. Previous studies have revealed a rim-and-spoke arrangement of IFs, suggesting that they are involved not only in the mechanical stability of the cytoplasm but also of the plasma membrane. Therefore, the organization of IFs at the plasma membrane and their influence on the mechanical properties of cells under a variety of strains are of great interest.

To mimic the rim arrangement at the plasma membrane under strain, the aim of this work was the development of an *in vitro* model system, with focus on the membrane-bound vimentin intermediate filaments (VIFs) that allows for uniaxial stretching. To investigate the rim arrangement, an elastic solid support, namely polydimethylsiloxane (PDMS), was used to enable lateral stretching of the composite system due to its molecular flexibility. The hydrophobic PDMS with embedded fluorescent beads was oxidized to render the surface hydrophilic, and by spreading small unilamellar vesicles (SUVs), a lipid bilayer was formed. The assembled VIFs coupled to ATTO647N and biotin were linked to the biotin-decorated lipid bilayer *via* a neutravidin linker. A lipid reservoir in the form of SUVs was added to provide the system with excess lipid material. Stretching of this composite system was achieved by a uniaxial motor-driven stretching device.

Performing stretching of individual membrane-bound VIFs revealed mechanical and entropic stretching. The former means that elongation of the filament's contour length upon stretching occurs, while for the latter pulling out the thermal fluctuations is observed. If the strain rate and pinning point density were increased, mechanical stretching rather than entropic stretching was increasingly observed. Additionally, the underlying lipid bilayer contributed to the reorientation of VIFs by diffusive reorganization or affected the strain transmission due to sliding and rupturing. The found properties of single membrane-bound VIFs might contribute to the mechanical response of membrane-bound VIF networks. Even though filaments in the networks mainly responded with entropic stretching, so far, there has been no access if mechanical stretching occurs or not. However, it can be speculated that the applied strains might be too low to observe mechanical stretching. In summary, an artificial model system was established that opens up a pathway to study the structural and mechanical properties of cytoskeletal components under strain in order to imitate the cell cortex in nature.

1 Introduction

1.1 The Eukaryotic Cell

The smallest basic structural and functional element of all organisms are cells. In terms of their properties and internal structure, they are divided into two classes: prokaryotic and eukaryotic cells. The former has no internal membranes, while the latter is equipped with unilamellar membranes that protect its internal organelles from external environmental influences. This compartmentalization provides well-defined areas for different activities and functions within the cell, making the structure more complex.[1] The maintenance and formation of different intracellular compartments, cell-to-cell communication, exocytosis, and endocytosis play important roles in cells. Major organelles embedded in the cytoplasm include the nucleus, which houses the DNA, and its surrounding endoplasmic reticulum for protein production, the Golgi apparatus for protein sorting, and the mitochondria as the cell's energy producers (cf. Fig. 1.1).[1,2] In addition, the structural stability of the cell, intracytoplasmic migration, and whole-cell migration are enabled by the cytoskeleton, consisting of actin filaments, microtubules, and intermediate filaments.[1,3]

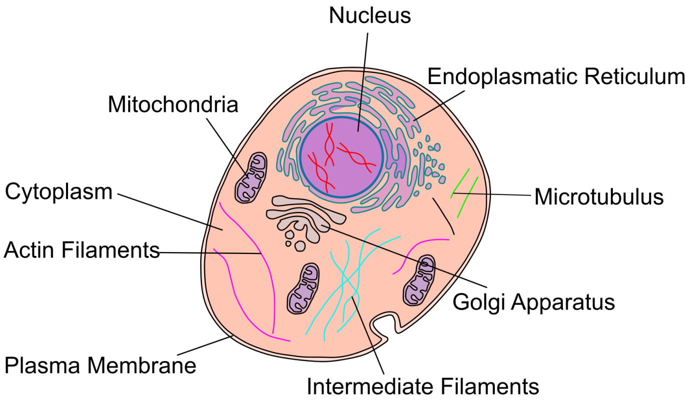

Fig. 1.1: Schematic drawing of a eukaryotic cell. It consists of a plasma membrane surrounding the cytoplasm, in which major organelles are embedded: nucleus, endoplasmic reticulum, Golgi apparatus, and the mitochondria. Moreover, microtubules, actin, and intermediate filaments ensure stability, transport, and migration. Inspired by ALBERTS *et al.*.[2]

1.2 The Biological Membrane

1.2.1 Structure of Biological Membranes

The basis for the formation of a living organism was the formation of biological membranes, which gives them an individual character by separating the cell interior from the external environment.[4,5] They are mainly composed of hundreds of different lipids, steroids, and proteins, although with different composition in the outer and inner leaflets.[3,5–7] Lipid bilayers with a thickness of about 5-10 nm[6–8] are the common structure of all cell membranes influenced by phase separation.[9] The plasma membrane is the most crucial membrane types, maintaining the internal environment of the cell and playing an essential role in intercellular communication.[10] Peripheral, and integral membrane proteins are responsible for various functions, such as communication, transport, and signal transduction.[3,8] According to SINGER and NICOLSON, biological membranes can be described as a "fluid mosaic" in which the individual lipid and protein molecules can move.[11,12] The extended version of this model is the so-called lipid rafts, which were developed on the basis of lateral heterogeneity and lipid segregation.[13,14] Rafts play an important role in cellular functions as they are small, heterogeneous, and highly dynamic domains.[13–15]

Membrane lipids belong to the family of large lipids, which have an amphiphilic character with a hydrophilic head group and a hydrophobic fatty acid chain. Depending on their molecular geometry, they spontaneously form micelles, vesicles, or bilayers in an aqueous environment. By forming vesicles or bilayers, the lipid molecules align themselves in such a way that the hydrophilic head groups face the water and form an interface (hydrophobic effect). On the other hand, the non-polar fatty acid chains interact with each other by displacing the water.[2,6] Although the hydrophilic head groups exhibit repulsive interactions, the coherence of the biological membrane is provided by hydrophobic interactions and noncovalent COULOMB and VAN DER WAALS interactions between the fatty acid chains. Phospholipids, which make up the bulk, glycolipids (mainly glycosphingolipids), and neutral lipids such as cholesterol form the main components of biological membranes.[3,6,10,11] A schematic drawing of a plasma membrane is presented in Fig. 1.2.

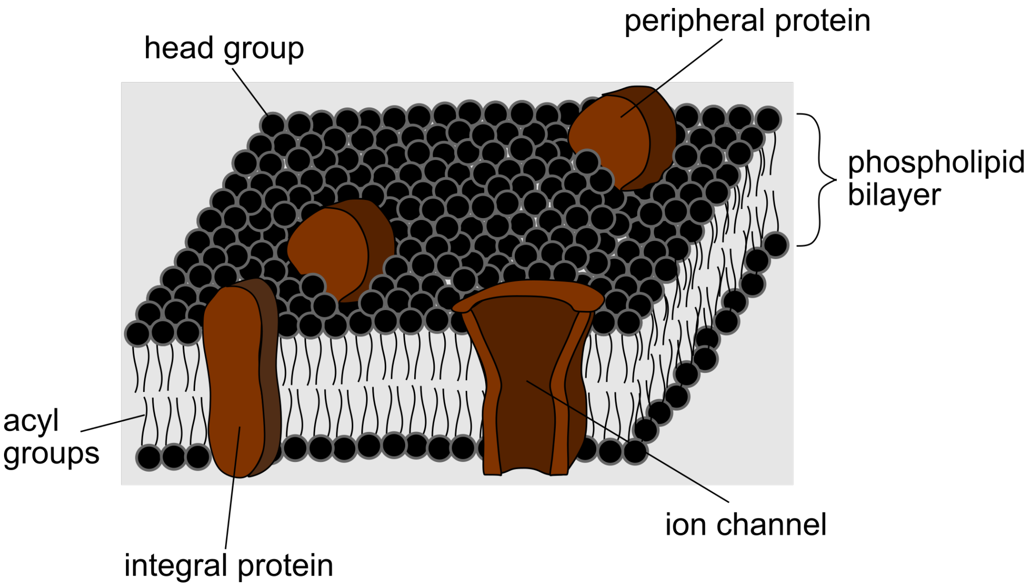

Fig. 1.2: Schematic drawing of a biological membrane. It consists predominantly of a phospholipid bilayer. The hydrophilic head groups are faced towards the aqueous compartments, whereas the hydrophobic acyl chains are enclosed in the interior of the bilayer. Peripheral and integral proteins allow for communication and transport. Adapted from MARTINAC *et al.*.[16]

To study the properties of biological membranes, a variety of well-defined artificial membrane systems (*e.g.*, vesicles and solid supported membranes) have been established in recent years. While lipid vesicles can be formed in aqueous solutions, solid supported membranes, by contrast, require solid support, a widely used model system that provides exceptional stability of formed bilayers.

1.2.2 Mechanics of Biological Membranes

In addition to forming a barrier between the cell interior and its environment, biological membranes mediate the cell's response to extracellular and intracellular mechanical forces.[17,18] Many biological processes, including growth, differentiation, exocytosis, and endocytosis, result in large deformations of the membrane itself by altering cell shape and structural integrity.[19] Because of its inelasticity when the plasma membrane is exposed to external stress, it responds by supplying lipid material to counteract the stress, leading to an area expansion. One process that contributes to area expansion is exocytosis by the fusion of vesicles into the plasma membrane to resist stress.[20,21] Mechanical properties of plasma membranes, which are essential in biological systems, include: YOUNG's modulus, bending rigidity, shear modulus, and viscosity. For example, membranes have a remarkably low shear modulus ($4\text{-}10 \cdot 10^{-3}$ Nm^{-1}) due to the fluidity of lipids, a high elastic modulus as a result of the inelastic property of bilayers, and a bending stiffness (10^{-19} Nm) influenced by protein-membrane and cytoskeleton-membrane interactions.[16,22]

1.3 The Cytoskeleton

Metazoan cells are highly complex and well organized to fulfill a variety of specialized functions that a disorganized unit of similar diversity can not perform.[23] They are able to change and maintain their shape during movement, growth, and cell division (*e.g.*, meiosis and mitosis).[24,25] As they are constantly exposed to external stresses, they have the outstanding ability to withstand mechanical forces and maintain their shape.[2] The molecular machinery responsible for cell shape and mechanics providing structure and organization is a complex, intertwined network system of filamentous polymers with regulatory proteins. It possesses high mobility and flexibility with viscoelastic behavior.[24,26] This cytoskeleton (cf. Fig. 1.3) consists of three main subsystems with specific functions in the cell - microtubules (MTs), actin filaments (AFs), and a group of polymers grouped as intermediate filaments (IFs).[2,24,25]

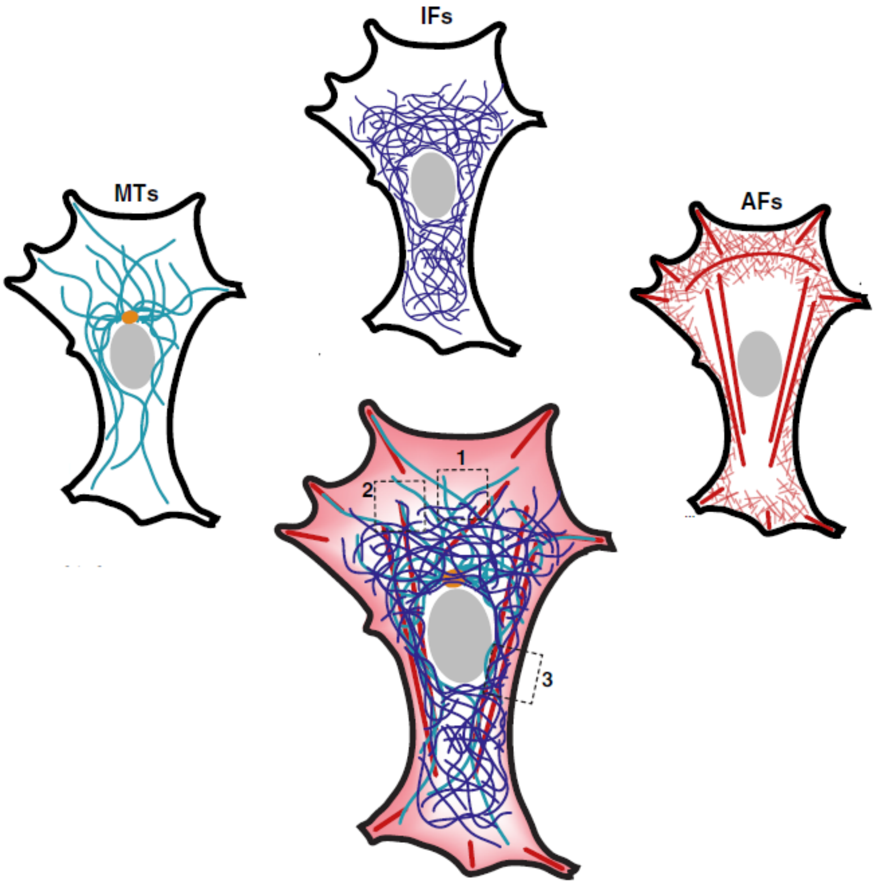

Fig. 1.3: Schematic drawing of the cytoskeleton in a cell with its structural components. This highly intertwined and dynamic network structure consists of microtubules, actin filaments, and intermediate filaments that have specific structural and mechanical functions in the cell. Adapted and modified from HUBER *et al.*.[24]

MTs enable directed transport of cargo through the cell *via* motor proteins, such as kinesin and dynein, and act as mechanical elements that can withstand pressure and compression.[2,26] They are the stiffest of all three cytoskeletal components, with a persistence length of more than 1 mm.[24,25] Dynamic instabilities caused by growth and shrinkage lead to rapid reorganization. In comparison, AFs, known as major contributors to cellular strength and cell shape during mitosis, have a persistence length of about 10 μm, making this polymer less stiff than microtubules.[2,25] However, the involvement of cross-links allows for the formation of highly organized, rigid structures, such as isotropic, bundled, or branched networks.[25] Depending on their localization, they form stress fibers, branched networks decorated with myosin II motors in the cell cortex, and protrusions such as bundled filopodia and lamellipodia.[26] Similar to MTs, AFs act as pathways for motor proteins (*e.g.*, myosin proteins) due to their polarity, which plays a key role in their organization.[25] In contrast to highly conserved MTs and AFs, IFs are known for their diversity and are, moreover, the softest with a persistence length of a few μm. Because of their flexibility, they are thought to dominate the mechanical response of the cell to large deformations as they can resist tensile forces better than compressive forces.[2,24–27] Some cell types, *e.g.*, airway epithelial cells, can form IFs in response to mechanical stress to resist shear stress.[25] Unlike MTs and AFs, IFs are incapable of transporting molecular motors due to their non-polar nature.[24,25]

All three cytoskeletal components have been found to interact directly by cross-linking, indirectly through biochemical signaling and gene regulation, and through non-specific steric interactions. For example, cross-talk can occur between MTs and IFs in the cell interior through cross-linking, direct physical contact, and molecular motors; between AFs and IFs at the periphery of an IF network *via* cross-linkers, direct binding, and motor proteins, and between MTs and AFs in the cell periphery through cross-links and AF- and MT-based motors.[24] When a cell with two present cytoskeletal components, *i.e.*, with an interpenetrating network (*e.g.*, AFs and IFs) is stretched, IFs appear to be load bearing[28], and thus protect the other network formed by AFs from rupturing. In contrast, AFs preferentially disassemble and fluidize.[29] The significant extensibility and stretchability of IFs allow them to serve as 'stress absorbers' and 'safety belts'.[30–32]

Compared to the other two filament components, IFs have not yet been adequately studied, although they are believed to be an important factor in cell stiffness and strength. However, their exceptional flexibility and mechanical stability are attracting increasing attention.[30–37]

1.4 Intermediate Filaments as Main Determinant of Cell Architecture and Mechanics

The human genome is enriched with 70 different IFs, which form one of the 100 most prominent gene families.[27,38] Their distinct expression during embryogenesis implies cell and tissue specificity with unique functions.[38–40] Thus, keratin IFs are expressed in epithelial cells, whereas vimentin IFs are expressed in mesenchymal, endothelial, and hematopoietic cells. IFs, such as desmin, synemin, and sycoilin, are mainly produced by myoblasts in muscle cells. Neuronal cells and nuclei mainly contain IFs constructed of α-internexin and neurofilament triplet proteins, and lamins, respectively.[39,40] Based on their structural similarities, IFs are classified into five different functional groups. The largest group of IFs is comprised of acidic (type I) and basic keratin (type II). Vimentin, desmin, and peripherin belong to type III IFs, which can form homopolymers. Type IV IFs include neurofilaments and α-internexin. The last group, type V IFs is predominated by lamins. In addition, some proteins have been discovered that can explicitly be categorized in the IF family based on their structure but cannot be classified into any of the categories mentioned earlier. Examples include two eye lens-specific proteins, nestin, phakinin, and filensin.[27,38,41–43]

Mutations in IF genes are associated with a variety of genetic diseases. Many features have been found to be responsible for their relevance to disease, including their dynamic properties, their involvement in cytoskeletal crosstalk, and their roles in signaling, mechanical stabilization, and motility. Mutagenic diseases associated with IF include *epidermolysis bullosa simplex* (keratin), dominant cataract (vimentin), and PARKINSON disease (neurofilament).[43–45]

1.4.1 Structure of Intermediate Filaments

In cells, IFs are organized in a rim-and-spoke arrangement adopted by QUINLAN *et al.*. They proposed that on the one hand, cytoplasmic IFs form radial spokes connecting cell-cell contact sites (*i.e.*, desmosomes) to the nucleus, while on the other hand, the circumferential rim runs parallel to the plasma membrane interconnecting desmosomal cell-cell junctions.[39] An illustration of the rim-and-spoke arrangement of an IF network is shown in Fig.1.4, of which the latter was suggested to contribute to the mechanical stability of the plasma membrane. Linker proteins that connect IFs to desmosomes include desmoplakins and plakoglobin. Their involvement results in an adaptive tension-spoke network that allows for the maintenance of the mechanical equilibrium. Consequently, force changes at the plasma membrane are sensed and transmitted to the nuclear compartment through a direct physical contact mediated by IFs. The distribution of radial spokes and circumferential rim varies depending on the cell type and function. In most of the cells, such as epithelial cells, radial spoke organization is common, while in other cell types, the circumferential rim is predominant.[39]

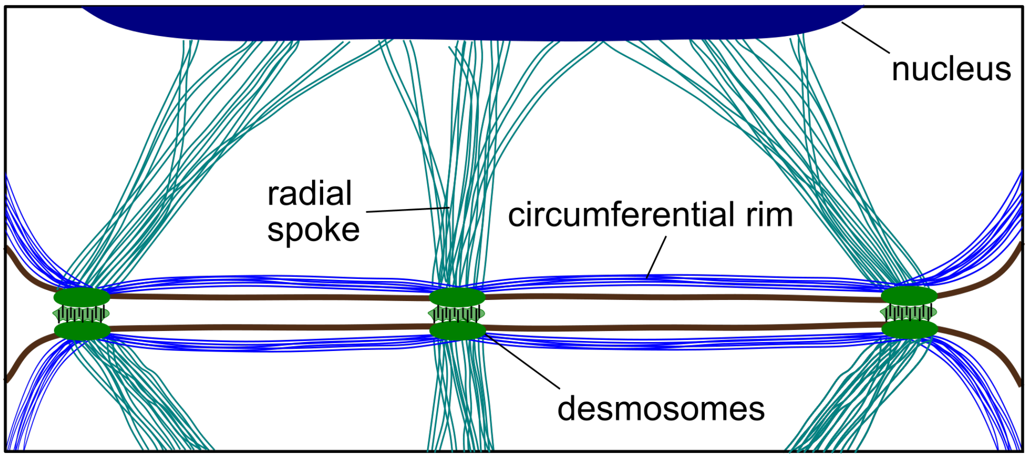

Fig. 1.4: Schematic representation of the rim-and-spoke organization of intermediate filaments (IFs). The cytoplasmic IF network consists of two distinct components: One forms the common radial spoke (blueish-green) that connects desmosomes (green) to the nucleus and contributes to nuclear stability. The other forms the circumferential rim (blue) near the plasma membrane (brown) that connects desmosomes *via* specific linker proteins. The rim contributes to the mechanical stability of the plasma membrane. Adapted from QUINLAN *et al.*.[39]

1.4.1.1 The Secondary Structure of all Intermediate Filaments

All IFs have a characteristic molecular blueprint of the secondary structure, which has a tripartite structure. They consist of a central α-helical rod domain (usually 45 nm[40,42]) flanked by unstructured, non-helical *N*- and *C*-terminal domains at the head and tail domains, respectively.[40–43,46–48] The amino acid (aa) sequence within the central rod domain is arranged in heptad repeats with the periodicity of seven residues in the forms of $(abcdefg)_n$. Positions *a* and *d* are turned out to be preferentially hydrophobic residues, such as leucine, methionine, or valine. This periodicity is interrupted by three linker domains L1, L12, and L2, which divide the structure into four α-helical segments, coil 1A, 1B, 2A, and coil 2B).[40–43,46,48] The number of amino acids in each helix is largely identical in all IFs, with coil 1A having 35 aa, coil 2A 19 aa, and coil 2B 115 aa, but the number of amino acids in coil 1B is IF-specific.[40,41,43] Another conserved feature is a discontinuity in the middle of segment 2B, which is an insertion of four additional residues into a continuous heptad repeat ("stutter").[40,48]

1.4.1.2 Assembly of Intermediate Filaments

Compared to the other two globular components of the cytoskeleton, IFs are self-assembling subsystems that do not require auxiliary proteins or factors such as adenosine triphosphate (ATP).[2,41,42,46,49] The basic building blocks of hierarchical IF self-assembly are polar, left-handed coiled-coil dimers formed by parallel and axially registered association of two single monomeric IF polypeptide chains.[41,42,46,49] Electro-microscopic studies revealed that the coil has a spacing of about 14 nm. Most IFs are able to form functional homodimers (*e.g.*, vimentin), while other IFs are not able to form functional homodimers but heterodimers (*e.g.*, keratin).[43,50] Under low-salt and physiological conditions, antiparallel, half-staggered 62 nm long A_{11} tetramers[41,51–53] are assembled, which is the smallest soluble oligomer found in cells. This antiparallel association of polar coiled-coil dimers leads to a non-polar arrangement of tetramers with *C*-terminal pendant tail domains.[41,48,49,54] The first phase include the lateral association of antiparallel tetramers leading to the formation of unit-length filaments (ULFs). These rod-shaped structures have an average length of about 60 nm and a diameter of 16-17 nm.[41,48,49,55] The number of dimers within a ULF can vary between IF, but generally consists of a central core of 32 coil 1 domains flanked by two segments of 16 coil 2 domains each.[53] The subsequent longitudinal annealing of the individual ULFs across coil 2 is a slow elongation phase in which short filaments are formed and further extended by an end-to-end association of these filaments.[40,41,49,56–58] In the third phase, radial compression of the filament diameter by 20% to 40% occurs, resulting in a matured, highly periodic filament of ~11 nm.[40,41,49,59] The diameter can vary from IF to IF and within one IF filament.[53,60,61] An overview of the three main stages of the assembly of IFs is illustrated in Fig. 1.5. *In vivo*, IFs continuously exchange between depolymerized IF subunits and fully polymerized IF proteins induced by phosphorylation,[62] which is achieved by reduced ionic strength *in vitro*.[63]

The role of the non-helical, unstructured head and tail domains in IF assembly has been widely discussed, and studies show no significant effects on IF assembly *in vitro*. However, the head domain has a major effect on IF structure during assembly[43,64–66], resulting in the formation of filaments containing fewer ULFs than usually observed or the formation of linear arrays of dimers or tetramers. In most of the IFs, the head domain appears to regulate lateral and end-to-end assembly, whereas the tail domain is involved in the control of lateral interactions.[43]

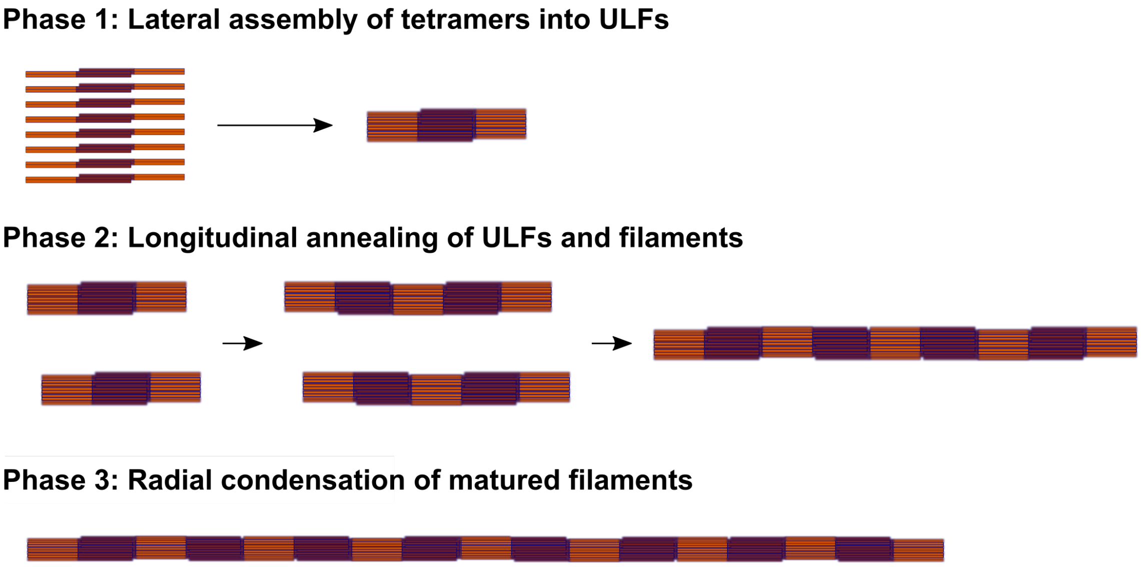
Phase 1: Lateral assembly of tetramers into ULFs
Phase 2: Longitudinal annealing of ULFs and filaments
Phase 3: Radial condensation of matured filaments

Fig. 1.5: Schematic illustration of the hierarchical assembly of intermediate filaments (IFs). The first phase is the formation of 60 nm long unit-length filaments (ULFs) by a lateral assembly of 62 nm long tetrameric subunits. In the second phase, the formed ULFs and short filaments are annealed longitudinally. Further elongation leads to mature μm long filaments. In the third phase, the IFs with a diameter of about 16 nm condense radially to a diameter of about 11 nm. Adapted from HERMANN*et al.*.[40]

1.4.2 Mechanical Properties of Intermediate Filaments

The mechanical properties of a cell are determined by the three components of the cytoskeleton.[24,35,67] However, these properties vary depending on the cell type, more precisely on the cytoskeletal subsystem involved and the external forces.[24] In contrast to AFs and MTs, IFs are thought to dominate cell mechanics at larger deformations because their flexibility allows them to withstand high stresses, tensile and compressive forces in cells.[24,67] At the level of a single filament, they can be stretched 2.6 to 3.5 times their original length, *i.e.*, 260-350 %, without rupturing.[24,30,31,68–71] In comparison, AFs and MTs tend to break at relatively low strains of less than 50 %.[24] These differences reflect the properties of the whole network: IF networks tend to be soft at low strains but can withstand much larger strains at large deformations, resulting in strain stiffening.[24,35] Therefore, IFs are essential in cells and tissues that are exposed to high stress and strain.[31,68,72] All IFs are mainly involved in the organization of cell organelles and mechano-transduction. IFs, such as lamins, maintain nuclear shape, and the increased stiffness of lamins protects the nucleus from deformation. Other IFs, such as keratin, vimentin, and desmin, increase mechanical integrity, regulate intracellular cell mechanics by stabilizing intracellular organelles by forming protective cages[72–77], and contribute to the stiffness of the cell cortex.[72]

1.5 Vimentin Intermediate Filaments

1.5.1 Structural Organization of Vimentin Intermediate Filaments

Vimentin intermediate filaments (VIFs) belong to the type III IFs that are very abundant in mesenchymal and endothelial cells.[39,40,78] Recent studies have led to a better knowledge of the structure of VIFs through atom-specific models of conserved segments. However, the exact organization of subunits within filaments remains not fully understood.[48,79–83] A vimentin monomer has a molecular weight of 57kDa and is 466 aa long, which consists of a central α-helical rod domain containing 310 aa, of which 70 aa are acidic, and 46 aa are basic. The coil 1 motif, which is the N-terminal part of the rod domain, is arranged in heptads, with every first and fourth residue being apolar. Its C-terminal part, the coil 2 motif, is organized in an 11-residue long repeats, with every first, fourth, and eighth residue being hydrophobic. The head domain is a 102 aa long sequence containing 12 arginine residues, making the head domain overall basic, while the tail domain comprises a 54 aa long sequence.[78] The periodic pattern of α-helical heptads and hendecads in the central rod domain enables the formation of coiled-coil homodimers by parallel alignment of the central coil 1 domains of two different vimentin filaments, as revealed by its crystallographic structure (cf. Fig. 1.6). Coil 1A and the subsequent linker domain are important for assembling the dimers into nonpolar tetramers of a length of 62 nm.[51–53] This is because the lysine residue of coil 1A at position 139 and the positively charged linker of one dimer interact with the negatively charged C-terminus of coil 1B of the other dimer. The two glutamic acid residues at position 191 of each filament are in a close neighborhood.[78,79] Subsequently, eight tetramers assemble laterally to form ULFs with a central core of 32 coil 1 domains and two segments of 16 coil-2 domains. The vimentin ULFs have a diameter of 16 nm with a length of 62 nm.[53] They anneal longitudinally across the coil-2 domains, resulting in molecular restructuring within each ULF. The interweaving of the overhanging ends of the ULFs within a matured filament results in a repetition of the structure every 43 nm.[84] The formation of short, mature filaments consisting of at least 2 ULFs is achieved by radial compaction, yielding the formation of vimentin filaments with a diameter of ~10 nm.[48,53,78,85] Thus, VIFs constructed from amino acid sequences with multiple coiled-coil domains are stabilized and linked by ionic and hydrophobic interactions.[78–80]

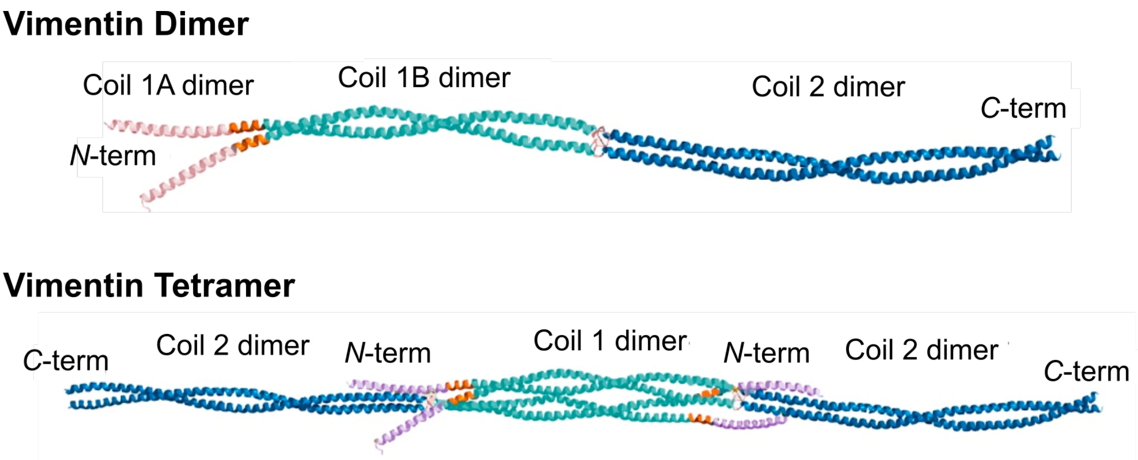

Fig. 1.6: Schematic representation of vimentin dimer and tetramer. The coiled-coil dimers are formed by parallel alignment of the central coil 1 domains (pink, orange, and green, *top*). Two dimers assemble into tetramers in such a way that the coil 1A (pink) with the positively charged linker (orange) of one dimer interacts with the negatively charged *C*-terminus of coil 1B (green) of the other dimer (*bottom*). Adapted and modified from DANIELSSON *et al.*.[78]

1.5.2 Mechanical Properties of Vimentin Intermediate Filaments

Previous studies in literature have shown that it is challenging to gain insights into the contributions of vimentin to cell mechanics, as different methods indicate that the results of vimentin perturbation are not consistent, *e.g.*, studies by ECKES *et al.*, WANG *et al.* and GUO *et al.*.[78,86–90] Nevertheless, studies have generally revealed that VIFs have multiple functions in cells. They have non-mechanical functions, such as GTPase signal transduction during wound healing, lipogenesis, sterol processing, promotion of nerve repair, and mediation of virus entry into host cells. Mechanical properties include cell mechanics, contractility, and protection of the nucleus during cell migration.[91]

VIFs are usually connected to the nucleus *via* the linker proteins plectin or nephrin-3[92] and form a cage-like network surrounding the nucleus, which is important for the transfer of mechanical forces from the cell cortex to the nuclear envelope. Studies in which the cell cortex was pulled demonstrated a deformation of the nucleus in the direction of stretch. The transfer of mechanical forces to the nucleus at small and large deformations occurs through VIFs.[77] During cell migration, the nucleus is subjected to extreme stresses that result in structural damage to the nucleus by *e.g.*, localized loss of the nuclear envelope integrity. Recently, researchers have reported that vimentin acts as a protector to keep the nucleus from rupturing.[77,93–96]

VIFs provide cells with a strain stiffening, rubbery, hyperelastic network that determines cell strength, extensibility, elasticity, and toughness.[88,89,94–96] Due to their high extensibility, VIFs maintain the elasticity of the cytoplasm under repeated stress. They improve cellular mechanical strength and toughness by slowing down viscoelastic relaxation, which reduces the risk of cell damage.[95] The cellular mechanical forces that VIFs are also able to resist are compressive and tensile forces associated with cell motility and shear forces generated by fluid flow at the surface of blood and airways. VIFs respond to shear forces with a rapid deformation of the networks, which implies a redistribution of intracellular forces. At low stress, they are adequately soft to allow deformation of the cells without the cytoplasm becoming excessively rigid or brittle. Under extreme stress, where AFs and MTs rupture, they respond by strain stiffening, preventing excessive deformation and further apoptosis, indicating the important role of VIFs in cell integrity, shape, and migration.[77,95] To the extent that VIFs contribute to cytoplasmic stiffness, they do not contribute significantly to cortical stiffness because the cytoplasm is much softer.[88,89,97]

1.5.3 In vitro Vimentin Filaments and Networks

The complexity of a cell makes it difficult to understand the contribution of VIFs to the overall cell mechanics because of the interaction of all three components of the cytoskeleton as well as motor and linker proteins. Thus, *in vitro* studies have been performed to separate them from AFs and MTs.[77] The stability of all IFs, including VIFs, to mechanical forces is attributed to the electrostatic interactions and hydrogen bonding between subunits within a filament, with interactions not only within the α-helical rod domain but also between N-terminus and α-helical coils.[48] *In vitro* strain experiments on individual VIFs using optical tweezers revealed a linear increase in force with increasing strain up to 10 %. With further increases in strain, the force remained constant, indicating a softening where a transition from the α-helix to the β-sheet occurs *via* random coils, followed by an increase in force, indicating a stiffening at strains above 50 %. Atomic force microscopy (AFM) experiments yielded similar results, but stiffening occurs at strains above 350 %, and the VIFs rupture when a force of 8 nN is applied.[30] This high extensibility has been observed in various experiments.[30,31,69–71] AFM experiments, in which vimentin dimers were pulled with a cantilever, showed that the response to strain was comparable to the one of the whole filament, demonstrating the relevance of the dimers as a reactor for mechanical forces. The transition from the α-helix to the β-sheet *via* random coils results in elongation of the contour length, with the amino acids still hydrogen-bonded, leading to large strains, as shown by wide-angle X-ray scattering (WAXS), RAMAN spectroscopy, and molecular dynamics simulations.[37,68,98–100] MONTE-CARLO simulations of extension and retraction curves for vimentin reveal irreversibility of the β-sheet formation.[31,71] The YOUNG's modulus derived from the elongation experiments of vimentin dimers is in good agreement with the those determined for the elongation of the whole filament. This result indicates that the filament responds to strain at small deformations by distributing the forces among all dimers.[77] The stretching response is also accompanied by sliding, which was shown by further *in vitro* experiments.[31,55,101,102]

The mechanical properties of the reconstituted *in vitro* VIF networks are commonly shown by rheological experiments.[33,34,103] By measuring the shear modulus at deformation with a constant strain and subsequent application of a small oscillating strain, it was found that vimentin networks exhibit lower shear modulus at low strains, but show an increase in shear modulus with increasing strain, indicating strain stiffening, consistent with the role in cell integrity. By sharp contrast, actin networks exhibit the highest stiffness, fluidizing at strains above 20 %.[33] Further *in vitro* measurements revealed non-linear mechanical properties of reconstituted VIF networks with suppressed, transient[103–106], and permanent cross-linkers, with the peak modulus and breaking stress higher for permanent cross-linkers than for networks without cross-linkers, resulting in a higher network flow. The non-linear mechanical response is due to plastic deformation and entropic stiffening of a filament segment between cross-linkers, with the rheological response dominated by inelastic fluidization at a slow loading rate and mainly by entropic stiffening at a high loading rate.[33,35,36,104,105,107] Structural studies of vimentin networks using fluorescence and electron microscopy revealed different morphologies within a network, *e.g.*, parallel alignment of two filaments due to electrostatic interactions leading to bundling and thus increased stiffness.[108–110]

2 Scope

The cytoskeleton of mammalian cells forms a complex, interwoven network of a variety of interacting filamentous and regulatory proteins. One major group of cytoskeletal components are intermediate filaments (IFs). They show incredible functions in cells, providing cells with shape, strength, and mechanical stability, particularly at large deformations. On the single filament level, IFs can be stretched remarkably 260-350 %. Previous studies on the composition of IFs proposed a rim-and-spoke arrangement, suggesting that IFs are not only involved in the mechanical stability of the cytoplasm to protect the nucleus but also act directly at the plasma membrane, thereby contributing to its mechanical stability.

This work aims at investigating the structure and mechanics of vimentin intermediate filaments (VIFs) attached to a lipid bilayer to mimic the part of the rim-and-spoke arrangement at the plasma membrane. Due to the complexity of cellular systems, a minimal artificial model system will be established by pursuing a bottom-up approach. Therefore, VIFs bound to the lipid bilayer *via* biotin-neutravidin linkages will be prepared on elastic hydrophilic polydimethylsiloxane (PDMS) equipped with fluorescent beads as optical tracers. This composite system will be laterally stretched by a uniaxial stretching device. With this system in hand, the mechanical response of membrane-bound VIFs and VIF networks to external strains will be studied by confocal laser scanning microscopy and atomic force microscopy. First, the lipid bilayer on PDMS will be characterized to find the optimal condition for sticky lipid bilayers, which are required for stretching the membrane and filaments. Since a lipid bilayer can only be stretched 4-6 % without rupturing and significantly higher strains are necessary for vimentin stretching, lipid bilayers will be studied under strain in the presence of a lipid reservoir in the form of small unilamellar vesicles (SUVs). Once succeeded, the VIFs will be linked to the lipid bilayer using neutravidin. A uniaxial stretching will be applied, and the stretch-induced changes of membrane-bound VIFs in the presence of SUVs will be studied. Increasing the concentration of VIFs leads to network formation. The main goal is to address the question of how a uniaxial stretch alters the behavior of single VIFs and VIF networks attached to the bilayer and *vice versa*.

3 Materials and Methods

3.1 Materials

3.1.1 Polydimethylsiloxane

Polydimethylsiloxane (PDMS) (cf. Fig. 3.1), a silicone-based synthetic organic elastomer, is one of the most widely used polymers in biological and medical science because it offers advantages such as rapid processing, cost efficiency, chemical inertness, and optical transparency.[111–113] Due to its non-toxicity, cells can be easily cultured on it, and implants made of PDMS are well tolerated *in vivo* cells.[113] It is most commonly applied in microfluidics and soft lithography.[111–113] In this study, PDMS is used as a solid support for the preparation of an artificial model system.

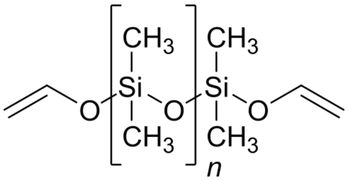

Fig. 3.1: Chemical structure of the elastomer polydimethylsiloxane.

PDMS consists of an inorganic siloxane backbone with organic methyl group attached to it.[112] Its flexibility at the molecular level due to flexible siloxane bonds gives PDMS mechanical properties without any mechanical failures (*e.g.*, bendability and stretchability).[111]

PDMS (Dow, Sylgard 184) was purchased from *Farnell GmbH* (Oberhaching, Germany) and supplied as a two-part kit: pre-polymer and curing agent. The pre-polymer is composed of dimethyl vinyl-terminated dimethylsiloxane (>60%), tetra(trimethyl siloxy)silane (1.0-5.0%) as well as dimethyl vinylated and trimethylated silica (30-60%). The curing agent contains dimethyl methyl hydrogen siloxane (40-70%), dimethyl vinyl-terminated dimethyl siloxane (15-40%), tetramethyl tetravinyl cyclotetrasiloxane (1.0-5.0%) as well as dimethyl vinylated and trimethylated silica (10-30%).[114] Furthermore, a catalyst, usually a platinum (Pt) species, such as KARSTED's catalyst, is supplemented in the curing agent, which accelerates the cross-linking process during the elastomer formation. [112,114]

Cross-linking occurs *via* a hydrosilylation mechanism, [111,114] in which a pre-polymer component (*e.g.*, dimethyl vinyl-terminated dimethyl siloxane or tetramethyl tetravinyl cyclotetrasiloxane) reacts with a component in the curing agent (*e.g.*, dimethyl methyl hydrogensiloxane) in the presence of the Pt catalyst (cf. Fig. 3.2). [114]

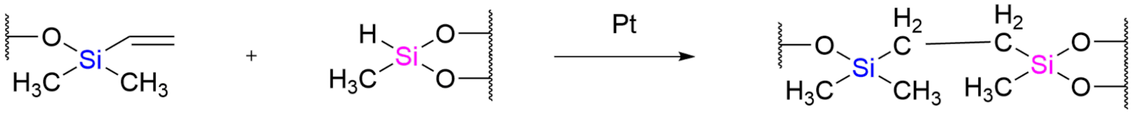

Fig. 3.2: Hydrosilylation reaction scheme. Polydimethylsiloxane is formed through a reaction of a pre-polymer component (*e.g.*, dimethylvinyl-terminated dimethylsiloxane) with a component in the curing agent (*e.g.*, dimethyl methyhydrogensiloxane). This reaction is catalyzed by an active platinum-catalyst. [111,114]

Fig. 3.3 shows an illustration of the detailed mechanism of platinum-catalyzed hydrosilylation proposed by CHALK and HARROD. [114,115] The first step is the reduction of an octahedral Pt(IV) species to the active catalyst, consisting of a square-planar Pt(II) species. This active Pt-catalyst coordinates to dimethyl vinyl-terminated dimethylsiloxane, resulting in the species **A**. Through an oxidative addition process of a dimethyl methyl hydrogensiloxane ($HSiR_3$) to species **A**, the intermediate **B** is formed, in which the Pt(II) is oxidized to Pt(IV) by cleavage of a Si-H bond to give species **C**. There is an equilibrium between the species **B** and the species **C**. After addition of SiR_3 to the species **B**/**C**, the product is obtained by reductive elimination. [114,115]

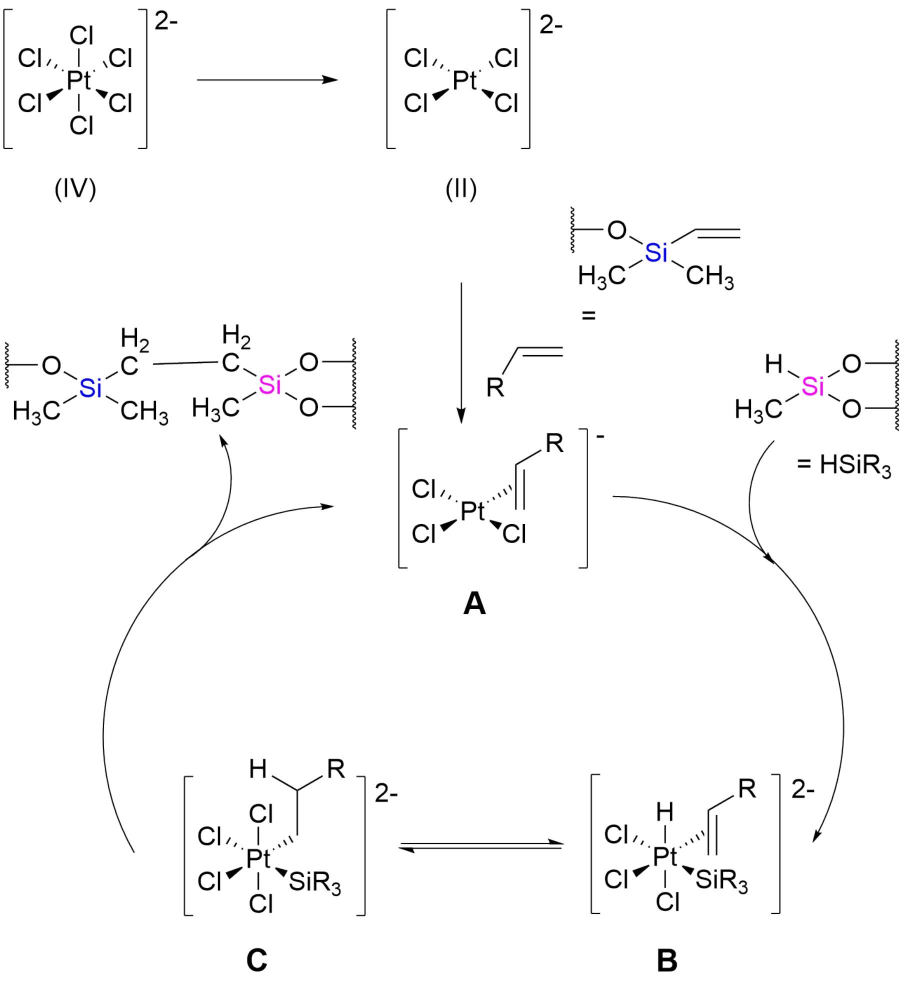

Fig. 3.3: Detailed hydrosilylation mechanism proposed by Chalk and Harrod. First, an octahedral Pt(IV) species is reduced to a square-planar Pt(II) species that coordinates the alkene to form the species **A**. In the next step, oxidative addition is carried out by adding $HSiR_3$ to give the species **B**, which is in equilibrium with the species **C**. After addition of SiR_3, the product (cf. 3.1) is obtained by a reductive elimination process.[114]

An important point to consider when selecting a suitable material is surface chemistry. PDMS is hydrophobic in an unmodified state, making it difficult to work with biological samples in aqueous solutions. Surface treatment with plasma oxidation renders the surface hydrophilic because of the silanol groups, which are formed during plasma treatment.[113] Delman *et al.* proposed a mechanism for the ultraviolet radiation-induced surface treatment with oxygen plasma (cf. Fig. 3.4).[116] However, the hydrophilicity of PDMS is stable for only 30 min before it changes back to hydrophobicity.[113] Roth *et al.* found by contact angle measurements that the recovery of hydrophobicity can be controlled by the conditions used for plasma treatment. The higher the plasma power and treatment time, the higher the driving force for the return to its original hydrophobicity after a certain storage time.[117]

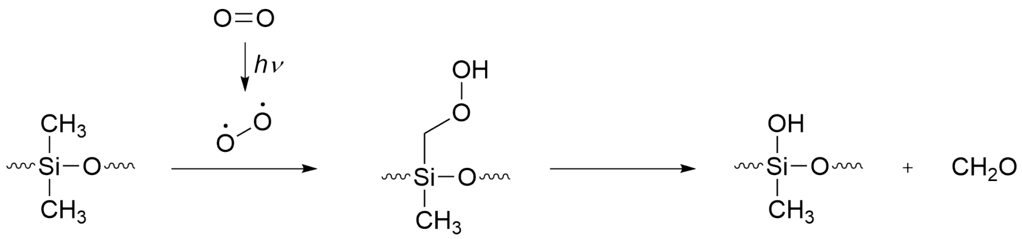

Fig. 3.4: Oxygen plasma treatment of the polydimethylsiloxane surface. This mechanism was proposed by Delman *et al.* in 1969. The methyl groups are oxidized by oxygen which is induced by ultraviolet radiation.[116]

3.1.2 Uniaxial Motorized Stretching Device

In order to stretch the PDMS-supported membrane-bound vimentin intermediate filament (VIF) system laterally, a uniaxial motorized stretching device was used (Fig. 3.5). The stretching device with the pre-stretching device was designed by Dr. Jonathan Bodenschatz (Institute for Physical Chemistry, Georg-August University Göttingen). The stretching device allows a maximum motor position (mp) of 10 mm without rupturing the PDMS chamber. The pre-stretching device with the fixed PDMS chamber is mounted on the stretching device. For atomic force microscopic measurements, an insert was constructed to close the hole in the center of the stretching device. To damp external vibrations, viscous glycerol was placed on the insert on which the PDMS chamber is placed.

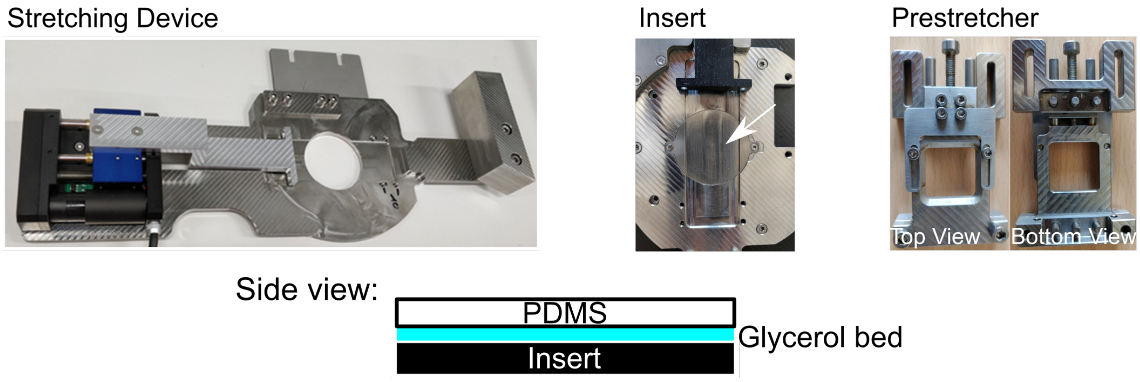

Fig. 3.5: Motorized uniaxial stretching device for lateral stretching of the membrane-bound vimentin intermediate filaments on PDMS. The stretching device allows a maximum motor position (mp) of 10 mm without tearing the substrate. The pre-stretching device with the PDMS chamber is mounted on the stretching device. For atomic force microscopic measurements, an insert was built to close the hole in the middle of the stretching device. A glycerol bed is placed between the PDMS chamber and the insert to dampen external vibrations.

For further details concerning the design of the stretching device, read the dissertation of Jonathan Bodenschatz.[118]

3.1.3 Lipids

Lipids are essential components of the plasma membrane, and in this study they are used to prepare artificial membranes on a solid support, PDMS. The prepared membrane consisted of 1-palmitoyl-2-oleoyl-*sn*-glycero-3-phospho-choline (POPC) and 1,2-dioleoyl-*sn*-glycero-3-phosphoethanolamine-*N*-(bi-otinyl cap) (DOPE biotin cap). All lipids were purchased from *Avanti Polar Lipids* (Alabaster, USA).

The matrix lipid POPC (cf. Fig. 3.6 A) is present in a large amount in this system and has no significant effect on protein attachment. It does not provide any charge. The basic element is glycerol, built up with a phosphatidylcholine as the head group (position *sn* 3) and esterified with a palmitic acid (16:0) at position *sn* 1 and an oleic acid (18:1, *cis*-Δ^9) at position *sn* 2.

DOPE-biotin-cap (cf. Fig. 3.6 B) is a receptor lipid whose head group, the phosphoethanolamine (position *sn*-3), is biotinylated and serves as a protein-binding lipid *via* a linker molecule neutravidin harboring four non-covalent binding sites for biotin. The positions *sn* 1 and *sn* 2 of the glycerol backbone of DOPE-biotin-cap are substituted with two oleic acids.

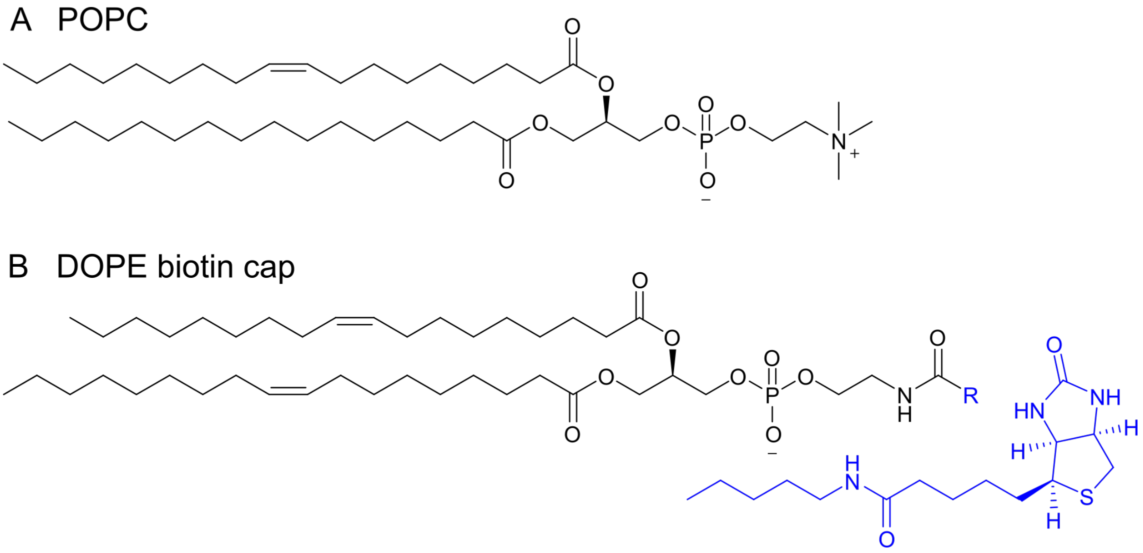

Fig. 3.6: Basic structure of lipids used to prepare solid-supported membranes on polydimethylsiloxane. (**A**) Schematic scaffold of 1-palmitoyl-2-oleoyl-*sn*-glycero-3-phosphocholine (POPC) used as a matrix lipid. (**B**) Structural scaffold of the receptor lipid 1,2-dioleoyl-*sn*-glycero-3-phosphoethanol-amine-*N*-(cap biotinyl) (DOPE-biotin-cap), which has a high affinity for the linker neutravidin.

3.1.4 Fluorophores

The purpose of using fluorophores is to visualize biological samples by means of fluorescence microscopy. Since the majority of these samples are not auto-fluorescent, the fluorophores must be implemented. In this project, the lipid-coupled fluorophore ATTO488 DOPE and the maleimide-coupled fluorophore ATTO647N maleimide conjugate were used, which were purchased from the company *Atto-tec GmbH* (Siegen, Germany).

ATTO488-DOPE (cf. Fig. 3.7 A) is a fluorophore that is bound to the DOPE. It is excited at λ_{abs} = 500 nm and the detection occurs at λ_{em} = 520 nm. It was used to label the small unilamellar vesicles (SUVs) that form the lipid bilayer by a spreading process and serve as a lipid reservoir. Due to its lower photostability, this fluorophore is suitable for experiments that require bleaching, such as determining the diffusion coefficient with fluorescence recovery after photobleaching (FRAP). ATTO657-DOPE (cf. Fig. 3.7 B) is a DOPE-coupled fluorophore that was used to label SUVs to form a lipid bilayer on PDMS. ATTO647-DOPE was primarily involved in experiments to study pure lipid bilayers under strain. It is excited at λ_{abs} = 647 nm and the detection occurs at λ_{em} = 667 nm.

ATTO647N-maleimide (cf. Fig. 3.7 C), a dye conjugated with a maleimide, has its excitation wavelength at λ_{abs} = 646 nm and emission wavelength at λ_{em} = 664 nm. It was employed to label vimentin monomers *via* MICHAEL addition (cf. Fig. 3.9). Due to its photostability, it is suitable for stepwise stretching experiments to visualize vimentin filaments over a certain period.

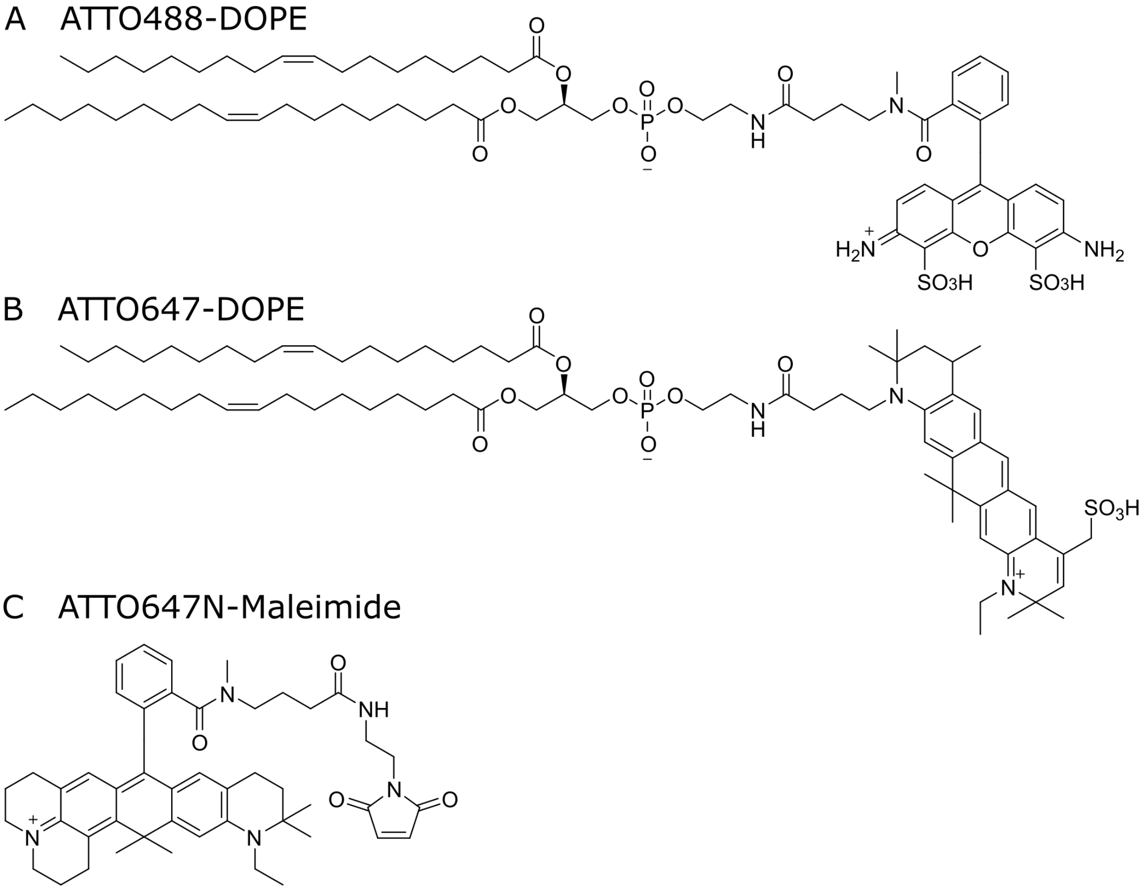

Fig. 3.7: Structural scaffold of the fluorophores used to label the vesicles and vimentin protein to visualize them by fluorescence microscopy. (**A**) Structure of ATTO488-DOPE incorporated into the small unilamellar vesicle to produce a lipid bilayer and to use them as a lipid reservoir. (**B**) Structure of ATTO647-DOPE integrated into the small unilamellar vesicle to produce a lipid bilayer for studies of pure lipid bilayers. (**C**) Structural framework of ATTO647N-maleimide conjugate used to label vimentin monomers by MICHAEL addition (cf. Fig. 3.9, chapter 3.1.6).

3.1.5 Beads

Fluorescent beads (blue, 4 µm) were placed between two PDMS films as an optical tracker during uniaxial stretching of membrane-bound VIFs or VIF networks on elastic PDMS support. The silica beads (cf. Fig.3.8) are excited at 354 nm, and detection occurs at 450 nm. The beads (PSi P4.0) are from *AttendBio Research* (Barcelona, Spain).

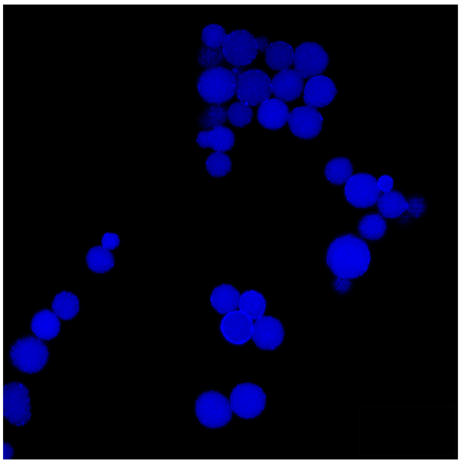

Fig. 3.8: Example fluoroscence micrograph of the blue beads (4 µm) embedded between two polydimethylsiloxane films of 100 µm thickness. They are used as optical tracker.

3.1.6 Vimentin Intermediate Filament

To study the structure and mechanical properties of VIFs under strain, the human vimentin mutant vimentin-C328NGGC was used within the scope of this work, in which the cysteine at the position 328 was replaced by asparagine. Two glycines and one cysteine were added at the *C*-terminal domain. The addition of a cysteine at the *C*-terminal end allows for labeling with the desired maleimide conjugate (ATTO647N or biotin) *via* a MICHAEL-addition. The labeling does not interfere with the assembly mechanism, which proceeds hierarchically in the presence of monovalent ions from vimentin monomers *via* tetramers and unit-length filaments to mature full-length filaments.[30] MICHAEL-addition, particularly the thiol-maleimide reaction, has gained much attention in bioconjugation chemistry. The general mechanism is shown in Fig 3.9. Initial deprotonation of the thiol group of the cysteine to form a nucleophilic thiolate anion, achieved by pH and a highly polar organic solvent, is followed by nucleophilic addition of the thiolate to the π-bond of the maleimide function of the fluorophore, forming an enolate. The desired fluorescently labeled species were obtained through keto-enol tautomerism.[119,120]

The vimentin mutant monomers were kindly provided by SUSANNE BAUCH with the group of PROF. DR. SARAH KÖSTER (Institute for X-ray Physics, Georg-August-University Göttingen).

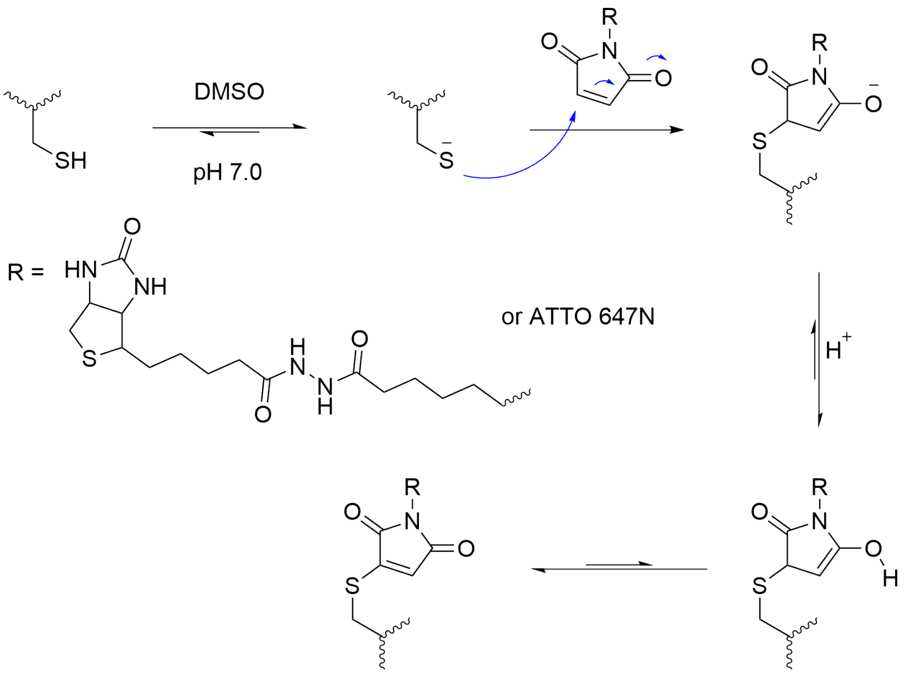

Fig. 3.9: Mechanism of the MICHAEL-addition reaction. The thiol group of the cysteine is deprotonated in the presence of a highly polar organic solvent. By conjugate addition, the thiolate group is added to the β-position of the maleimide function, forming an enolate. Keto-enol tautomerism leads to the main product, the ATTO647N or biotin-labeled vimentin monomer.[119,120]

3.2 Preparative Methods

3.2.1 Preparation of Polydimethylsiloxane Chambers

To stretch the membrane-bound VIFs or VIF networks, an elastic support was needed. Therefore, a PDMS chamber consisting of a thin film (2 cm x 2 cm x 200 µm) and a thick frame (5.5 cm x 2.5 cm x 0.5 cm) was made (cf. Fig. 3.10).

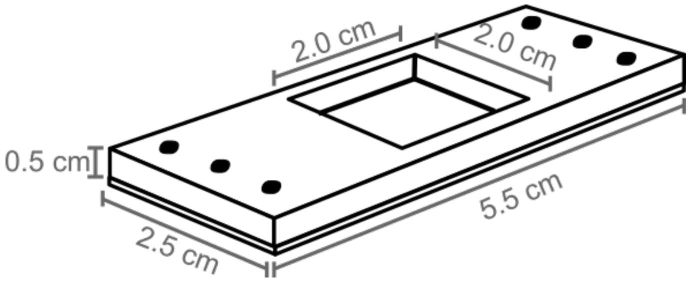

Fig. 3.10: Schematic drawing of the polydimethylsiloxane (PDMS) chamber used in this work. It consists of a thin PDMS sheet (2 cm x 2 cm x 200 µm) and a thick PDMS frame (5.5 cm x 2.5 cm x 0.5 cm).

To prepare the PDMS frame for the PDMS chamber, a mixture of base and curing agent (20:1 *w*/*w*) was degassed under vacuum for 30 min, followed by polymerization at 70°C for 1.5 h in an acrylic mold.

The thin PDMS film was prepared by mixing the base and curing agent at a weight ratio of 10:1 (*w*/*w*). This mixture was first degassed in an ultrasonicator for 5 min (45 kHz, degassing, 40 %) and then further degassed under vacuum for 25 min. After degassing, the mixture was uniformly spread on a silicon wafer coated with octafluorocyclobutane using a Spin Coat G3P-8 (*Specialty Coating Systems*, Indianapolis, USA) (800 rpm, ramp time: 10 s, dwell time: 30 s). The coated silicon wafer was polymerized at 70°C for 45 min to form the first thin film of PDMS. Fluorescent silica beads (blue, 4 µm) were deposited on the polymerized PDMS film (100 µm). For this purpose, the beads' suspension (7 µL) was dissolved in ultrapure water (1000 µL). Ultrasonic treatment was necessary to avoid aggregation. After application and spin coating, the remaining water was removed, followed by coating with a second PDMS film (100 µm) prepared analogously to the first thin film. Before polymerization of the second film at 70°C for 45 min, the PDMS frames were placed on the coated wafer with the beads in the center of the frame.

Due to its hydrophobic character, the PDMS surface had to be oxidized to become hydrophilic. Therefore, it was treated with oxygen plasma (100 %, 0.4 mbar, 20 %, 20 s)

by
Germany).

3.2.2 Preparation of Small Unilamellar Vesicles

SUVs, typically 100 nm in diameter, were used to prepare a lipid bilayer on hydrophilic PDMS. They were obtained by sonification.

The required lipid stock solutions (10-20 mg/mL) and the determination of the exact concentrations by LANGMUIR-BLODGETT trough were kindly performed by JUTTA GERBER-NOLTE (Institute for Organic and Biomolecular Chemistry, Georg-August-University Göttingen). The desired lipids dissolved in chloroform were combined in a test tube containing chloroform. The lipid compositions are given in Tab. 3.1. The lipid mixture was dispersed under nitrogen flow for 15 minutes and dried in vacuo for at least 3.5 h. The obtained thin lipid film was stored at 4°C until use.

Tab. 3.1: Lipid composition for the preparation of lipid bilayers on a solid support and use as a lipid reservoir. The lipid films used to apply a lipid bilayer contain biotinylated DOPE, the others do not.

	POPC	**DOPE biotinyl cap**	**ATTO488 [1]/ATTO647-DOPE [2]**
Bilayer	96 mol%	3 mol%	1 mol%
Lipid Reservoir	99 mol%	-	1 mol%

[1] for stretching experiments of membrane-bound VIFs, [2] for stretching experiments of lpid bilayer.

The prepared lipid films were hydrated with degassed vimentin buffer (500 µL, cf. Tab. 3.2). After 30 min incubation, they were mechanically shaken three times for 30 s with a rest period of 5 min. Finally, SUVs were formed by sonication (2 x 15 min, 4 cycles, 55-60 %) with an ultrasonic device (*Bandelin*, Berlin, Germany).

Tab. 3.2: Composition of vimentin buffer used in this work.

Composition	**Concentration**
NaH_2PO_4 (PB A)	2 mM
Na_2HPO_4 (PB B)	2 mM
KCl	100 mM
	pH 7.5

3.2.3 Preparation of Vimentin Intermediate Filaments

3.2.3.1 Labeling of Vimentin Monomers with ATTO647N and Biotin Maleimide

To visualize VIFs by fluorescence microscopy, the respective monomers were labeled with ATTO647N-maleimide. Biotinylation of the vimentin monomers was necessary to bind them to the membrane, which was also biotinylated, *via* neutravidin. Labeling with both was achieved by MICHAEL addition.

For this purpose, two different buffers were needed, one as a labeling buffer and one as a storage buffer (cf. Tab. 3.3).

Tab. 3.3: Composition of labeling buffer and storage buffer used in this work. The storage buffer is a low-salt buffer with a high concentration of urea to allow the protein to dissolve in aqueous solutions.

Labeling Buffer	**Storage Buffer**
NaH_2PO_4 (PB A, 50 mM)	NaH_2PO_4 (PB A, 2 mM)
Na_2HPO_4 (PB B, 50 mM)	Na_2HPO_4 (PB B, 2 mM)
Urea (5 M)	Urea (8 M)
pH 7.0	pH 7.5

Prior to the labeling procedure, vimentin monomers (approx. 1 mg/mL, 1 mL per label) dissolved in storage buffer were dialyzed against labeling buffer overnight at 4°C in a dialysis tube (50 kDa cutoff). Bio Gel P-30 media (3 g, *Bio-Rad Laboratories*, Hercules, USA) were hydrated overnight in labeling buffer (54 mL) to separate small from big beads.

The concentration of dialyzed vimentin solution was adjusted to 1 mg/ml. To this solution, a 20-fold excess of the corresponding maleimide conjugate in DMSO (20 µL, 10 mM) was added portionwise and mechanically shaken for 30 s, with an incubation time of 5 min, followed by incubation for 2 h under light exclusion. Afterwards, a L-cysteine solution was added (100 µL, 1 M) to bind free maleimide conjugates, succeeded by incubation maintained for 1 h. The reaction mixture was purified by size exclusion chromatography on a column filled with Bio Gel P-30 media for ATTO647N labeling (d = 1 cm, l = 30 cm) and on a Sephadex column (GE healthcare PD mini Trap G.25, *GE Healthcare Bio-Sciences AB*, Uppala, Spain) in the case of biotin labeling. After pre-equilibration, the corresponding protein conjugate was eluted and collected in fractions (the first colored zone in the case of dye labeling). The purified labeled vimentin monomer fractions were analyzed by UV/vis spectroscopy at $\lambda_{\text{protein}} = 280$ nm and $\lambda_{\text{dye}} = 650$ nm, or $\lambda_{\text{biotin}} = 350$ nm on a Nanodrop (Nanodrop2000c, *Thermo Fisher Scientific*, Dreieich, Germany). Fractions with a concentration > 0.10 mg/ml were pooled and were combined in a dialysis tube (50 kDa MWCO) in the storage buffer overnight at 4°C. After dialysis, the concentration of the sample was determined, and the labeled protein was aliquoted and stored at -80°C until use.

3.2.3.2 Dialysis of Vimentin into Low Salt Buffer

Since vimentin monomers were dissolved in 8 M urea, they were brought into low urea buffer by stepwise dialysis to form higher-ordered structures as the tetramer for vimentin. In order to work under physiological conditions, the salt concentration was also lowered by the stepwise dialysis. The required buffers are listed in Tab. 3.4.

Tab. 3.4: Composition of dialysis buffer and dilution buffer used in this work. The dilution buffer is used to dilute the urea concentration in the dialysis buffer.

	Dialysis Buffer	**Dilution Buffer**
NaH_2PO_4 (PB A)	20 mM	2 mM
NaH_2PO_4 (PB B)	20 mM	2 mM
Urea	6 M	-
pH	7.5	

The unlabeled vimentin monomers, ATTO647N labeled, and biotinylated monomers were thawed at 37°C to avoid false folding. After defrosting, they were mixed in a dialysis tube (50 kDa MWCO) to ensure that the final concentration of the mixture contained 10 % ATTO647N labeled monomers and 5 % biotinylated monomers. The dialysis tube was dialyzed against the dialysis buffer (cf. Tab. 3.4) for 30 min at room temperature. By stepwise dialysis, the urea concentration was decreased to 4 M, 2 M, 1 M, 0 M using the dilution buffer (cf. Tab. 3.4), and incubating for 30 min after each dilution step. The last dialysis step into dilution buffer was carried out overnight at 4°C. Subsequently, the concentration of the formed vimentin tetramers was adjusted to about 0.4 mg/mL by UV/vis spectroscopy at $\lambda_{\text{protein}} = 280$ nm on a Nanodrop (Nanodrop2000c, *Thermo Fisher Scientific*, Dreieich, Germany) using the dilution buffer, and stored protected from light at 4°C until use.

3.2.3.3 Assembly of Vimentin Tetramers

The assembly of vimentin tetramers into matured filaments was initiated by the use of monovalent ions and did not require the addition of adenosine triphosphate (ATP).

There are two ways to assemble tetramers into filaments, one is by dialysis, and the other is by kick-start assembly. In this study, kick-start assembly was performed.

Vimentin tetramers obtained by dialysis, the concentration of which was adjusted to 0.4 mg/ml, were diluted 1:1 with assembly buffer containing KCl (cf. Tab. 3.5) and assembled at 37°C for 90 min.

Tab. 3.5: Composition of assembly buffer used in this work. It contains KCl, which initiates the hierarchical assembly process into mature vimentin filaments.

Composition	Concentration
NaH_2PO_4 (PB A)	2 mM
Na_2HPO_4 (PB B)	2 mM
KCl	200 mM
	pH 7.5

3.3 Biosensing Methods

3.3.1 UV/vis Spectroscopy

Optical spectroscopy, such as UV/vis spectroscopy, is based on the absorption of light by matter in the ultraviolet (UV) and visible (vis) light regions.[121] The sample is excited, and electrons from the highest occupied molecular orbital (HOMO) are transferred to the lowest unoccupied molecular orbital (LUMO). The smaller the HOMO-LUMO energy gap, the longer the absorbed wavelength.[122]

Proteins show an absorption maximum at λ_{protein} = 280 nm caused by $\pi - \pi^*$ transitions of amino acids containing conjugated π-bonds, such as tryptophan (Trp), tyrosine (Tyr), and cysteine disulfide (Cys SS) bonds. For this reason, the determination of protein concentration can be easily accomplished by absorbance measurements at λ_{protein} = 280 nm. According to LAMBERT-BEER's law, the absorbance (A_{280}) is determined by the following equation (cf. Eq. 3.1).[123]

$$A_{280} = -\log\frac{I}{I_0} = \epsilon_{280} \cdot c_{\text{protein}} \cdot d \tag{3.1}$$

The absorbance is proportional to the quotient of the intensity of light before (I_0) and after (I) passing through the protein solution with a concentration (c_{protein}) and a certain optical path length (d). The extinction coefficient (ϵ) is specific for each protein and can be calculated by linear combination of the numbers of individual amino acid residues (n_{x}cf. Eq. 3.2)[122,123]

$$\epsilon = 5500 \cdot n_{\text{Trp}} + 1490 \cdot n_{\text{Tyr}} + 125 \cdot n_{\text{CysSS}} \tag{3.2}$$

The extinction coefficients of Trp, Tyr and CysSS are 5500, 1490 and 125 $\text{L}\cdot\text{mol}^{-1}\cdot\text{cm}^{-1}$, respectively. The accuracy is found as ± 5 %.[123]

Since the proteins are fluorescently labeled, the concentration of labeled proteins is determined using absorbance measurements by considering the absorption ($\text{A}_{\text{max,dye}}$)

of the respective fluorophore (cf. Eq. 3.3).

$$c_{\text{protein}} = \frac{A_{280} - A_{\text{max, dye}} \cdot f}{\epsilon_{280}} \tag{3.3}$$

The factor f takes into account that the absorption of the fluorophore at the absorption maximum of the protein is equal to the ratio of absorption of the dye at this wavelength to its absorption at the maximum of the dye at long wavelengths.[124] In the case of the fluorophore used in this work (ATTO647N), the correction factor is given by the manufacturer as $f = 0.03$.[125] The key parameter is the knowledge of the degree of label (DOL), which is important for accuracy, reproducibility, and comparison of labeling performance.[124] It is essentially the average number of fluorophores bound to the protein and is calculated using Eq. 3.4.

$$DOL = \frac{c_{\text{dye}}}{c_{\text{protein}}} = \frac{A_{\text{max,dye}} \cdot \epsilon_{280}}{(A_{280} - A_{\text{max,dye}} \cdot f) \cdot \epsilon_{dye}} \cdot 100 \tag{3.4}$$

The extinction coefficient of the dye (ϵ_{dye}), ATTO647N, is given by the manufacturer as $\epsilon_{\text{dye}} = 1.5 \cdot 10^5$ L·mol^{-1}·cm^{-1}.[125] For biotin labeling, there was no suitable kit to determine the label density since it is difficult to detect biotin due to the overlap of its intrinsic absorbance with that of proteins. Assays have been developed to shift the absorption wavelength (*e.g.* HABA assay, HUANG assay), but these assays need rapid readout, high throughput, wash-free, and sensitivity.[126] Therefore, it could only be assumed that the DOL was 100 %.

In this work, to determine the protein concentration of unlabeled, fluorescently labeled, as well as biotin-labeled vimentin monomers, UV/vis measurements were performed using a Nanodrop (Nanodrop2000c, *Thermo Fisher Scientific*, Dreieich, Germany), which is capable of measuring small volumes. The molecular weight of vimentin with 56.67 kDa and an extinction coefficient of 24240 L·mol^{-1}·cm^{-1} were used for these measurements.

3.4 Biophysical Methods

3.4.1 Confocal Laser Scanning Microscopy

Fluorescence microscopy is one of the most widely used light microscopy techniques. It is a non-invasive technique and has high selectivity. Fluorescence imaging has become an important mainstay of microscopy in biological research involving dyes that emit light within nanoseconds of absorbing light of a dye-specific wavelength. This phenomenon is called fluorescence. Usually, the emitted wavelength is longer than the absorbed wavelength. This so-called STOKES shift of emittance and absorbance makes the fluorescence microscope a powerful tool by allowing a separation.[127]

An even more powerful innovative tool for viewing microscopic structures in 3D with improved contrast, resolution, diffraction, and signal-to-noise ratio (SNR) is Confocal Laser Scanning Microscopy (CLSM). The basic concept of scanning the illumination and scanning the detection was first described and patented by MINSKY.[128] The method (cf. Fig. 3.11 A) is based on illumination with a diffraction-limited spot created by converting the collected plane wave into a converging spherical wave in the objective through the lens, which focuses the light at the "waist" of an hourglass-shaped laser beam that contains all its energy in a collected coherent plane wave. The image is divided into pixels, and each pixel is scanned by two oscillating mirrors that direct the laser beam towards and away from the object. One mirror illuminates and captures the fast axis while the other scans the slow axis until the entire image of the *xy*-plane (2D image) is recorded. The focal plane can be maintained to obtain time series, and for 3D imaging, the focus can be shifted along the *z*-axis. A dichroic mirror and an emission filter separate the emission wavelength from the excitation wavelength by reflecting the latter.[129] Since the light cone does not completely illuminate the object of interest due to diffraction, it results in a much larger point source surrounded by diffraction rings with decreasing intensity from the center to the outer rings (cf. Fig. 3.11 B). This pattern is called a point spread function (PSF).[129,130] The PSF depends on the emitted wavelength and the numerical aperture (*NA*) of the objective. Small PSFs are produced by shorter wavelengths and higher *NA* lenses.[130] Only scanning of the illumination is not sufficient to remove out-of focus light generated by scattering. Thus, a pinhole is placed in front of the detector to ensure the illumination point and the pinhole are focused on the same point simultaneously.[129] Small pinholes (*e.g.* $\leq$ 1 Airy Unit (AU)) result in a PSF with a compact shape leading to improved resolution and contrast, however at the same time, the number of photons passing through can be reduced leading to reduced detection efficiency. Large pinholes (*e.g.* > 1 AU) increase the size of the PSFs and reveal diffraction rings in the out-of focus planes.[130] The appropriate size of the pinhole, based on experimental and theoretical approaches, is approximately the size of the projected diffraction-limited spot ($1.22 \cdot \lambda / NA$). To counter the slow acquisition time in sequential imaging, a photomultiplier (PMT) serves as a fast-response detector that detects weak signals. However, the efficiency of photons detected by the pinhole is 10% or less. As the scanning speed increases, the quality of the image decreases as the number of photons detected decreases.[129]

An important feature that makes CLSM more powerful than wide-field microscopy is resolution, which is defined as the ability to distinguish two closely spaced spots as two clearly defined individual points. Thus, two spots must be at least as close as the distance between the center of the PSF and the first destructive interference band (cf. Fig. 3.11 C).The RAYLEIGH criterion can be used to calculate the resolution, which is given in Eq. 3.5 and 3.6.[130]

$$R_{lateral} = \frac{0.51 \cdot \lambda_{\text{exc}}}{NA} \tag{3.5}$$

$$R_{axial} = \frac{0.88 \cdot \lambda_{\text{exc}}}{n - \sqrt{n^2 - NA^2}} \tag{3.6}$$

The resolution is proportional to the excitation wavelength λ_{exc}. n is the refractive index of the medium, and NA is the numerical aperture of the lens in the objective. In practice, resolving power can be determined from the full width at half maximum (FWHM) of a 3D PSF of low-resolution fluorescent microspheres.[130] Compared to wide-field microscopes, CLSM achieves 1.4 times better resolution because the PSF is narrower (cf. Fig. 3.11 D).[129]

In recent decades, numerous microscopes such as Airyscan Microscopy, Total Internal Reflection Fluorescence (TIRF), or Stimulated Emission Depletion (STED) have been developed to improve resolution further and allow imaging of structures below ABBE limit ($\frac{\lambda}{2 \cdot NA}$).

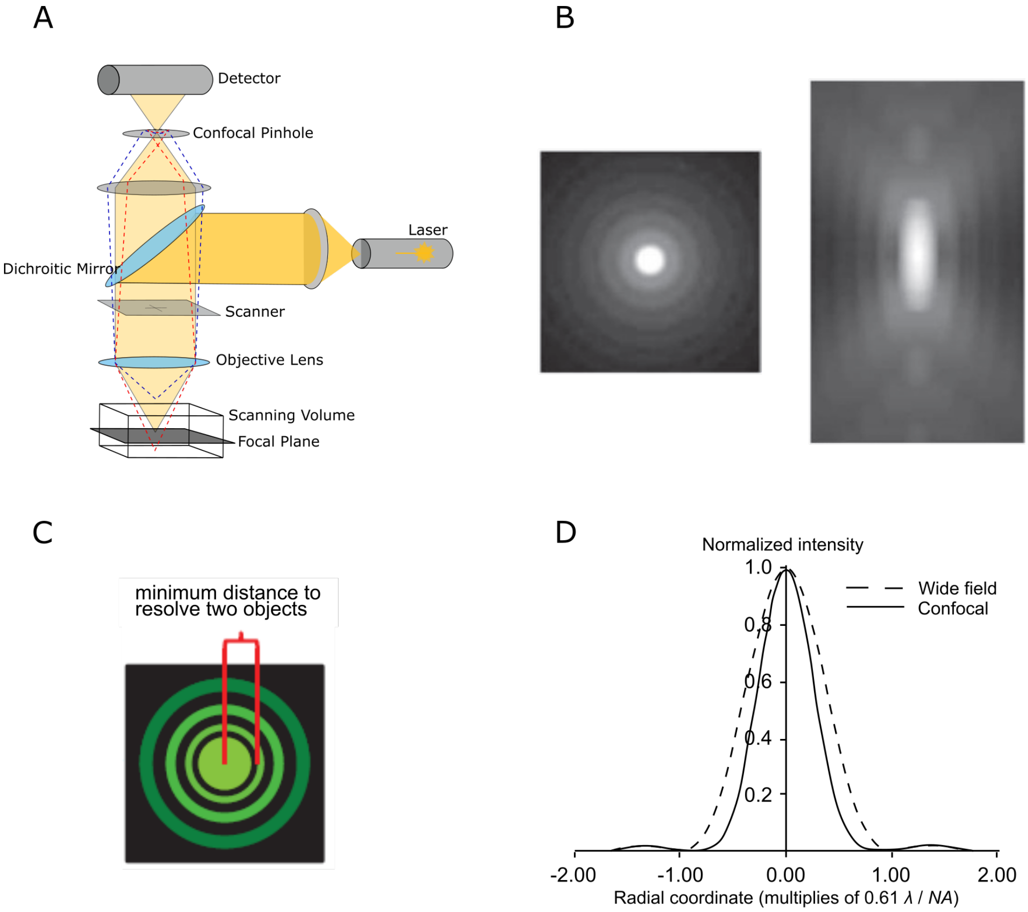
A
Detector
Confocal Pinhole
Laser
Dichroitic Mirror
Scanner
Objective Lens
Scanning Volume
Focal Plane
B
C
minimum distance to resolve two objects
D
Normalized intensity
1.0
0.8
0.6
0.4
0.2
Wide field
Confocal
-2.00
-1.00
0.00
1.00
2.00
Radial coordinate (multiples of 0.61 λ / NA)

Fig. 3.11: (**A**) Principle of confocal laser scanning microscopy (CLSM). Light from the laser is reflected through the objective on the dichroic mirror onto the sample in the focal plane. This emits fluorescence that passes through the dichroic mirror, followed by a moving mirror system, and through a pinhole before reaching the detector.[129] (**B**) The point spread function (PSF). The light distribution near the confocal spot with rings of progressively lower light intensity. The diffraction rings and dark areas are caused by constructive and destructive interference of diffracted light, respectively. PSF in the *xy* plane (*left*); PSF in the *yz* plane (*right*).[130] (**C**) Schematic drawing of the diffraction pattern. The resolving power by Rayleigh criterion is defined as the distance from the center of the PSF to the first destructive interference band that resolves it.[130] (**D**) Plot of an intensity profile of the PSF of conventional and CLSM. The PSF of the CLSM is narrower than that of the conventional microscope, resulting in 1.4 times better resolution.[129]

3.4.1.1 Airyscan Microscopy

Airyscan microscopy is a technology introduced in 2014 which offers advantages compared to classical CLSMs by increasing spatial resolution and signal-to-noise ratio while maintaining the optical sectioning capability of a CLSM.[131] This was achieved by combining confocal imaging with a 0.2 AU pinhole setting, deconvolution based on the Wiener filter, and the principle of pixel reassignment.[132] The pinhole-detector design of a traditional CLSM was optimized and replaced with an Airyscan detector containing a hexagonally packed detector array, typically a gallium arsenide phosphide photomultiplier (GaAsP-PMT), which consists of 32 detector elements, each serving as an individual pinhole of 0.2 AU size. Thus, the total detector area is equivalent to 1.25 AU (cf. Fig. 3.12).

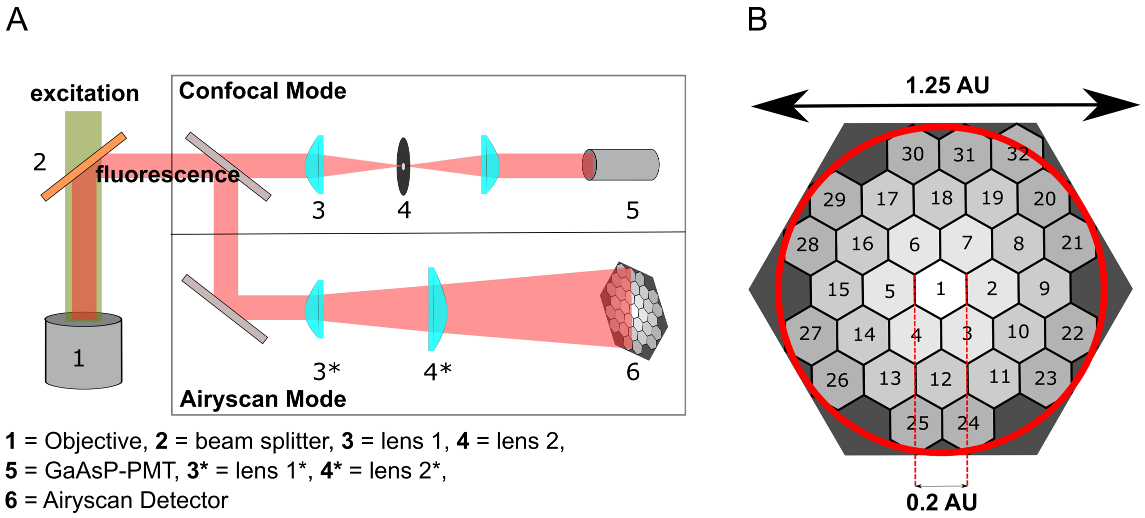
A
B
excitation
Confocal Mode
2
fluorescence
3
4
5
1
3*
4*
6
Airyscan Mode
1 = Objective, **2** = beam splitter, **3** = lens 1, **4** = lens 2,
5 = GaAsP-PMT, **3*** = lens 1*, **4*** = lens 2*,
6 = Airyscan Detector
1.25 AU
30 31 32
29 17 18 19 20
28 16 6 7 8 21
15 5 1 2 9
27 14 4 3 10 22
26 13 12 11 23
25 24
0.2 AU

Fig. 3.12: Principle of Airyscan Microscopy. (**A**) The schematic representation of the beam path of the Airyscan microscope compared to CLSM. In airyscan mode, the pinhole-detector design is replaced by an airyscan detector. (**B**) The airyscan detector consists of 32 individual detector elements, each of which has a pinhole aperture of 0.2 AU, resulting in a total detector size of 1.25 AU.[131,133] Adapted from FRITZSCHE *et al.*[132]

Scanning the central pixel results in a spatial resolution of the reconstructed image that is similar to images obtained with a conventional CLSM with a 0.2 AU pinhole setting, but the overall sensitivity of the system is comparable to confocal images obtained with a 1.25 AU pinhole setting.[131,132] A 1.7-fold increase in spatial resolution (lateral: 140 nm, axial: 400 nm) and a 4-8-fold increase in SNR compared to conventional CLSMs is achieved by SHEPPARD's pixel reassignment followed by a linear deconvolution step based on a WIENER filter during image reconstruction.[131,133,134]

Experimental procedure

In this work, membrane-bound VIFs and VIF networks labeled with 10 % ATTO647N and 5 % biotin maleimide were studied. The composite system was imaged in the prepared PDMS chamber, in which blue beads were embedded with various motor positions.

For this purpose, the PDMS chamber was hydrophilized with 100 % oxygen plasma according to chapter 3.2.1. The preparation of SUVs is described in chapter 3.2.2. The obtained ATTO488 labeled vesicles containing biotinylated lipids (500 µL) were placed on the hydrophilized PDMS surface and incubated for 15 min. To get rid of excess vesicles, the solution was rinsed 20 times. A neutravidin solution in vimentin buffer (cf. Tab. 3.2) was prepared at a concentration of 1 mg/mL, and 200 µL was added to the prepared lipid bilayer to bind the biotin headgroup of DOPE. After 90 min incubation, a 30-fold wash step was performed. VIFs (400 µL for filament studies and 800 µL for network studies) constructed according to chapter 3.2.3.3 were added after dilution (1:10 or 1:20 for filament studies and 1:1.25 for network studies) and rinsed 10 times after 90 min incubation. The final step was the addition of SUVs that did not contain biotinylated DOPE and incubation for 1.0 h.

To image the composite system, a LSM 880 (*Carl Zeiss Microscopy GmbH*, Oberkochen, Germany) with an airyscan detector equipped with a 40x water immersion objective (W Plan-Apochromat, $NA = 1.0$, *Carl Zeiss Microscopy GmbH*, Oberkochen, Germany). The settings used are given in Tab. 3.6. CLSM images of the beads, vimentin filaments and networks were acquired for each motor position. Airyscan mode was used for the vimentin filaments and networks. In the case of the membrane, CLSM images were acquired before adding the lipid reservoir. When a motor position of 10 mm was reached, the excess lipid reservoir was removed by rinsing 25-30 times, and an image was acquired after removal.

Tab. 3.6: User settings for the microscopy to study the membrane-bound vimentin filaments and networks under strain.

	Beads	**Membrane**	**Vimentin**
Fluorophore	405	488	647N
Laser	Diode 405-30	Argon	HeNe633
Laser Power	2%	2%	2%
Resolution	1024 x 1024	256 x 256	256 x 256
Scan time	3.3 s	10.1 s	10.1 s
Bit Depth	16 bit	16 bit	16 bit

3.4.1.2 Fluorescence Recovery After Photobleaching

One factor that affects the quality of the fluorescence image is bleaching. Bleaching is a process in which the triplet state of the fluorophore interacts with molecular oxygen by transferring its energy to the ground state of oxygen. The reactive singlet oxygen can participate in chemical reactions with organic molecules, such as the fluorophore, resulting in the destruction of the fluorescence ability.[127] However, fluorescence recovery after photobleaching (FRAP) takes advantage of this bleaching phenomenon.

FRAP is a powerful and widely used method based on fluorescence microscopy to obtain information about the dynamics of fluorescently labeled molecules (*e.g.*, lipids or proteins) at the submicrometer scale.[135] It is specifically used to determine a coefficient of diffusion processes by providing quantitative approaches.[6] Non-directional diffusion is defined as a mass transport of specific molecules that occurs in the absence of external forces.[135]

The general principle is that fluorescent molecules are irreversibly bleached using a short pulse of high-intensity light, leading to a decrease in fluorescence intensity in the region of interest (ROI). Depending on the lateral mobility of the fluorescently labeled molecules, the fluorescence intensity is regenerated as fluorescently labeled molecules diffuse into the ROI and bleached molecules out. Over time, the bleached ROI recovers because the fluorescence intensity increases (cf. Fig. 3.13). This process occurs at a specific rate, which depends on the mobility of the molecules.[6,135]

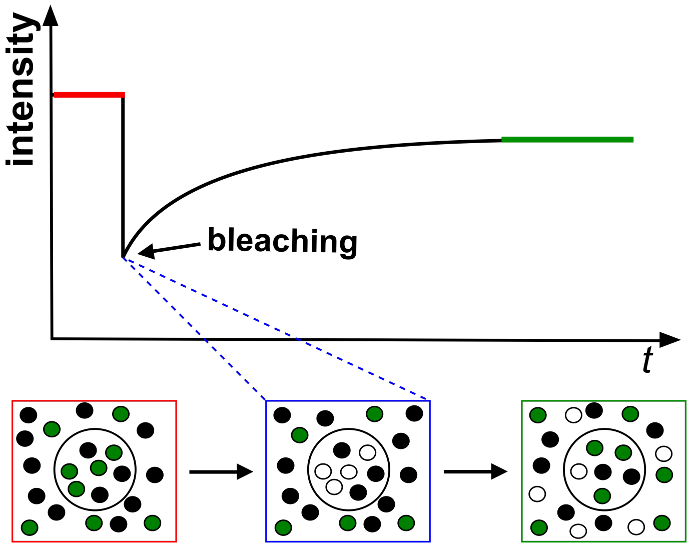

Fig. 3.13: Principle of fluorescence recovery after photobleaching (FRAP) to measure lateral diffusion of fluorescently labeled molecules. Black circles are unlabeled molecules, while green circles represent fluorescently labeled molecules. White circles are assigned to bleached molecules. Fluorescence intensity is homogeneously distributed at the beginning of a FRAP experiment (red frame). Irradiation of the region of interest (ROI) with an intense laser pulse destroys fluorescently labeled molecules without damaging the molecule itself (blue frame). Lateral diffusion leads to the regeneration of fluorescence intensity (green frame). The red and green lines in the FRAP curve show the fluorescence intensity before and after bleaching, respectively.[6,135]

To evaluate FRAP experiments, the concept of AXELROD *et al.* is used, in which two-dimensional diffusion of fluorophores is homogeneously distributed in the membrane. This concept was further optimized by SOUMPASIS *et al.* and KANG *et al.*. It is assumed that bleaching is an irreversible first-order process that depends on the efficiency and intensity profile of the laser and the extinction coefficient of the fluorophores. The distribution of fluorescence intensity in the ROI is described by a GAUSSIAN profile. The raw fluorescence intensity ($F_{\mathrm{raw}}(\mathrm{k})$) obtained from FRAP experiments has to be corrected by background fluorescence intensity (F_{bk}(t)) and photofading (F_{fade}(k)) (cf. Eq. 3.7) followed by a normalization to the prebleach intensity.[136]

$$F_{corr}(t) = \frac{F_{\text{raw}}(k) - F_{bk}}{F_{\text{fade}}(k) - F_{bk}} \tag{3.7}$$

The first approach to determine the diffusion coefficient by AXELROD *et al.* based on the second law of FICK is given in Eq. 3.8.[137]

$$D_{\text{n}} = \frac{r_{\text{n}}^2}{4 \cdot \tau_{1/2}} \tag{3.8}$$

The nominal bleaching radius is the radius of the set bleaching laser. In this approach, diffusion during photobleaching is neglected. However, since diffusion does occur when performing FRAP experiments in a confocal setup, using the nominal radius of the bleach spot is not accurate, resulting in an underestimation of the diffusion coefficient. Therefore, a more accurate method is to use the effective radius (r_{eff}). KANG *et al.* defined the effective radius as the radius of the postbleach profile at the height of 0.86 with its depth of K. Thus, the transformed equation for the diffusion coefficient is shown in Eq. 3.9.[136]

$$D_{\text{eff}} = \frac{r_{\text{n}}^2 + r_{\text{eff}}^2}{8 \cdot \tau_{1/2}} \tag{3.9}$$

However, for $r_{\text{eff}} \approx r_{\text{n}}$, D_{eff} is approximately equivalent to D_{n}, which equals the equation of AXELROD and SOUMPASIS.

Considering the above-mentioned equations (cf. Eqs. 3.8 and 3.9), the diffusion coefficients also depend on the half-life of recovery ($\tau_{1/2}$), which is basically the time it takes a bleach spot to recover halfway between the original and saturated fluorescence intensity.[136] It can be easily extracted from the recovery curve of $F_{\text{corr}}(t)$ by fitting it according to SOUMPASIS (cf. Eq. 3.10).[138]

$$F_{\mathrm{corr}}(t) = A \cdot e^{\frac{-2\tau_{1/2}}{t}} \cdot \left[I_0 \cdot \frac{-2\tau_{1/2}}{t} + I_1 \cdot \frac{-2\tau_{1/2}}{t} \right] \tag{3.10}$$

I_0 and I_1 describe the modified BESSEL functions of 0^{th} and 1^{st} order, respectively. With the extracted half-life, the diffusion coefficient can be calculated according to Eq. 3.9. Furthermore, the mobile ratio (R_{m}) can be extracted from the recovery curve. The corresponding equation is given below (cf. Eq. 3.11) with F_∞ being the postbleach steady-state fluorescence intensity, F_0 the initial postbleach fluorescence intensity and F_{i} the prebleach fluorescence intensity.[137,138]

$$R_{\mathrm{m}} = \frac{F_\infty - F_0}{F_{\mathrm{i}} - F_0} \tag{3.11}$$

Experimental Procedure

The ATTO647-labeled lipid bilayer containing an ATTO488-labeled lipid reservoir in solution was studied under strain, aiming to stretch artificial lipid membranes more than the 4-6 % found in the literature. To this end, a membrane was applied to a hydrophilic PDMS surface by adding SUVs and incubating for 15 min. After rinsing 20 times, SUVs were added as lipid reservoirs and incubated for 1 h. CLSM images were acquired with the same settings as in Tab. 3.6, and FRAP experiments were performed after each motor position to gain insights into the mobility of the membrane under strain. When a motor position of 10 mm was reached, excess vesicles in the solution were removed by rinsing 25-30 times. CLSM imaging and FRAP experiments were performed. Tab. 3.7 lists the setting parameters for FRAP experiments. FRAP experiments were also performed with VIFs attached to the membrane before and after stretching (cf. Tab. 3.6).

Tab. 3.7: User settings for the microscopy to study the mobility of the membrane under strain.

	Settings
Fluorophore	488
Laser	Argon
Laser Power	2%
Resolution	256 x 256
Scan time per frame	≈ 54 ms
$\boldsymbol{d_n}$	29-31 px
Bleach pulse power	100%
***N* (frames)**	250
Bit Depth	16 bit

3.4.2 Atomic Force Microscopy

Atomic force microscopy (AFM), first invented in 1986 by BINNING, QUATE and GERBER [139], was awarded the Nobel prize and represents a major breakthrough in the history of nanotechnology that opened new possibilities in physics, chemistry, biology and medicine. [140] It has become an instrument that can measure microstructural parameters and decipher intermolecular forces at the nanoscale with atomic resolution. [141] BINNING *et al.* revealed a lateral and vertical resolution of 30 Å and less than 1 Å, respectively. [139]

A typical AFM setup is shown in Fig. 3.14, whose core component is a tip attached to a cantilever spring. The cantilever is mounted to a piezoelectric element. By passing the tip of the cantilever line-by-line over the sample, the interaction force between the tip and the sample is detected by monitoring the deflection of the cantilever. The deflection is measured by reflecting the laser beam from the back of the cantilever *via* a mirror onto a position-sensitive photodetector with four quadrants. The feedback mechanism from the differences in light intensities between the upper (I(A)) and lower quadrant (I(B)) of the photodiode allows the piezo scanners to control the height and keep the tip at a constant deflection. [141,142]

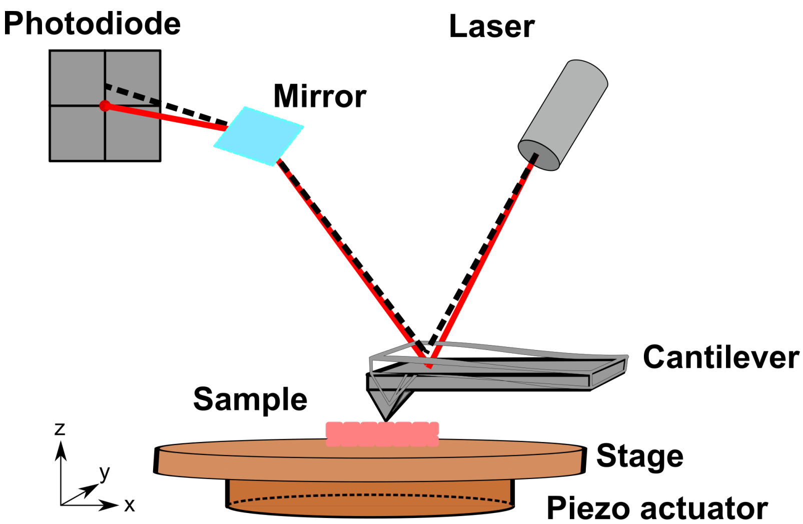

Fig. 3.14: Principle of the atomic force microscopy (AFM). While the sample is scanned with the tip of the cantilever, the deflection of the cantilever is detected by a photodiode with four quadrants. This is achieved by a laser beam reflecting off the back of the cantilever *via* a mirror. A feedback mechanism allows the piezo actuator to maintain a constant force or height.[141,142] Inspired by MEY[143]

Thus, the vertical deflection can be calculated as a function of the intensity changes between the upper and lower photodiode relative to the total measured intensity (cf. Eq. 3.12). The lateral deflection can be determined in an analogous way.

$$A_{\mathrm{vertical}} = \frac{I(\mathrm{A}) - I(\mathrm{B})}{I(\mathrm{A}) + I(\mathrm{B})} \tag{3.12}$$

3.4.2.1 Force Distance Curves

Force distance (FD) curves can be used to determine the mechanical properties of the specimen. Here, the deflection, which includes the vertical position of the tip of the cantilever, is recorded and converted into an FD curve, the goal being to reduce the overall force of the tip-sample interaction. The force F is obtained by taking the amount of deflection of the cantilever (Z_{C}) and multiplying it by its spring constant (k_{C}), which is known as the HOOK's law (cf. Eq. 3.13. The spring constant depends on the length L_{C}, the width w_{C}, and the thickness t_{C} of the particular V-shaped cantilever. The YOUNG's modulus E must also be considered.[142]

$$F = k_{\mathrm{C}} \cdot Z_{\mathrm{C}} = \frac{E \cdot w_{\mathrm{C}} \cdot t_{\mathrm{C}}^3}{2 \cdot L_{\mathrm{C}}^3} \cdot Z_{\mathrm{C}} \tag{3.13}$$

However, theoretical determinations of the cantilever spring constant are often a rough approximation and simplification since they do consider other geometries than rectangles, materials used, or structural defects. Therefore, HUTTER *et al.* have proposed an effective experimental method to determine the spring constant, namely the recording of a thermal noise spectrum assuming that a cantilever behaves like a harmonic oscillator with one degree of freedom.[144] The mechanical properties of a cantilever change with respect to the surrounding medium, so it is necessary to consider the medium density (ρ_f), which is the more accurate method of SADER *et al.*, leading to the following equation (cf. Eq. 3.14).[145]

$$k_C = 0.1906 \cdot \rho_\mathrm{f} \cdot w_\mathrm{C}^2 \cdot L_C \cdot Q \cdot \Gamma_\mathrm{i}(\nu_\mathrm{k}) \cdot w_0^2 \tag{3.14}$$

The density of the medium, the quality factor Q, the imaginary component of the hydrodynamic function $\Gamma_\mathrm{i}(\nu_\mathrm{k})$ and the resonance frequence of the cantilever w_0 are viewed in Eq. 3.14.

The tip-sample distance D adds the cantilever deflection and the position of the piezo (Z_P) (cf. Eq. 3.15).

$$D_\mathrm{TS} = Z_\mathrm{P} + Z_\mathrm{C} \tag{3.15}$$

A FD curve is recorded by moving the cantilever in z direction and maintaining the xy positions (cf. Fig. 3.14). The signal of the photodiode is captured as a function of the z-piezo movement. Such a FD curve is shown in Fig. 3.15. As the cantilever tip approaches the surface (blue), it initially experiences no interaction force. The photodiode provides a constant signal because no deflection of the cantilever is detected by a laser beam (I). Near the surface, the increasing attractive interaction forces lead to an effect called "snap-on" (II), and the tip jumps into contact with the sample (III). When the cantilever contacts the sample, the signal from the photodiode increases linearly with the expansion of the piezo until the trigger point is reached (III). When the piezo is retracted (red), the retraction path (IV) shows the same behavior as the approach path (III). Adhesive forces cause the scanning probe to stick to the surface, resulting in a so-called "snap-off" that can be unspecific (V) or specific bindings (VI). Subsequently, the photodiode again displays a constant signal. By determining the slope of the FD curve recorded on hard surfaces, the sensitivity is determined, which relates the deflection of the cantilever to the measured voltage differences at the photodiode.[143]

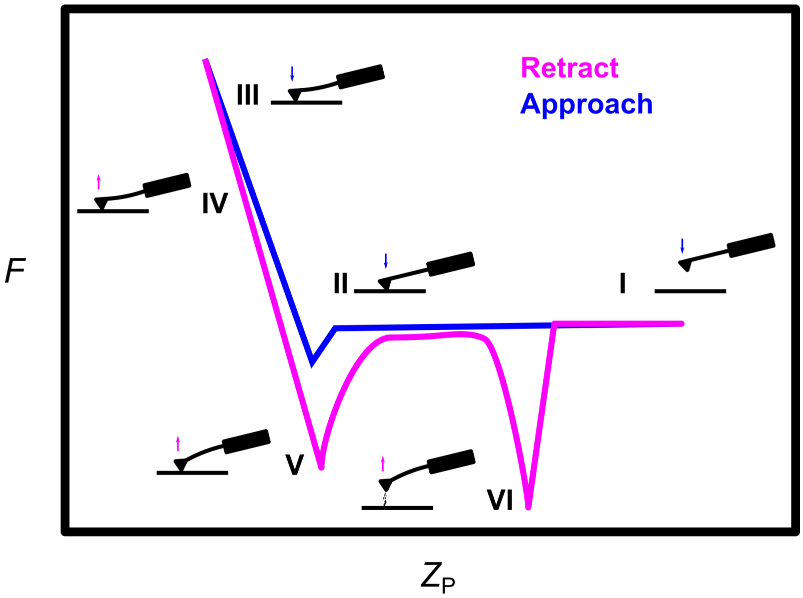

Fig. 3.15: Schematic representation of a typical force-distance (FD) curve. When the cantilever tip approaches the surface (blue), no interaction force acts on the cantilever, and the photodiode provides a constant signal (I). Near the surface, the increasing attractive interaction forces lead to a "snap-on" effect (II), and the tip jumps into contact with the sample (III). When the cantilever has contact with the sample, the signal from the photodiode increases linearly with the expansion of the piezo (III). When the piezo is retracted (red), the retraction path (IV) shows similar behavior as the approach path (III). Adhesive forces can be present that cause the scanning probe to stick to the surface, resulting in a so-called "snap-off". It can be due to unspecific (V) or specific bindings (VI). Subsequently, the photodiode again displays a constant signal.[143] Inspired by MUELLER *et al.*[140]

3.4.2.2 Quantitative Imaging Mode

AFM is a powerful imaging instrument that can visualize samples (*e.g.*, biological samples) with atomic resolution. The most common imaging modes are contact and dynamic modes. The contact mode is one of the first invented imaging modes, which relies on repulsive interaction forces between the tip and the sample.[140,141] Because the tip is in close contact, unwanted lateral forces can act on the sample, causing irreversible damage to the sample. Although the dynamic mode was designed to reduce friction and lateral forces, it must deal with compression of soft samples and obstacles on sticky samples because it has no control over vertical forces.[140,146]

New development to eliminate lateral forces and control vertical forces is the Quantitative Imaging (QI) mode. It is a force curve-based imaging mode that measures FD curves at each pixel of the image, providing not only topographic information but also mechanical properties of the sample like elasticity and adhesion with high spatial resolution. The interaction force can be minimized by below 50 pN while imaging. Unlike regular force mapping, QI mode uses a novel tip movement algorithm that speeds up scanning (cf. Fig. 3.16). The cantilever is driven with a constant velocity onto the specimen from a fixed defined height, the z length, while there is no movement in xy direction. The height of the z piezo element is reduced until a certain deflection or force of the cantilever is reached. The cantilever is then returned to the initial height. A height image of the specimen can be calculated from the z piezo heights reached at each trigger point. Furthermore, elasticity and adhesion images can also be created. Elasticity images are obtained by fitting the slope of the FD curve with a linear fit, which is an approximation. Depending on the sample, there are more accurate fitting models, such as the HERTZ model.[147] For an adhesion pattern, the maximum adhesion force is calculated by finding the highest adhesion values from the retraction part of an FD curve.[146]

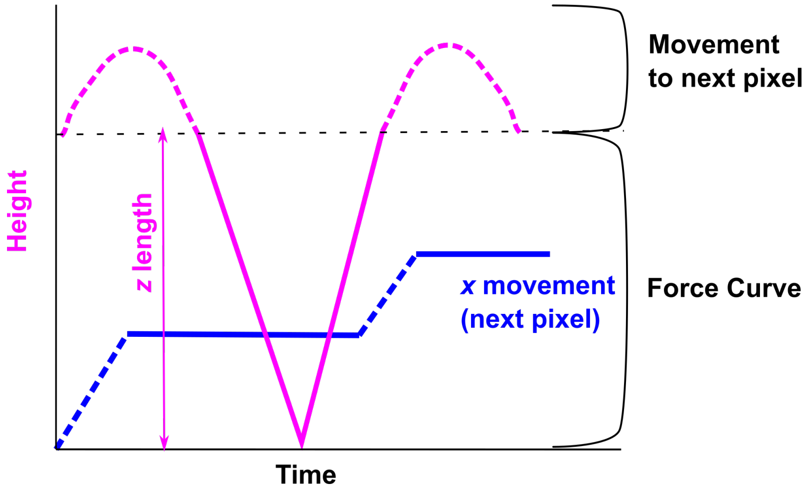

Fig. 3.16: Schematic illustration of the quantitative imaging (QI) mode. The approach of the cantilever to the specimen is from a fixed z length following a xy movement, *i.e.*, there is no movement in the xy direction during the approach, which significantly reduces lateral forces. Since the set point can be adjusted, there is control over the vertical force.[146]

Experimental Procedure

Membrane-bound VIF networks were imaged in QI mode was performed to gain insights into their structural properties. They were studied under unstretched conditions. Sample preparation is described in chapter 3.4.1.1 under Experimental Procedure. No lipid reservoir was used in this case because the system was not stretched laterally.

For this purpose, a JPK Nanowizard 3 and 4 (*JPK Instruments*, Berlin, Germany) was used to perform the measurements. After positioning the laser beam on the back side of the cantilever, a calibration of the cantilever was performed as described by SADER *et al.*[145] by determining a thermal noise considering the medium. This allowed for the accurate determination of the spring constant of the used cantilever. The cantilever and its characteristics are shown in Fig. 3.17. The sensitivity was determined by plotting an FD curve with a relative set point of 1.0 V and a velocity of 1.0 µm/s. Adjusting the slope yielded the sensitivity. In QI mode, an image size of 2 µm x 2 µm was recorded with a set point of 0.3 nN, a *z* length of 300 nm, and a pixel dwell time of 100 ms.

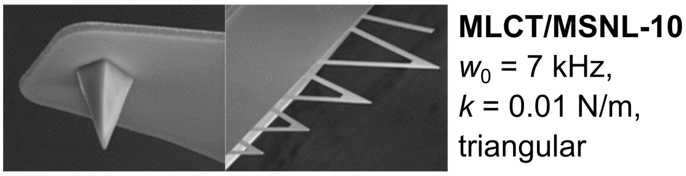

Fig. 3.17: Electromicrographs of the cantilever used in this work with their specifications. The triangular cantilever MSNL-10 is used for imaging.[148]

3.5 Data Evaluation and Processing

3.5.1 Beads Evaluation

The beads (4 µm) embedded in the PDMS sheet (cf. chapter 3.1.5) were analyzed by tracking them in each stretching step. Therefore, fluorescence micrographs were taken at each motor position (mp, Δmp = 1 mm, mp_{max} = 10 mm) and subsequently aligned relative to one bead, preferably in the center, the reference bead. The beads were detected with the cell segmentation algorithm cellpose, and the center of mass of each bead was marked. (cf. Fig. 3.18) [149]

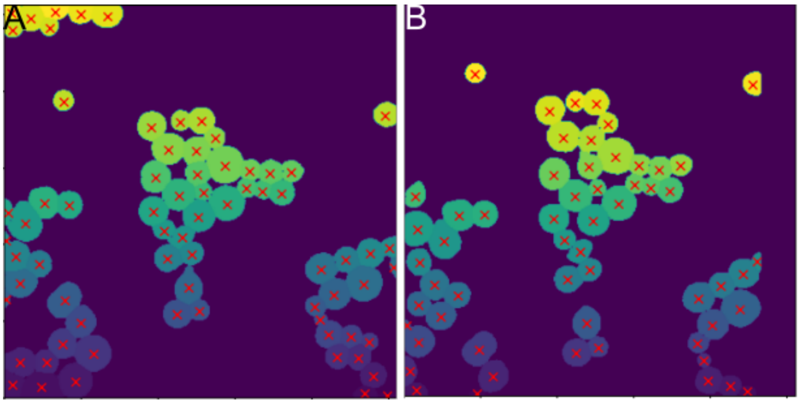

Fig. 3.18: Detection of beads (4 µm), which are embedded in the polydimethylsiloxane by using cellpose. [149] The centers of mass of the individual beads are marked with 'x' for accurate length determination. (A) Beads in the unstretched state (mp = 0 mm), and (B) beads in the stretched state (mp = 10 mm).

A displacement field of each bead was generated by tracking the individual beads in the recorded fluorescence micrograph at each stretching step. With this in hand, the distances ($L_{\text{Beads,i}}$) between the reference bead and surrounding beads at different mp were determined, and by using Eq. 3.16, the resulting strains of beads were calculated.

$$\epsilon_{\text{Beads}} = \frac{L_{\text{Beads, mp}} - L_{\text{Beads,0}}}{L_{\text{Beads,0}}} \tag{3.16}$$

Analogously, the longitudinal ($\epsilon_{\text{Beads},yy,\text{mp}}$) and lateral strains ($\epsilon_{\text{Beads},xx,\text{mp}}$) were calculated. The lateral strain considers the y-component, which is defined as the stretching direction, whereas the longitudinal strain examines the x-component, which is orthogonal to the stretching direction. These determined strains were then plotted against mp.

3.5.2 Digital Image Correlation

To evaluate small beads, digital image correlation (DIC) was used. DIC is a widely used technique to study a substrate's deformation, which is based on an image registration algorithm for tracking displacements between an undeformed reference image and a deformed current image.[150,151] It allows for the study of the deformation of a diversity of materials at different length scales ranging from meters to nanoscale.[152,153] Due to challenges, the standard DIC required modification, thus, a improved 2D subset based DIC software package (Ncorr) was developed by BLABER *et al.*.[154]

In subset-based DIC, the reference image is divided into small regions, *i.e.*, into so-called subsets (circular groups of points). Then, the linear, first-order transformation of the coordinates of the points is tracked in the deformed current image. The basic steps of the DIC algorithm implemented in Ncorr are shown in Fig. 3.19. First, an initial guess for the displacement is found, which is used as the initial input in the iterative optimization scheme, followed by the refinement solution, which allows for subset deformation.[154]

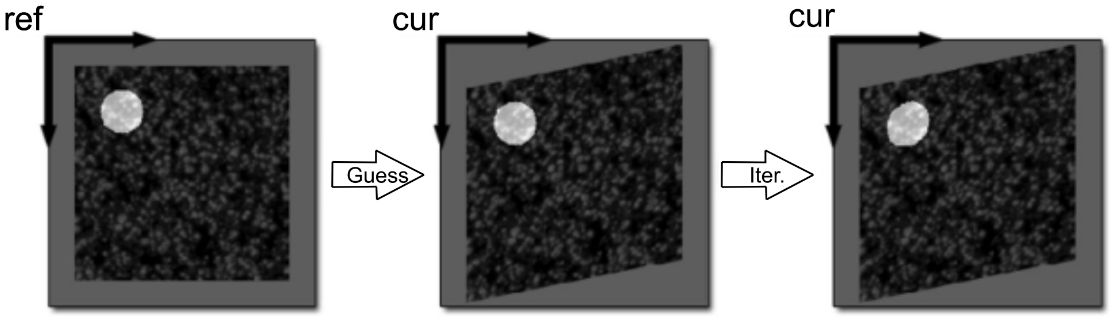

Fig. 3.19: Steps of a digital image correlation (DIC) algorithm, starting with finding an initial guess for the displacement in the current image. This is the initial input to the iterative optimization scheme, which refinds solutions that enable subset deformation.[154]

To find the initial guess followed by refinement, two different criteria had to be fulfilled (cf. Eq. 3.17 and Eq. 3.19).[154]

$$C_{\mathrm{cc}} = \frac{\sum_{(i,j)\in S}(f(\tilde{x}_{\mathrm{ref,i}}, \tilde{y}_{\mathrm{ref,j}}) - f_{\mathrm{m}})(g(\tilde{x}_{\mathrm{cur,i}}, \tilde{y}_{\mathrm{cur,j}}) - g_m)}{\sqrt{\sum_{(i,j)\in S}[f(\tilde{x}_{\mathrm{ref,i}}, \tilde{y}_{\mathrm{ref,j}}) - f_{\mathrm{m}}]^2 \sum_{(i,j)\in S}[g(\tilde{x}_{\mathrm{cur,i}}, \tilde{x}_{\mathrm{cur,j}}) - g_{\mathrm{m}}]^2}} \tag{3.17}$$

Here, $\tilde{x}_{ref,i}$ and $\tilde{y}_{ref,j}$ are the x and y-coordinates of a deformed reference point, whereas $\tilde{x}_{cur,i}$ and $\tilde{y}_{cur,j}$ are the coordinates of current subsets. f and g correspond to reference and current gray scale intensity functions at a certain location (x, y), respectively. The mean gray scale values are given by f_m and g_m (cf. Eq. 3.18).[154]

$$\begin{aligned} f_\mathrm{m} &= \frac{\sum_{(i,j)\in S}(f(\tilde{x}_\mathrm{ref,i}, \tilde{y}_\mathrm{ref,j})}{n(S)} \\ g_\mathrm{m} &= \frac{\sum_{(i,j)\in S}(g(\tilde{x}_\mathrm{ref,i}, \tilde{y}_\mathrm{ref,j})}{n(S)} \end{aligned} \tag{3.18}$$

$n(S)$ is defined as the number of data points in subset S. Horizontal (u, x-direction) and vertical (v, y-direction) displacements with pixel accuracy are provided by the initial guess. Refinement of the results with sub-pixel resolution occurs by extracting the minimum of a correlation criteria (C_LS) that correlated to C_CC (cf. Eq. 3.19).[154]

$$C_\mathrm{LS} = \sum_{(i,j)\in S} \left[\frac{f(\tilde{x}_\mathrm{ref,i}, \tilde{y}_\mathrm{ref,j}) - f_\mathrm{m}}{\sqrt{\sum_{(i,j)\in S}[f(\tilde{x}_\mathrm{ref,i}, \tilde{y}_\mathrm{ref,j}) - f_\mathrm{m}]^2}} - \frac{g(\tilde{x}_\mathrm{ref,i}, \tilde{y}_\mathrm{ref,j}) - g_\mathrm{m}}{\sqrt{\sum_{(i,j)\in S}[g(\tilde{x}_\mathrm{ref,i}, \tilde{y}_\mathrm{ref,j}) - g_\mathrm{m}]^2}} \right]^2 \tag{3.19}$$

In the process of finding the initial guess, a reference subset is fully size-padded and convolved with the current image to obtain the normalized cross-correlation at integer digits (NCC). By finding the maximum correlation coefficient, the position of the subset is recreated with respect to the current configuration. Thus, the output image is an array of correlation coefficients (cf. Fig. 3.20).[154]

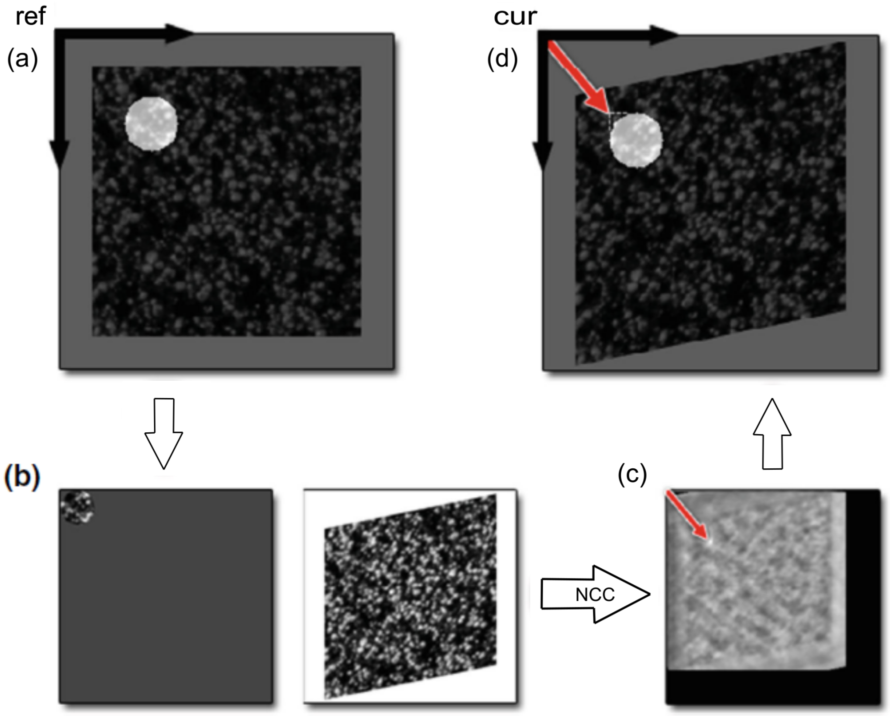

Fig. 3.20: Scheme to find the initial guess. The reference subset (a) is scaled up to full size (b) and convoluted with the current image (c) to yield the normalized cross-correlation leading to an output image, which is basically an array of correlation values. The maximum correlation coefficient is used to recreate the position of the subset.[154]

The strains are obtained by using GREEN-LANGRANIAN strains involving displacement gradients (cf. Eq. 3.20/3.21).[154] Since in standard DIC, the obtained displacement gradients are noisy and require smoothening, Ncorr makes use of the strain subwindow algorithm proposed by PAN *et al.*[154,155]

$$E_{xx} = \frac{1}{2}\left(2\frac{\partial u}{\partial x} + \left(\frac{\partial u}{\partial x}\right)^2 + \left(\frac{\partial v}{\partial x}\right)^2\right) \tag{3.20}$$

$$E_{yy} = \frac{1}{2}\left(2\frac{\partial v}{\partial y} + \left(\frac{\partial u}{\partial y}\right)^2 + \left(\frac{\partial v}{\partial y}\right)^2\right) \tag{3.21}$$

3.5.3 Determination of Contour and Apparent Persistence Lengths

The determination of the contour and apparent persistence lengths of the membrane-bound VIFs was based on Easyworm, an open-source software tool developed by LAMOUR.[156] By using the *ImageJ* plugin *JFilament*, the detected filaments were traced and the x- and y-coordinates of the filaments were extracted at different applied strain. These extracted coordinates were used to calculate the contour and apparent persistence lengths. To obtain the contour length (L_C), the sum of the distances between two neighboring coordinates (L_{ij}) was calculated according to the following Eq. 3.22.

$$L_C = \sum_{i=0}^{j} L_{ij} \tag{3.22}$$

The persistence lengths of the filaments were derived from the worm-like chain (WLC) model for semi-flexible filaments. Considering flexible polymers according to LAMOUR (cf. Eq. 3.23), the tangent-tangent decay was monitored.

$$< \cos\theta(\Delta s) >= \exp\left(-\frac{\Delta s}{L_P}\right) \tag{3.23}$$

The angle θ is the angle between two segments separated by a contour length of segment Δs (cf. Fig. 3.21). θ_1 defines the angle between two tangents (green-cyan) separated by Δs, whereas θ_1 describes the angle between two other vectors (cyan-blue). They are distanced by $2 \cdot \Delta s$. This is propagated until the last possible tangent.

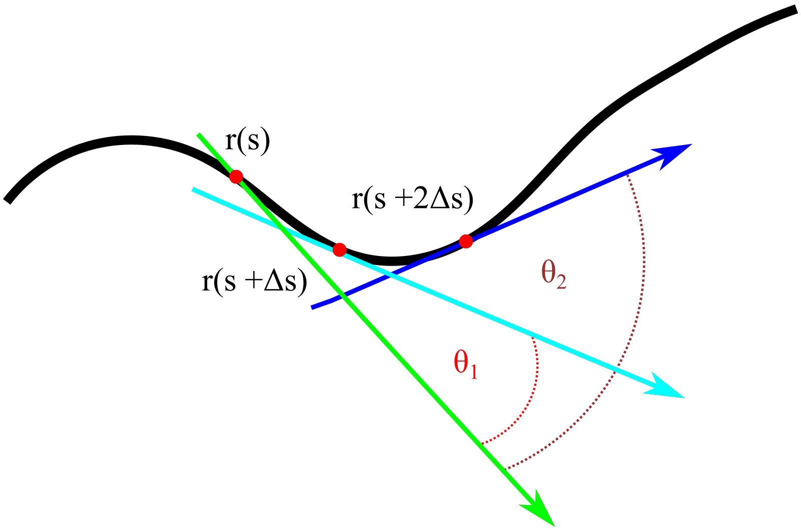

Fig. 3.21: Determination of the apparent persistence lengths of membrane-bound vimentin intermediate filaments based on Easyworm by monitoring the decay of tangent-tangent correlations derived from the worm-like chain (WLC) model for semi-flexible polymers.[156] θ_1 defines the angle between two tangents (green-cyan) that are separated by Δs, whereas θ_1 describes the angle between two vectors (cyan-blue) distanced by $2 \cdot \Delta s$. This is propagated until the last possible tangent, *i.e.*, the step size is increased until the end of the filament of interest.

Since L_P is unknown and the parameter to be calculated, $< \cos\theta(\Delta s) >$ was determined, as given in Eq. 3.24. Therefore, Δs was increased stepwise by x.

$$< \cos\theta(\Delta s) >= r(s) \cdot r(s + x \cdot \Delta s) \tag{3.24}$$

Hence, the apparent persistence length of membrane-bound VIFs was obtained (cf. Eq. 3.25).

$$L_\mathrm{P} = -\frac{\Delta s}{\ln(< \cos\theta(\Delta s) >)} \tag{3.25}$$

3.5.4 Theoretical Strain Displacement

For theoretical determination of the displacement of the coordinates of individual filaments upon uniaxial stretch, Eq. 3.26 was used. The coordinates (x, y) are transformed by applying the lateral ($\epsilon_{\mathrm{beads},yy}$) and longitudinal strains ($\epsilon_{\mathrm{beads},xx}$), derived from the evaluation of the beads. To compare the transformed filament with the actually strained filament, the transformed filament was plotted together with the unstrained and strained filament.

$$
\begin{aligned}
x_{\text{theo, mp}} &= x_0 \cdot \epsilon_{\text{beads},xx} + x_0 \\
y_{\text{theo, mp}} &= y_0 \cdot \epsilon_{\text{beads},yy} + y_0
\end{aligned}
\tag{3.26}
$$

Here, x_0 and y_0 are the x and y-coordinates in the unstretched state, respectively, used to obtain the theoretical coordinates $(x_{\text{theo, mp}}, y_{\text{theo, mp}})$ at different motor positions (mp).

3.5.5 Segmentation of Vimentin Intermediate Filaments

To analyze the orientation dependence of the membrane-bound VIFs, they were segmented. The segmentation occurs by taking the angle change into account. By going along a filament, the angle change is considered once it reaches a change greater than 5°, the current segment is completed, and a new segment is started. As shown in Fig. 3.22, an exemplary filament in the unstretched (cyan) and stretched (magenta) is segmented.

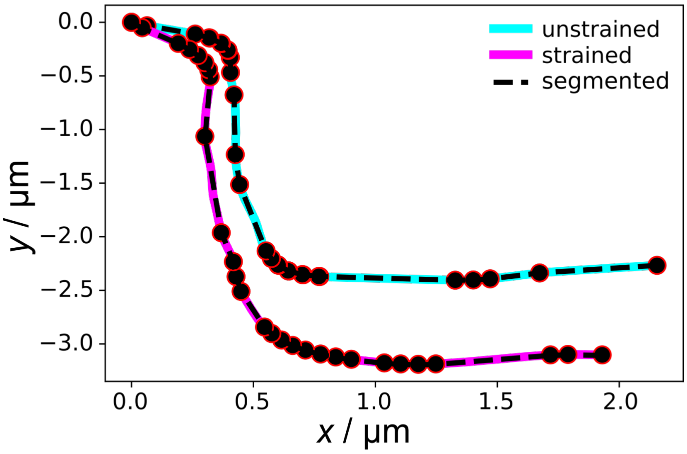

Fig. 3.22: Segmentation of the filaments in the unstretched (cyan) and stretched states (magenta) considering the angle change. The dashed line between the filled circles are the found segments within the filament. The filled circle serves as a marker at which the angle change is recognized to be higher than 5°. The number of segments found for unstretched filaments is not the same as for the filaments in the stretched state.

The black dashed lines between a filled circle show the different identified segments. A filled circle is placed on the coordinate, where an angle change was recognized to be greater than the set angle is recognized. Due to reorientation, straining, and lack of markers on the filament, the segments found in the strained state differ from the ones in the unstrained state.

3.5.6 Pixel-wise Height Distribution

In order to extract the height profile of the VIF networks from the obtained atomic force micrographs, the images were analyzed by the tube filter algorithm. The tube filter algorithm was developed and kindly provided by PROF. DR. BURKHARD GEIL (Institute for Physical Chemistry, Georg-August University Göttingen). It is derived from the HESSIAN image matrix ($H(x, y)$, cf. Eq. 3.27), which represents the 3D superficial curvature of the input image ($I(x, y)$).

$$H(x,y) = \begin{bmatrix} \frac{\delta^2 I}{\delta x^2}(x,y) & \frac{\delta^2 I}{\delta y \delta x}(x,y) \\ \frac{\delta^2 I}{\delta x \delta y}(x,y) & \frac{\delta^2 I}{\delta y^2}(x,y) \end{bmatrix} \tag{3.27}$$

This surface curvature depends on the intensity. The tube-filtered image was obtained by determining the pixel-wise minimal curvature (cf. Fig. 3.23, step 1). Next, the obtained tube filtered image was thresholded (cf. Fig. 3.23, step 2), which was then served as a mask for the original image (cf. Fig. 3.23, step 3). This resulted in an output image, from which the background was removed and only showed the filaments and higher structures (cf. Fig. 3.23, step 4). Based on their intensities, the values were extracted and converted into height, finally resulting in a height profile. The individual height profiles were pooled together and plotted in a histogram.

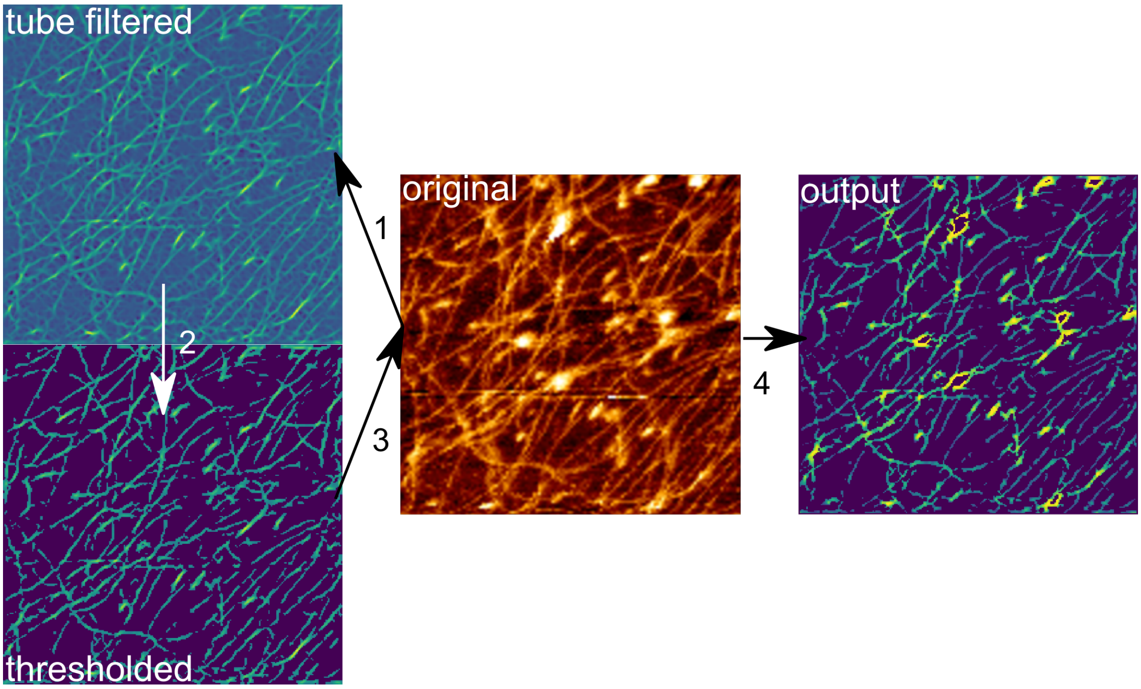

Fig. 3.23: Basic steps of the analysis of the pixel-wise height distribution of vimentin intermediate filament networks attached to the lipid bilayer. The first step is the exposure of the original image to the tube filter algorithm. Then, the obtained tube filtered image was thresholded (step 2), which was used as a mask for the original image (step 3). This resulted in an output image with the removed background showing only the structures of interest.

4 Results

In cells, intermediate filaments (IFs) are found to bind to the plasma membrane *via* desmosomes, indirectly or *via* other linker systems.[24,39] Therefore, in the course of this work, vimentin intermediate filaments (VIFs) were studied, particularly concerning their change in structural properties and mechanical response by applying external strains. To study that, an *in vitro* artificial model system was established (cf. Fig. 4.1). First, artificial membranes composed of POPC:DOPE biotinyl cap:dye (96:3:1, *n*/*n*) were prepared on hydrophilic polydimethylsiloxane (PDMS). VIFs coupled to ATTO647N (10 wt%) and biotin (5 wt%) were then attached to the biotin-decorated lipid bilayer *via* the linker neutravidin. Lateral stretching of membrane-bound VIFs in the presence of lipid reservoir in the form of small unilamellar vesicles (SUVs, POPC:ATTO488, 99:1, *n*/*n*) was achieved by a uniaxial, motorized stretching device (cf. Fig. 3.5, chapter 3.1.2).

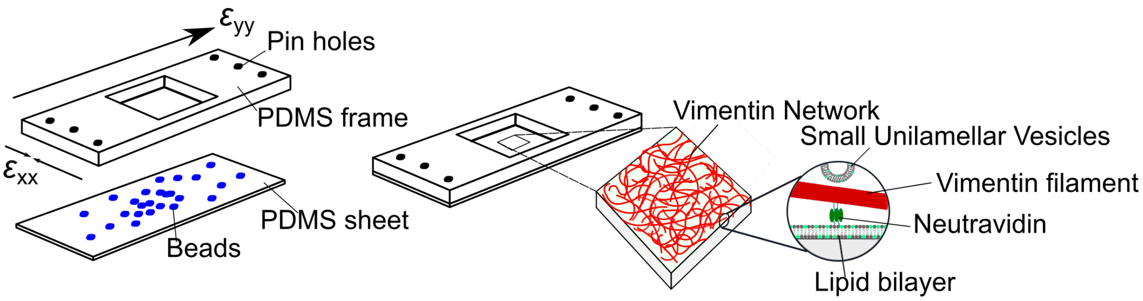

Fig. 4.1: *In vitro* experimental system. Elastic polydimethylsiloxane (PDMS)) chamber consisting of a PDMS frame with pin holes for the attachment to the stretching device and a PDMS sheet (thickness: 200 µm) in which fluorescent beads (blue, diameter in 4 µm) are embedded (*left*) The biotinylated vimentin intermediate filaments (VIFs) connected to the supported lipid bilayer (POPC:biotinyl cap-DOPE:dye, 96:3:1, *n*/*n*) *via* biotin-neutravidin-biotin linkages were prepared on the PDMS sheet. The addition of small unilamellar vesicles, which do not contain biotinylated lipids, to the membrane-bound VIFs serves as a lipid reservoir (*right*). This composite system was laterally stretched by a uniaxial stretching device.

4.1 Characteristics of Uniaxial Stretching

PDMS is a commonly used elastomer in biological science. In this work, PDMS is used as solid support for preparation and mainly for lateral stretching of the artificial model system. It is assumed that the applied strain coming from the motor is only an approximation and that the applied strain is not entirely but only partly transferred to the PDMS. Thus, to better understand the uniaxial stretching and the loss of transmission strain, the stretching parameters were characterized and defined using the CAUCHY strain definition (cf. Eq. 3.16 in chapter 3.5.1).

For a stepwise uniaxial stretching of the membrane-bound VIFs, a motorized stretching device was used, on which a pre-stretching device with a PDMS chamber was mounted (cf. chapter 3.1.2). Fluorescently labeled beads (blue, 4 µm in diameter) were embedded in the PDMS sheet as optical trackers, and their local positions were detected by confocal laser scanning microscopy (CLSM) as a function of different motor positions (mp) (cf. Fig. 4.2 A). From the trajectories of the tracked bead positions, a displacement field relative to a reference bead was derived, which is characteristic of a uniaxial stretching device based on PDMS (cf. Fig. 4.2 B). Beads that are located on the cross-hair ($x = 0$, y or x, $y = 0$) move along the axes, either away from the reference bead along the y-axis (longitudinal) or towards the reference bead along x-axis (lateral), while beads in between the cross-hairs move in both x- and y-direction. From the displacement field, the longitudinal (y-component) and the lateral strain (x-component) were calculated according to Eq. 3.16 in chapter 3.5.1 (cf. Fig. 4.2 C). The magnitude of the longitudinal strain ($\epsilon_{\text{beads},yy}$) increased linearly with increased mp, whereas the lateral strain ($\epsilon_{\text{beads},xx}$) decreased linearly indicating compression. Upon uniaxial stretch up to mp = 10 nm, a longitudinal and lateral strain of 35 ± 10 % and -14 ± 4% were found, respectively.

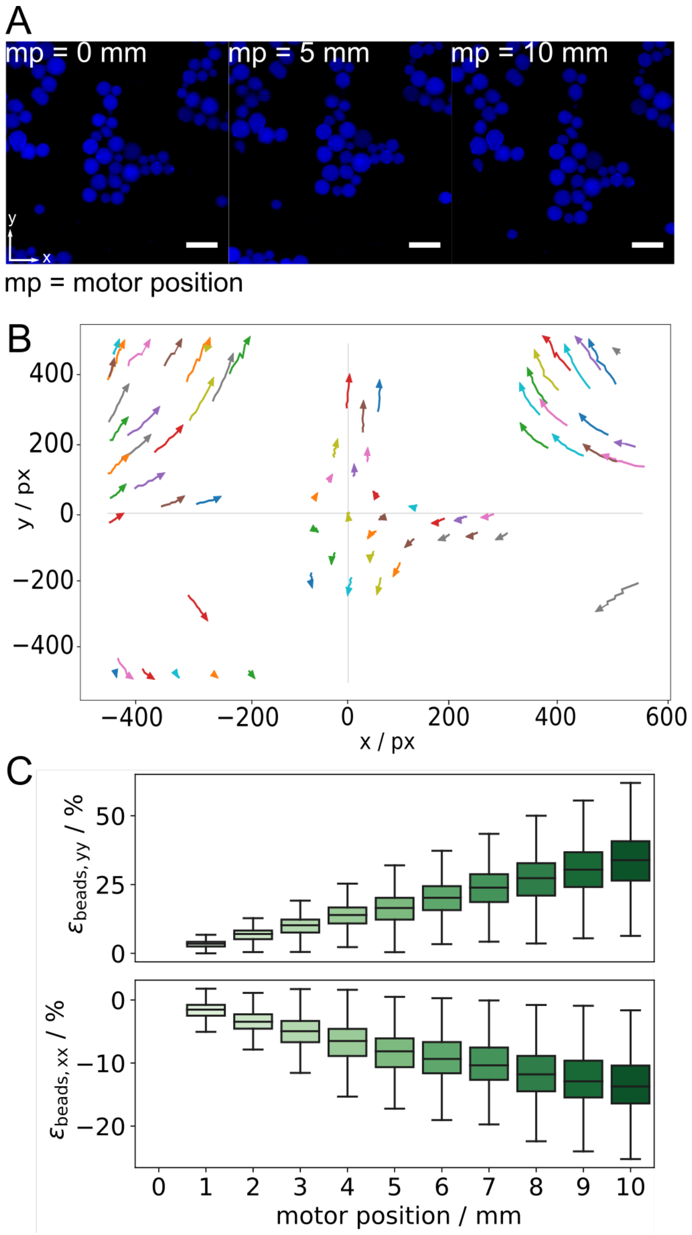

Fig. 4.2: Characteristic of uniaxial stretching. (**A**) Confocal fluorescence micrographs of the beads (blue, 4 µm in diameter) in the unstretched (motor position: mp = 0 mm) and stretched (mp = 5 mm and mp = 10 mm) states. Stretching direction is the y-axis; scale bars: 10 µm. (**B**) A displacement field was obtained by tracking the beads with respect to a reference bead. Beads positioned on the crosshair moved either away from the reference bead along the y-axis or towards the reference bead along the x-axis. The other beads located between the crosshair moved in both x- and y-direction. (**C**) longitudinal ($\epsilon_{\mathrm{beads},yy}$) and lateral strain ($\epsilon_{\mathrm{beads},xx}$) were plotted against the motor position. The magnitude of the longitudinal strain increased linearly with increasing motor position, while the magnitude of the lateral strain decreased linearly with increasing motor position. When stretched up to 10 mm, a longitudinal strain of 35 ± 10 % and a lateral strain of -14 ± 4% were determined ($n = 20$).

Due to the heterogeneity of the distribution of the beads within the PDMS, showing areas without any located beads, the obtained results were cross-validated with PDMS embedding small polystyrol beads (red, 100 nm in diameter,Thermo Fisher Scientific, Waltham, USA), which undergoes a uniaxial stretch. Fluorescence micrographs at different mp up to mp = 10 mm were recorded. Micrographs at mp = 0 mm and mp = 10 mm are shown in Fig. 4.3.

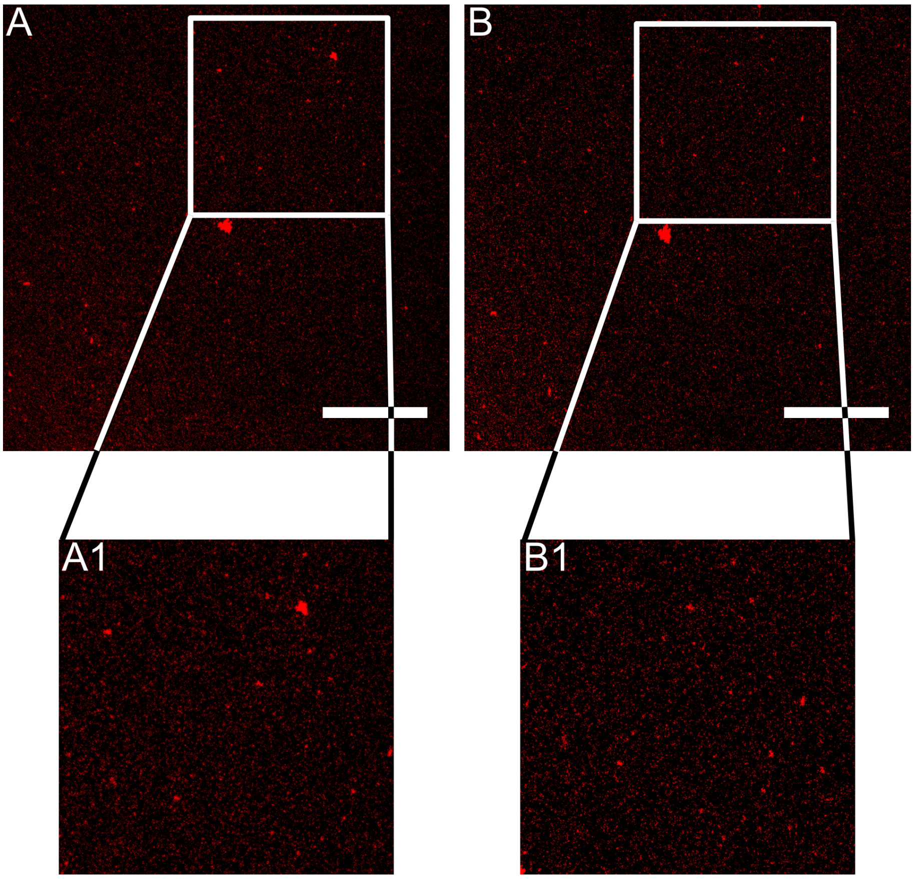

Fig. 4.3: Confocal fluorescence micrographs of the polystyrol beads (red, 100 nm in diameter) in the (**A**) unstretched (mp = 0 mm) and (**B**) stretched (mp = 10 nm) states; scale bars: 50 µm. For better visualization zoom-ins (**A1**/**B1**) were shown. The small beads are homogeneously distributed. Brighter fluorescence was assigned to aggregated or accumulated beads.

The fluorescence images showed homogeneously distributed beads in the whole field of view. Brighter fluorescence intensities were assigned to aggregated beads. Using digital image correlation (DIC, cf. chapter 3.5.2) by applying the GREEN-LANGRANGIAN strains (cf. Eq. 3.20/3.21, chapter 3.5.2), revealed that the magnitude of longitudinal and lateral strains alter with increased mp: an increased magnitude of longitudinal strain up to roughly 44% (cf. Fig. 4.4 A) and a decreased magnitude of lateral strain up to -12% were obtained (cf. Fig. 4.4 B) at mp = 10 mm. Even though smaller beads were homogeneously distributed within the PDMS, the strain distribution over the sample appeared heterogeneous. However, since smaller beads gave similar results as with larger beads, with small deviations, the latter ones were used for further experiments because they were easier to track when the PDMS chamber was stretched at a higher strain rate.

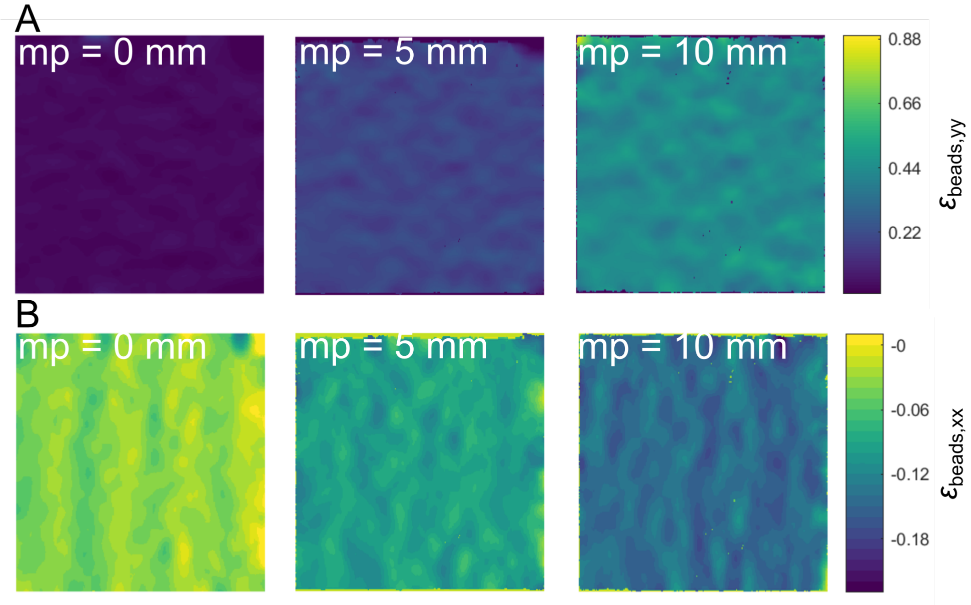

Fig. 4.4: Characteristics of uniaxial stretching using small bead size (100 nm) analyzed by digital image correlation (DIC). Strain distribution of unstrained (motor position: mp = 0 mm, *left*), at mp = 5 mm (*center*) and at mp = 10 nm (*right*), which was heterogeneous. The magnitude of the longitudinal strain ($\epsilon_{\text{beads},yy}$, **A**) increased with increasing mp with the maximal longitudinal strain found as roughly 44%, while the magnitude of the lateral strain ($\epsilon_{\text{beads},xx}$, **B**) decreased with increasing mp, showing a lateral strain of around -12% at mp = 10 mm.

4.2 Supported Lipid Bilayer under Strain

To decipher the response of a lipid bilayer to external strain, *in vitro* stretching experiments were performed with a lipid bilayer that was composed of POPC:DOPE biotinyl cap:ATTO488-DOPE (96:3:1, *n*/*n*) on an elastic, hydrophilic PDMS substrate. POPC was used as it is one of the lipids predominantly contained in biological membranes.[157] Previous *in vitro* studies have revealed that a lipid bilayer can only be stretched up to 4-6 %[158–160] and that it exhibits two different behaviors on PDMS when stretched.[161]

4.2.1 Sliding and Sticky Membranes: A Study by Varying the Plasma Exposure

Stretching experiments of lipid bilayers on PDMS under strain by varying plasma settings were carried out by* LEA REPENNING *as part of her Bachelor thesis.

STUBBINGTON *et al.* found that a lipid bilayer on PDMS can either slide over the PDMS surface without deformation as the substrate undergoes area changes (*i.e.*, sliding membranes), or it becomes fixed so that it closely follows the deformation changes of the PDMS substrate (*i.e.*, sticky membranes). The behavior, which a membrane shows, depends on the surface treatment with oxygen plasma.[161] The present work aimed at sticky lipid bilayers on PDMS supports since, unlike sliding membranes, sticky membranes will be able to transfer strains to the bound vimentin intermediate filaments for further experiments. Therefore, SUVs prepared, as described in chapter 3.2.2, were spread on PDMS previously treated with oxygen plasma. To find the optimal conditions for sticky membranes, plasma settings were varied, and the resulting membranes were imaged in unstrained and strained situations by means of CLSM. The confocal fluorescence micrographs obtained under unstretched and stretched conditions are given in Tab. 4.1. Depending on the applied plasma settings, sliding or sticky lipid bilayers on PDMS were formed, showing characteristic behaviors.

Tab. 4.1: Confocal fluorescence micrographs of lipid bilayers on polymethylsiloxane (PDMS) treated with different plasma conditions in the unstretched and stretched states. The supported artificial membranes on PDMS treated with 1 % generator power continued to show homogeneously distributed fluorescence intensity in the stretched state as in the unstretched state. In contrast, supported stretched membranes on PDMS treated with 20 % generator power displayed increased defects (almost circular) without any fluorescence intensity. Additionally, the higher the pressure, the more cracks (linear) appeared orthogonal to the stretching direction; scale bars: 10 µm.

Plasma Settings	**Unstrained**	**Strained**
0.3 mbar*, 1 %, 10 s*	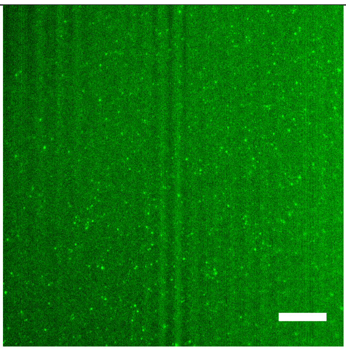	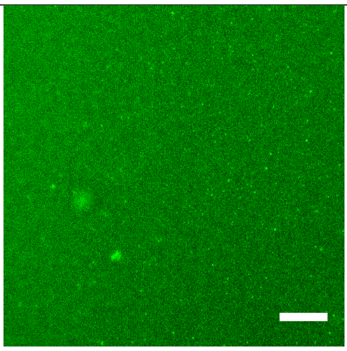
0.2 mbar, 20 %, 10 s	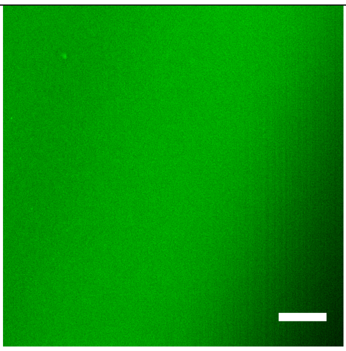	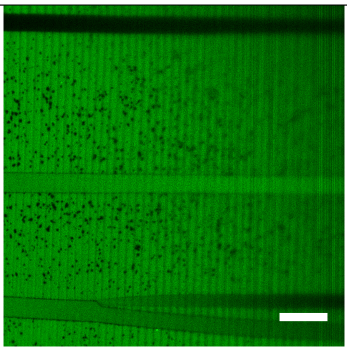
0.2 mbar, 20 %, 15 s	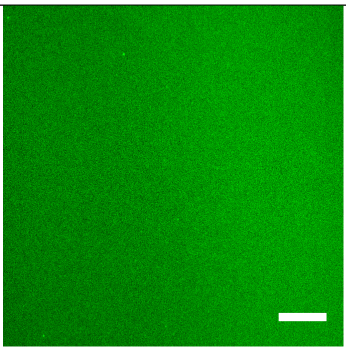	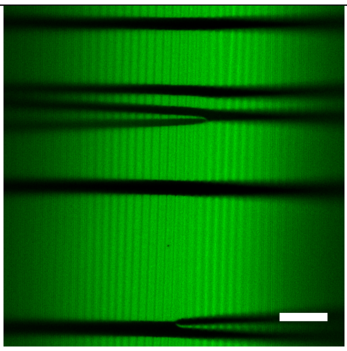

Plasma Settings	**Unstrained**	**Strained**
0.2 mbar, 20 %, 20 s	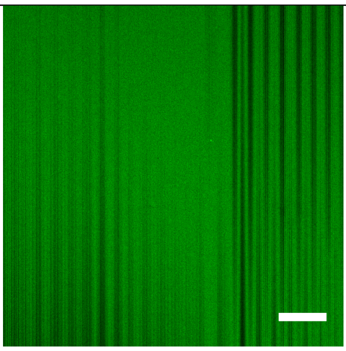	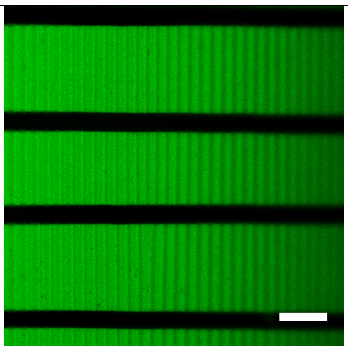
0.3 mbar, 20 %, 10 s	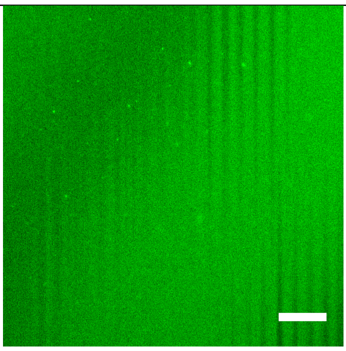	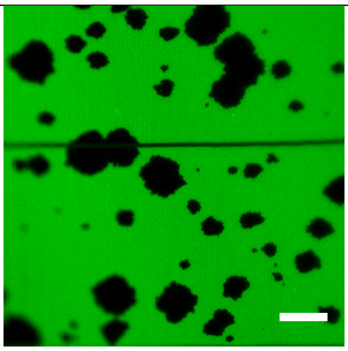
0.3 mbar, 20 %, 15 s	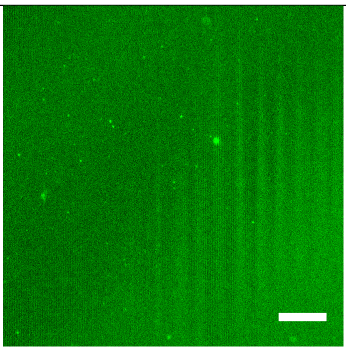	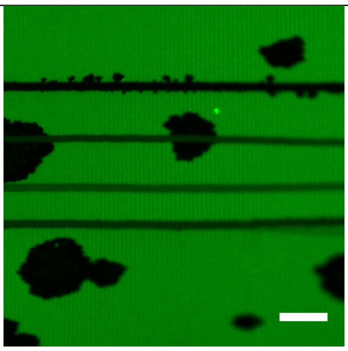
0.3 mbar, 20 %, 20 s	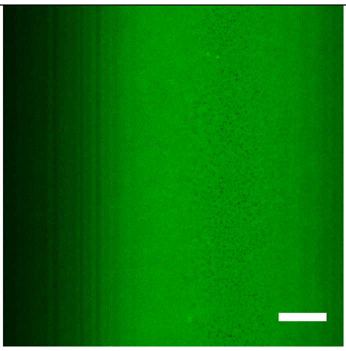	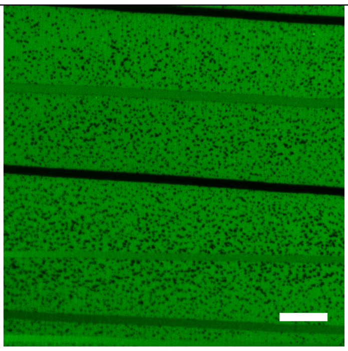

Plasma Settings	**Unstrained**	**Strained**
0.4 mbar, 20 %, 10 s	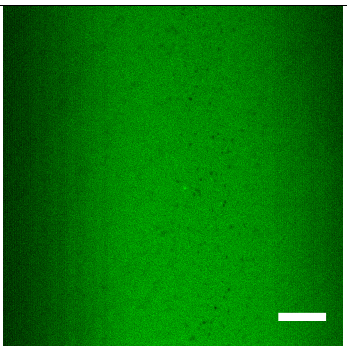	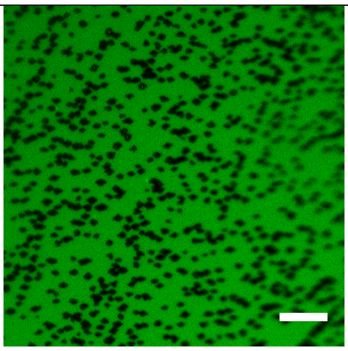
0.4 mbar, 20 %, 15 s	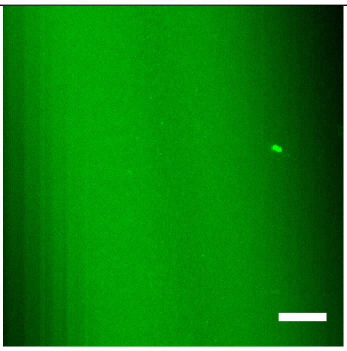	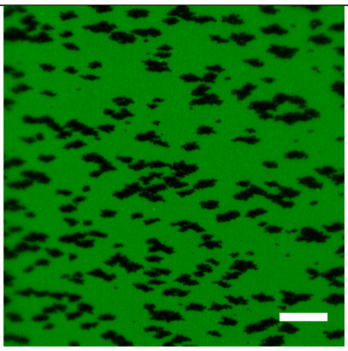
0.4 mbar, 20 %, 20 s	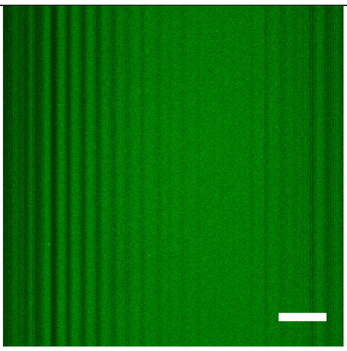	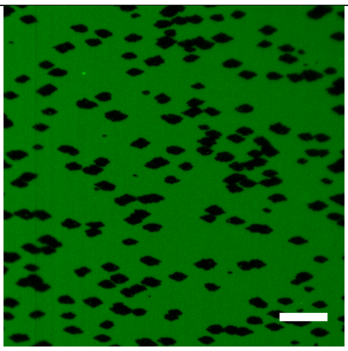

* variable parameters, when the generation power is 1 %. The lipid bilayer shows the same behavior.

In the unstrained state, all prepared lipid bilayers exhibited homogeneously distributed fluorescence intensities, while only a few brighter spots indicated the presence of adhered vesicles. However, upon stretching, they showed different behaviors depending on the applied plasma settings. The supported artificial lipid bilayers on PDMS treated with 1 % generator power showed homogeneously distributed fluorescence intensity even in the stretched state, which implies sliding. In contrast, stretched lipid bilayers on PDMS treated with 20 % generator power showed defects without any fluorescence intensity, showing stickiness of the lipid bilayer. Their number and size increased with higher motor position and plasma exposure time. An additional observation is that the lower the pressure was (0.2 mbar, 0.3 mbar), the more cracks appeared perpendicular to the stretching direction, which indicates cracks in the oxide layer.

Considering the results above, in further experiments, a plasma setting with a pressure of 0.4 mbar, a generator power of 20 %, and a treatment time of 20 s was used to render the PDMS surface hydrophilic (no cracks, but defects present when stretched). An exemplary fluorescence micrograph showing a lipid bilayer on plasma-treated PDMS in unstrained (mp = 0 mm) and strained (mp = 5 mm and mp = 10 mm) states is shown in Fig. 4.5. The membrane in the unstrained state is planar, and the green fluorescence intensity is homogeneously distributed (cf. Fig. 4.5 A), while the same supported bilayer formed defects without fluorescence intensity, whose number and area increased with increasing motor position (cf. Fig. 4.5 B/C).

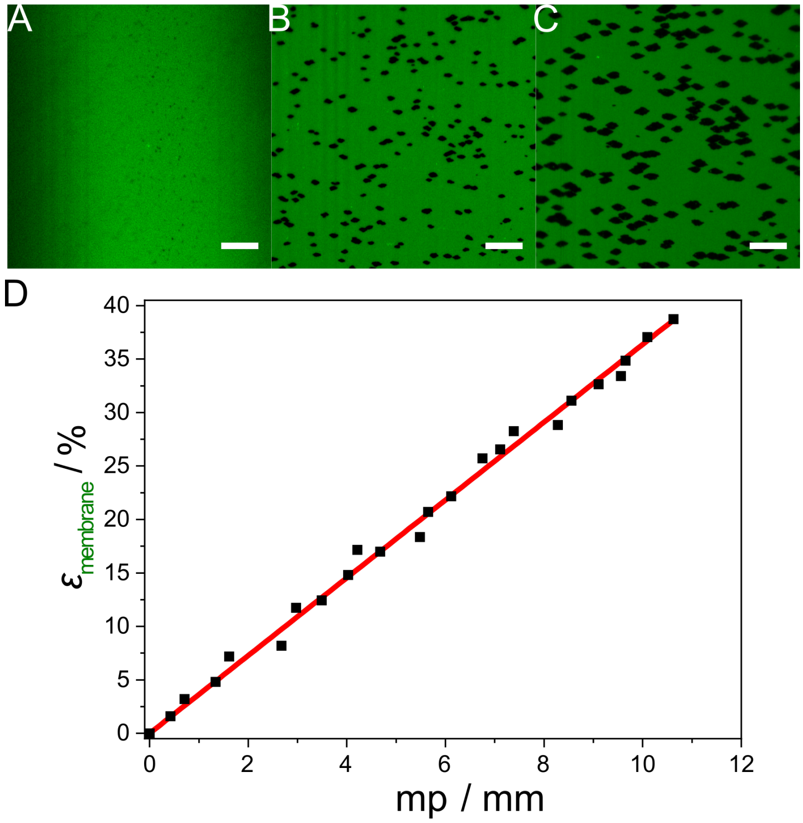

Fig. 4.5: Sticky lipid bilayer under strain. Example of confocal fluorescence micrographs showing a lipid bilayer (POPC:DOPE biotin cap: ATTO488, 96:3:1, *n*/*n*) on plasma-treated polymethylsiloxane (0.4 mbar, 20 %, 20 s) in an unstrained and a strained state. (**A**) Fluorescence micrograph of a lipid bilayer in the unstrained state, which was homogeneously distributed in fluorescence intensity. (**B**/**C**) Fluorescence micrographs of the same lipid bilayer in the strained state (mp = 5 mm, (**B**) and mp = 10 mm, (**C**)), which showed defects with increasing motor position (mp).(**D**) The strain of the specific membrane was calculated by determining the distances between two defects in the direction of strain analogous to Eq. 3.16 (cf. chapter 3.5.1) plotted against the mp, indicating a linear dependence between the deformation of the membrane and mp; scale bars: 10 µm.

In Fig. 4.5 D, the strain of the exemplary membrane, calculated by determining the distances between two defects in the direction of strain analogous to Eq. 3.16 (cf. chapter 3.5.1), was plotted against the motor positions, which is equivalent to the lateral strain ($\epsilon_{\text{beads},yy}$, cf. Fig. 4.2, chapter 4.1) in direction of stretching. The obtained results indicate a linear dependence between the deformation of the lipid bilayer and the beads. The appearance of defects and their increased number upon stretching, as well as the linear correlation between the calculated strains of the membrane ($\epsilon_{\text{membrane}}$) and the beads in the direction of elongation, indicate that the supported bilayer is sticky on PDMS under the above-mentioned plasma conditions.

4.2.2 Supported Lipid Bilayer under Strain Using Lipid Reservoir

Since this work aims at studying the artificial membrane-bound vimentin system under high strains (cf. Fig. 4.1, chapter 4), it is necessary to stretch the membrane without rupturing. As already mentioned, in literature, it has been reported that a lipid bilayer is inelastic and can only be stretched up to 4-6% without rupturing.[159,160,162] Similar results were also obtained in this work (cf. chapter 4.2.1). However, cellular plasma membranes can be stretched well beyond 5% owing to membrane reservoirs. STAYKOVA *et al.* demonstrated that lipid bilayers on partly hydrophilic PDMS (sticky) could be stretched to a certain extent in the presence of SUVs without rupturing.[162] Thus, to allow the planar lipid bilayer on PDMS to be stretched beyond 4-6% without the formation of too many defects, a membrane reservoir was provided by the addition of SUVs to the aqueous phase. By spreading SUVs of POPC:DOPE biotinyl cap: ATTO647-DOPE (96:3:1, *n*/*n*), a lipid bilayer was prepared on PDMS, prior to which the PDMS sheet was oxidized with oxygen plasma (100% O_2, 0.4 mbar, 20 %, 20 s) rendering the surface hydrophilic. Successful spreading of the vesicles was verified by fluorescence micrographs (cf. Fig. 4.6 A, *top*), which show homogeneously distributed fluorescence intensities.

By means of fluorescence recovery after photobleaching (FRAP) experiments, a diffusion coefficient and a mobile fraction for an ATTO647-DOPE lipid in the PDMS-supported lipid bilayer were determined in the presence of a lipid reservoir. Therefore, a region of interest was bleached, and recovery of fluorescence intensity was recorded. To obtain the diffusion coefficient, the recovery curve was fitted with the SOUMPASIS fit to acquire the half-life of recovery ($\tau_{1/2}$). With $\tau_{1/2}$ and the bleach radius in hand, the diffusion coefficient was determined using Eq. 3.8 (cf. chapter 3.4.1.2). The mobile fraction was obtained by considering the postbleach steady-state fluorescence intensity, the initial postbleach fluorescence intensity, and the prebleach fluorescence intensity according to Eq. 3.11 (cf. chapter 3.4.1.2). The diffusion coefficient and mobile ratio were determined as 1.4 ± 0.2 µm$^2 \cdot$ s^{-1} and 91 ± 6 %, respectively (cf. Fig. 4.6 B, *unstrained*).

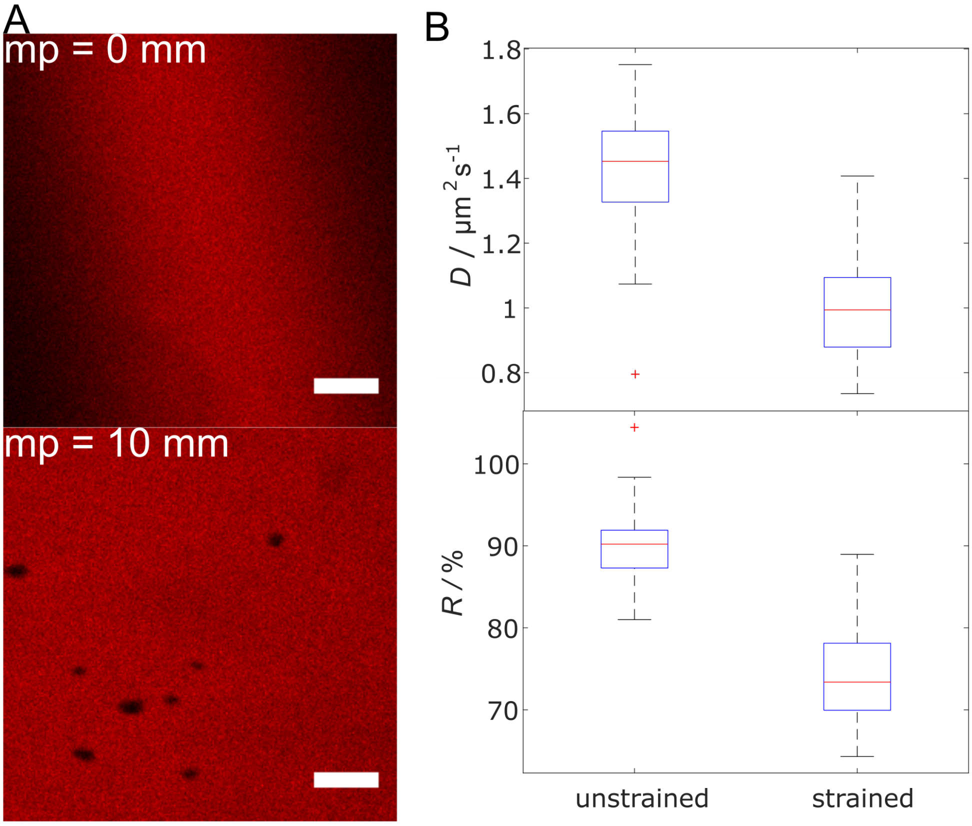

Fig. 4.6: Behavior of polymethylsiloxane (PDMS)-supported lipid bilayers composed of POPC:biotinyl cap DOPE:ATTO647 (96:3:1, *n*/*n*) upon uniaxial stretching in the presence of a lipid reservoir in form of small unilamellar vesicles (POPC:ATTO488-DOPE, 99:1, *n*/*n*). (**A**) Exemplary confocal fluorescence micrographs at motor position (mp) = 0 mm (*top*) and mp = 10 mm (*bottom*), scale bars: 5 µm. In the unstretched state (mp = 0 mm), the fluorescence was homogeneously distributed. However, the PDMS sheet was wrinkled, resulting in a limited focal plane. Upon stretching up to 10 mm, several small defects were formed that did not show any fluorescence intensity. (**B**) Boxplot of the diffusion coefficients and the mobile fraction in the unstrained and strained state. The central line (red) on each box represents the median, while the bottom and top edges of the box indicate the 25th and 75th percentiles, respectively. The whiskers are the data points that are not considered outliers marked with '+'. By performing fluorescence recovery after photobleaching, the diffusion coefficient and mobile fraction were found to decrease from 1.4 ± 0.2 µm$^2 \cdot$ s^{-1} (N = 15) and 91 ± 6 % (N = 15) to 1.0 ± 0.2 µm$^2 \cdot$ s^{-1} (N = 15) and 74 ± 7% (N = 15), respectively, upon stretching owing it to the formed defects.

If the bilayer is stretched in the presence of SUVs (POPC:ATTO488-DOPE, 99:1, *n*/*n*) the fluorescence images of the lipid bilayers (cf. Figs. 4.6 A, *bottom*/4.7 A) remain rather homogeneous with some defects that are filled with lipid material originating from the SUVs (cf. Fig. 4.7 B/C), The diffusion coefficient of the ATTO647-DOPE lipids were then determined by FRAP experiments to be 1.0 ± 0.2 µm$^2\cdot$ s^{-1} and the mobile fraction 74 ± 7% (cf. Fig. 4.6 B, *bottom*). Defects are discernable as black spots. Their number and size of the stretch-induced membrane defects are significantly lower than those found in stretched membranes in the absence of SUVs (cf. Fig. 4.5). Further support that the SUVs serve as a lipid reservoir for the stretched bilayer on PDMS, *i.e.*, that the SUVs integrate into the membrane is provided by FRAP (cf. Fig. 4.7 D). ATTO488-DOPE fluorescence is observed after stretching of the bilayer showing the transfer of ATTO488-DOPE lipids into the planar bilayer. Furthermore, a large fluorescence recovery (85 ± 7 %) of the ATTO488-DOPE fluorescence with a diffusion coefficient of 2.2 ± 0.7 $\mu m^2 \cdot s^{-1}$ is observed, thereby indicating a continuous lipid bilayer after stretching.

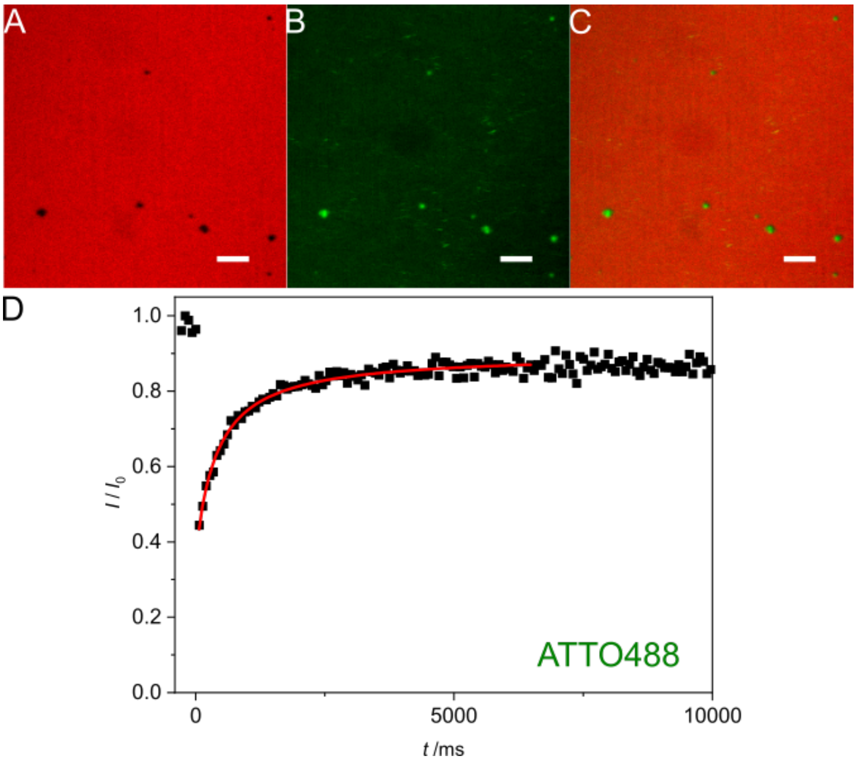

Fig. 4.7: Supported lipid bilayers under strain in the presence of lipid reservoir. (**A-C**) Fluorescence micrographs of a strained lipid bilayer (motor position: mp = 10 mm) composed of POPC:biotinyl cap-DOPE:ATTO647-DOPE (96:3:1, *n*/*n*) on oxidized polymethylsiloxane surface in the presence of small unilamellar vesicles (SUVs) serving as lipid reservoir (POPC:ATTO488-DOPE, 99:1, *n*/*n*). (**A**) ATTO647-DOPE fluorescence, (**B**) ATTO488-DOPE fluorescence and (**C**) superposition of (**A**) and (**B**) showing that defects (**A**, black) were filled with lipid material originating from the SUVs (**B**, green areas); scale bars: 10 µm. (**D**) Fluorescence recovery curve after photobleaching (FRAP) of the ATTO488-DOPE fluorescence. The FRAP curve was fitted according to SOUMPASIS (red) to obtain the half-life of recovery, which was then used to determine the diffusion coefficient. A diffusion coefficient of 2.2 ± 0.7 $\mu m^2 \cdot s^{-1}$ ($N = 9$) with a mobility fraction of 85 ± 7 % ($N = 9$) was obtained.

4.3 Supported Membrane-bound Vimentin Intermediate Filaments under Strain

4.3.1 Stretching of Membrane-bound Vimentin Intermediate Filaments Dependent on the Stretching Speed

Supported lipid bilayers, which can be stretched without significantly changing the integrity of the lipid bilayer, are a prerequisite for analyzing the influence of stretching on membrane-bound VIFs. First, fluorescently labeled VIFs were attached onto PDMS-supported lipid bilayers *via* biotin-neutravidin linkages, and fluorescence micrographs of the VIFs at different motor positions (mp) of membrane stretching were taken by CLSM. Micrographs at $\epsilon_{\text{beads}} = 0\ \%$, $\epsilon_{\text{beads}} = 2.9\ \%$, $\epsilon_{\text{beads}} = 6.4\ \%$, and $\epsilon_{\text{beads}} = 9.6\ \%$ are shown in Fig. 4.8 A1-4/B1-4. The confocal fluorescence micrographs confirmed the successful attachment of VIFs to the lipid bilayer. Filamentous structures with high fluorescence intensity and density are clearly visible. An example of a filament is shown in white. Dotty-like structures could be assigned to filaments directing out of the membrane plane and tetramers or unit-length filaments (ULFs). During the stepwise uniaxial stretching procedure ($\Delta\text{mp} = 1$ mm), the fluorescence density was slightly reduced due to neighboring ATTO647N-labeled monomers within a filament being displaced from each other. This was especially observed in Fig. 4.8 B1-4. To visualize the change of the highlighted filaments under a variety of strain, they were traced by using a *ImageJ* plugin *JFilament* and the extracted coordinates (x, y) were plotted starting from an origin (0,0) (cf. Fig. 4.8 A5/B5). The membrane-bound VIFs responded to the applied strain rather with a directional reorientation than undirected thermal fluctuations. They reoriented by following the PDMS stretching, as described in chapter 4.1; displacement towards the stretching direction (y-direction) was observed, while in x-direction, the filaments showed reorientation towards the center along the x-axis. Thus, the mechanical response was influenced by the x- (longitudinal) and y-component (lateral) of the strain. More precisely, the reorientation occurred depending on the angular orientation of the segments, which will be described in more detail in chapter 4.3.3.

To investigate the impact of stretching speed on the stretching of membrane-bound VIFs, either a low stretching speed of $v = 20\ \mu\text{m} \cdot \text{s}^{-1}$ or a faster speed of $v = 750\ \mu\text{m} \cdot \text{s}^{-1}$ was applied. The observation of reorientation was independent of the strain rate but showed to have an impact on the extent.

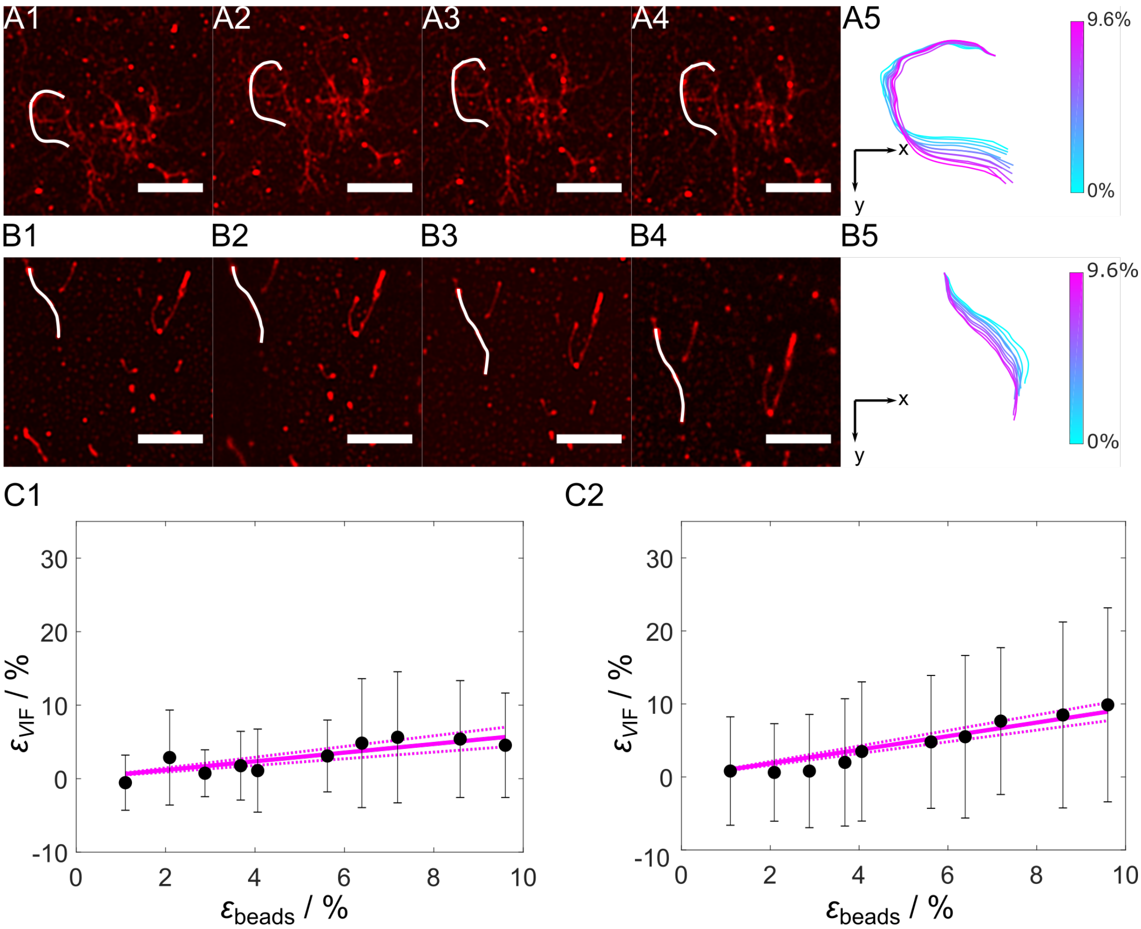

Fig. 4.8: Stretching of membrane-bound vimentin intermediate filaments (VIFs). Lipid composition: POPC:biotinyl cap-DOPE:ATTO488 (96:3:1, n/n). Biotinylated VIFs (10 wt% ATTO647N, 5wt % biotin) were attached to the lipid bilayer *via* neutravidin. (**A**) Fluorescence micrographs of a series of slow (stretching speed: $v = 20\,\mu\text{m} \cdot \text{s}^{-1}$) and (**B**) of fast ($v = 750\,\mu\text{m} \cdot \text{s}^{-1}$) stepwise stretching of selected membrane-bound VIFs. (**A1/B1**) Filaments at $\epsilon_{\text{beads}} = 0$ %, (**A2/B2**) Filaments at $\epsilon_{\text{beads}} = 2.9$ %, (**A3/B3**) Filaments at $\epsilon_{\text{beads}} = 6.4$ %, and (**A4/B4**) Filaments at $\epsilon_{\text{beads}} = 9.6$ %; scale bars: 5 µm. (**A5/B5**) The filaments highlighted in (**A**1-4/**B**1-4) were plotted starting from an origin (0,0) to observe the structural change. The filaments showed directional reorientation; color bars: $\epsilon_{\text{beads}} = 0 - 9.6$ %. (**C1**) Strain of VIFs as a function of ϵ_{beads} at slow stretching velocity ($N = 30$) and (**C2**) at fast stretching velocity ($N = 86$) indicating a linear dependence with a slope of 0.60 at low stretching speed and a slope of 0.93 at high stretching speed. The dashed lines are the 95% confidence bounds.

A semiflexible filament under strain is expected to react to stretching with elongation of its contour length. Thus, the change in the contour length is a well-suited parameter to study the strain of VIFs. Therefore, by determination of the contour lengths ($L_{\text{C,mp}}$) of the individual membrane-bound VIFs as a function of the applied strain given as ϵ_{beads}, the strain of the VIFs ϵ_{VIF} ($\epsilon_{\text{VIF}} = \Delta L_{\text{C,mp-0}}/L_{\text{C,0}}$) was calculated to study whether the filament itself gets altered upon stretching. The individual contour lengths at different motor positions were measured by using the coordinates of the traced filament obtained by *JFilament*. Therefore, the distances between two neighboring coordinates were summed up according to Eq. 3.22 (cf. chapter 3.5.3). At low stretching speed

($v = 20\ \mu\text{m} \cdot \text{s}^{-1}$), a linear behavior of ϵ_{VIF} (ϵ_{beads}) was found with a slope of 0.60 demonstrating that about 60 % of the applied strain is transmitted to the membrane-bound VIFs, corresponding to $\epsilon_{\text{VIF}} = 5.4 \pm 7.1$ % at mp = 10 mm ($\epsilon_{\text{beads}} = 9.6$ %, cf. Fig. 4.8 C1). Increasing the stretching speed to $v = 750\ \mu\text{m} \cdot \text{s}^{-1}$ still resulted in a linear dependency of ϵ_{VIF} (ϵ_{beads}), however with a larger slope of 0.93, which clearly showed that a significantly larger strain of 93 % is transferred to the VIFs, which equals to $\epsilon_{\text{VIF}} = 9.0 \pm 13.3$ % at mp = 10 mm ($\epsilon_{\text{beads}} = 9.6$ %, cf. Fig. 4.8 C2).

4.3.2 Stretching of Membrane-bound VIFs Dependent on the Pinning Point Density

Stretching experiments of membrane-bound VIFs on PDMS under strain by varying the biotin concentration within the filaments were carried out by* PAULINE ROTH *as part of her Bachelor thesis.

VIFs are connected to the lipid bilayer *via* neutravidin. As the biotin monomers within a VIF are statistically distributed, the hypothesis was investigated, which states that the response of membrane-bound VIFs depends on the pinning point density, *i.e.*, when the pinning point density is high, the VIFs would rather experience straining than reorientation. To prove this, stretching experiments were performed on membrane-bound VIFs that were connected *via* AlexaFluor 350-labeled neutravidin (cf. Fig. 4.9). The idea was to visualize the number of pinning points within the filaments connected to the lipid bilayer. To this end, accessibility to a quantitative analysis of the pinning point density could be realized to prove the aforementioned hypothesis.

However, the results demonstrated that the neutravidin is heterogeneously distributed, showing aggregated structures as well as filamentous structures (cf. Fig. 4.9 A2). An overlay of the neutravidin and the VIF fluorescence (cf. Fig. 4.9 A3) clearly confirms that the filamentous structures of the neutravidin fluorescence arose from the VIFs (cf. Fig. 4.9 A4). This presumably indicates an excessive neutravidin binding to VIFs, which possess free biotin monomers. Upon stretching, neutravidin was accumulated in the formed defects within a lipid bilayer (cf. Fig. 4.9 B), giving further evidence for excessive neutravidin in the system.

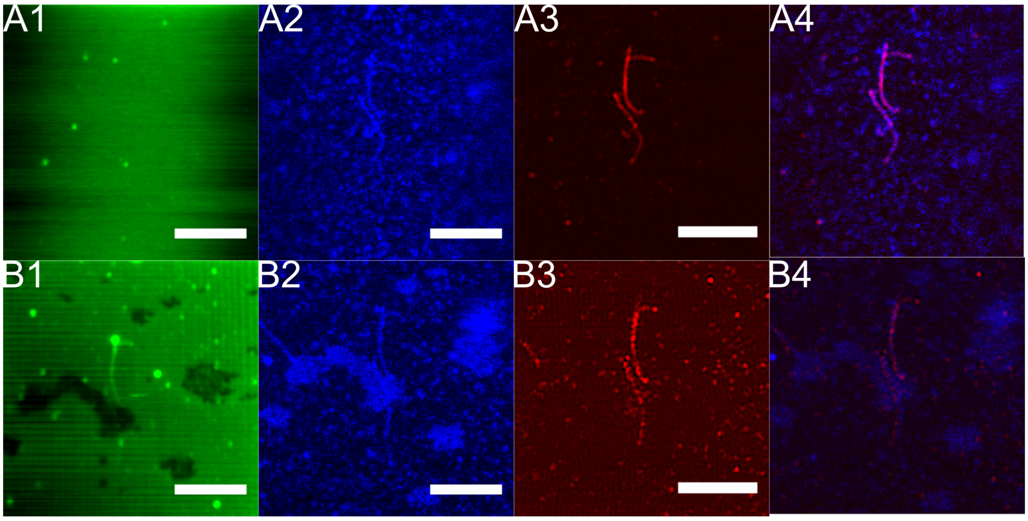

Fig. 4.9: Stretching of membrane-bound vimentin intermediate filaments (VIFs) connected by labelled neutravidin. Lipid composition: POPC:biotinyl cap-DOPE:ATTO488 (96:3:1, *n*/*n*). Biotinylated VIFs (10 wt% ATTO647N, 5 wt% biotin) were attached to the lipid bilayer *via* neutravidin (AlexaFluor 350). (**A**/**B**) Confocal fluorescence micrographs of lipid bilayer (**A1**/**B1**), neutravidin (**A2**/**B2**), VIFs (**A3**/**B3**), and a superposition (**A4**/**B4**) of (**A2**/**B2**) and (**A3**/**B3**) in the unstretched (**A**) and stretched (**B**) state; scale bars: 5 µm. The alignment of filamentous structures of neutravidin and VIFs and the accumulation of neutravidin in the defects formed upon stretching implies excessive neutravidin in the system.

The experiments above did not prove the hypothesis as mentioned earlier due to lack of resolution, as the pinning points cannot be resolved by CLSM. Therefore, stretching experiments with different biotin concentrations (5 wt%, 10 wt%, 15 wt%, and 20 wt%) were performed. Higher biotin concentration within a filament means higher pinning point density, which in turn means that higher strains should be observed. By measurement of the contour lengths of the individual membrane-bound VIFs as a function of the applied strain given as ϵ_{beads}, the obtained strains of VIFs (ϵ_{VIF}) showed that more strain was transferred to the VIFs when the biotin concentration was increased (cf. Fig 4.10 A). Experiments with 5 wt% biotin concentration revealed a slope (m) of 0.93 (cf. Figs. 4.10 A1/Fig. 4.8). For a biotin concentration of 10 wt%, a slope of $m = 1.43$ was obtained, demonstrating a strain transfer of 143 % (cf. Fig. 4.10 A2). Increasing the biotin concentration to 15 wt% resulted in a slope of $m = 1.10$, implying that 110 % of the applied beads strain is transferred to the VIFs (cf. Fig. 4.10 A3). A further increase led to the transmission of 143 %, as a slope of $m = 1.43$ was found (cf. Fig. 4.10 A4). The results showed that increasing the biotin concentration, *i.e.*, increasing the pinning point density led to larger strains that were transferred to VIFs. However, there was a discrepancy for VIFs with 15 wt% biotin. The transmission is lower than for those with 10 wt% and 20 wt% biotin, but nonetheless higher than for the ones with 5 wt% biotin. This observation only partly proves the hypothesis. Plotting the slopes in dependence of the biotin concentration revealed a curve that might go into saturation at the presented high biotin concentrations (cf. Fig 4.10 B). The curve was fitted with an exponential function ($y = -1.3 \cdot e^{-0.25 \cdot x} + 1.3$). Due to a lack of data points for lower concentrations, the fit needs to be seen as nothing more than a trend curve.

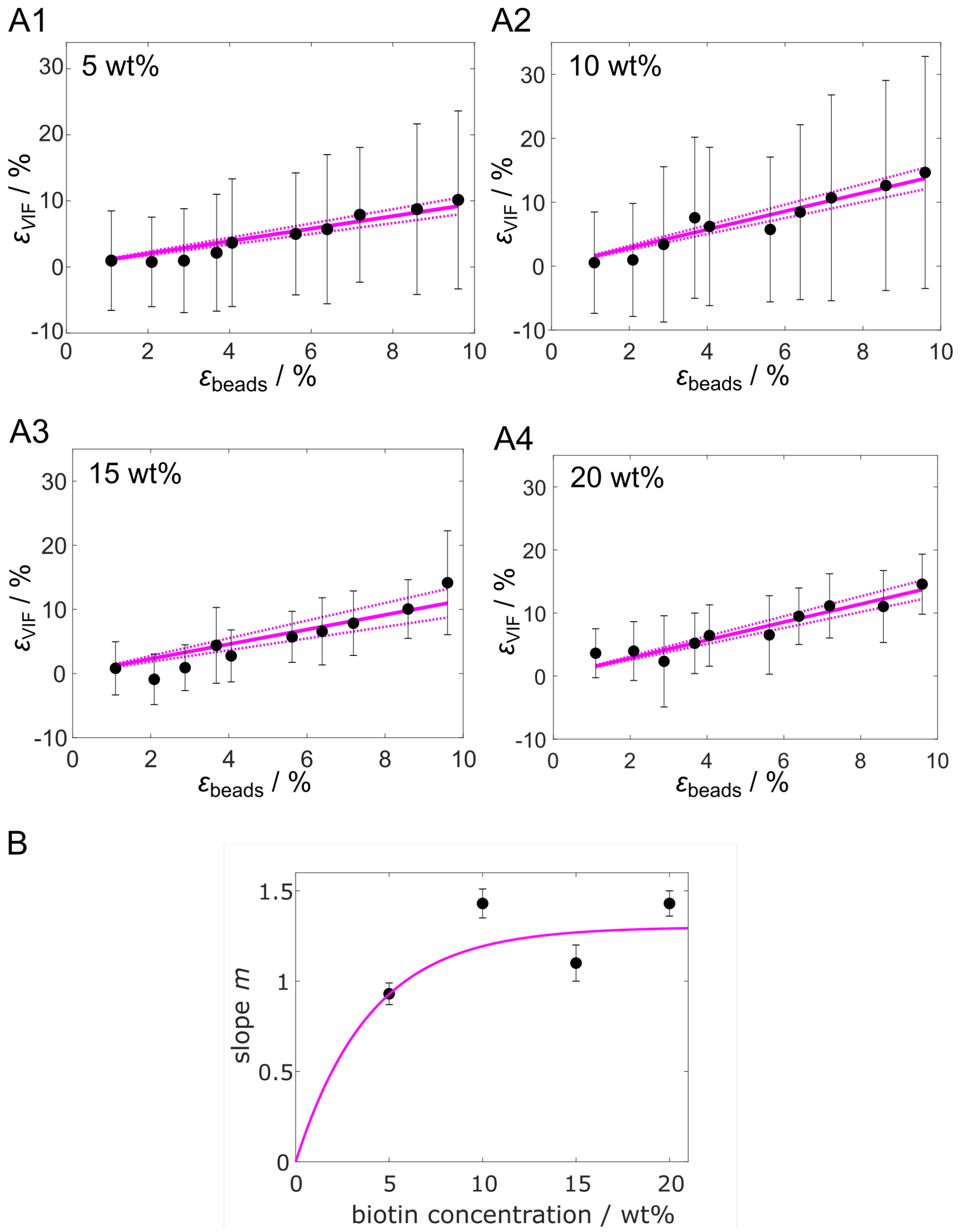

Fig. 4.10: (**A**)The strain of membrane-bound vimentin intermediate filaments (VIFs) in dependence of the biotin concentration within the filaments. **A1** Strain of VIFs with 5 wt% ($N = 86$); (**A2**) Strain of VIFs with 10 wt% ($N = 12$); (**A3**) Strain of VIFs with 15 wt% ($N = 12$); and (**A4**) Strain of VIFs with 20 wt% ($N = 12$) biotin monomers as a function of ϵ_{beads} indicating a linear dependence with a slope of 0.93, 1.43, 1.10, 1.43, respectively. (**B**) Representation of the found slope as a function of the biotin concentration. The data gave hints for saturation of the transmission strain. Therefore, the data points were fitted with an exponential function ($y = -1.3 \cdot e^{-0.25 \cdot x} + 1.3$), which is only for the purpose to show the trend.

Qualitative calculations were carried out to understand the deviations, assuming all points within a VIF are pinned. Applying the lateral and longitudinal strain obtained by beads tracking (cf. Fig. 4.2, chapter 4.1), the displacement of each coordinate in a filament was calculated according to Eq. 3.26 in chapter 3.5.4 (cf. Fig. 4.11). A superposition of the calculated contour of the strained VIFs (cf. Fig. 4.11, *e.g.*, magenta, dashed line) with the actual contour of a strained VIFs (cf. Fig. 4.11, *e.g.*, magenta, solid line) indicated that, qualitatively, higher pinning point density was present than in the cases, where no superposition was observed. This clearly demonstrated that, within one filament, the pinning points were heterogeneously scattered.

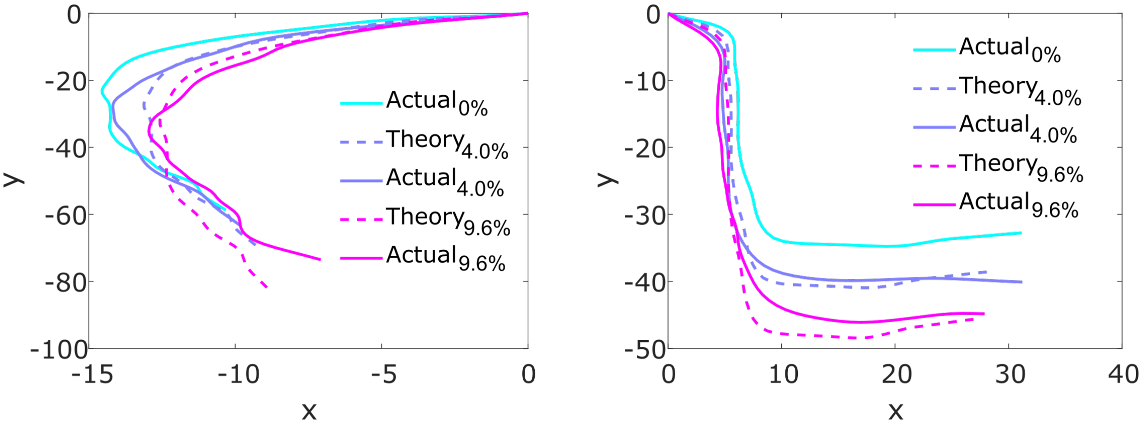

Fig. 4.11: Theoretical displacements of the contour of exemplary filaments by applying strain. The filament in the unstrained state is shown in cyan (solid line), and the strained states ($\epsilon_{\mathrm{VIF}} = 4.0\%$ and $\epsilon_{\mathrm{VIF}} = 9.6\%$) are highlighted in purple and magenta (solid line). The theoretical contours were calculated according to Eq. 3.26 (cf. chapter 3.5.4) and were shown in the same xy diagram (dashed line). If an overlap of theoretical and actual pinned filament contours was visible, a high pinning point density could be assumed. An example of a vimentin intermediate filaments with presumable low pinning point density (*left*) and with probable high pinning point density (*right*).

4.3.3 Reorientation of Membrane-bound VIFs during Stretching

As shown in Fig. 4.8 A/B, the orientation of the VIFs on the membrane with respect to the applied longitudinal and lateral strain is pivotal for its reorientation on the membrane. To quantitatively analyze this aspect, a circle was defined for the unstretched (u) PDMS sheet with radius $\epsilon_{\mathrm{xx},u} = \epsilon_{\mathrm{yy,u}}$ (cf. Fig. 4.13 A, *left*). Upon stretching (s) the circle transforms into an ellipse with $\epsilon_{\mathrm{beads},yy}$ for the lateral strain (semi-major axis) and $\epsilon_{\mathrm{beads},xx}$ for the longitudinal strain (semi-minor axis). The angle of zero strain (AZS) is defined as the vector pointing to the intersection of the circle and the ellipse and the y-axis. The AZS defines those orientations of the VIFs on the membrane, where the filament part experiences no strain. With this approach, three orientational cases of membrane-bound VIFs were defined with respect to the stretching direction: (i) if angles are larger than AZS, compression of the part of the VIFs occurs; (ii) if angles are smaller than AZS, the part of VIFs is stretched, and (iii) if the angle equals the AZS, neither compression nor stretching occurs (cf. Fig. 4.13 A, *right*).

In this work, an average apparent persistence length of the membrane-bound VIFs was determined as about 0.3 ± 0.04 µm (cf. Fig. 4.12, *left*). It was calculated according to LAMOUR based on the Easyworm software tool (cf. chapter 3.5.3).[156] Hence, those VIFs with an average contour length of 4.3 ± 1.9 µm (cf. Fig. 4.12, *right*) are not straight rods on the surface but bind in a "cooked spaghetti-like" manner. Thus, several angles with respect to the stretching direction were found within one filament.

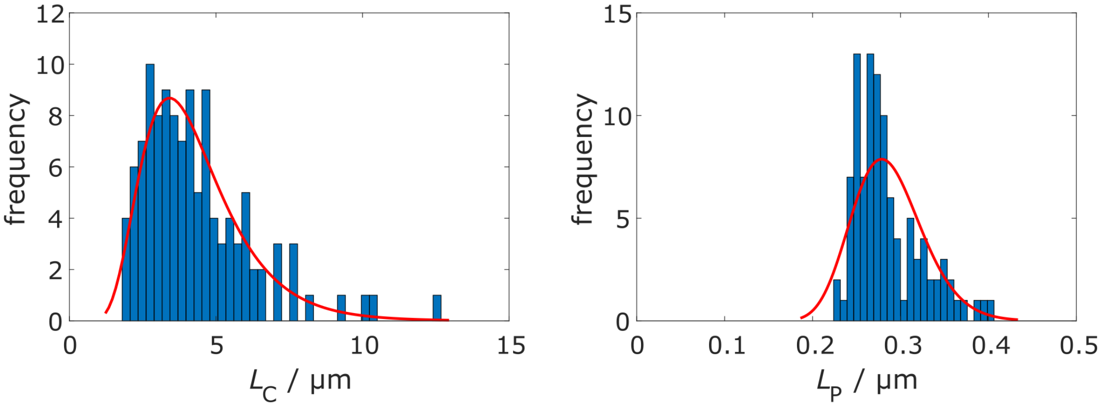

Fig. 4.12: Persistence and contour lengths of membrane-bound vimentin intermediate filaments plotted as histograms. On average, a contour length of $L_C = 4.3 \pm 1.9$ µm ($N = 116$, *left*)and an apparent persistence length of $L_P = 0.3 \pm 0.04$ µm ($N = 91$, *right*) were determined. Both showed a right-skewed distributions.

According to the three categories (cf. Fig. 4.13 A, *right*), the VIFs were segmented as described in chapter 3.5.5. The number of determined segments either in the unstrained or strained state were plotted against the angle, which was defined between the orientation of the segment and the y-axis (stretching direction) (cf. Fig. 4.13 B). The segments in the unstretched state were not uniformly distributed as expected, showing slightly more segments in the stretching direction, which is probably a result of the directed flushing of the filaments onto the membrane surface. When they were stretched, they were further shifted towards the direction of stretching.

Since the number of the determined segments is independent of the length of the individual segment and no information is provided about stretching, or compression, the overall average length of the sum of the segments pointing in the same direction was plotted (cf. Fig. 4.13 C). In the unstrained state, a homogeneous length distribution around 200 nm was found. Upon uniaxial stretching, all segments aligned in an angle larger than AZS = 35° show slight compression or no change, while all VIF segments were oriented at an angle less than the AZS experience stretching, which is reflected in the increased segment length.

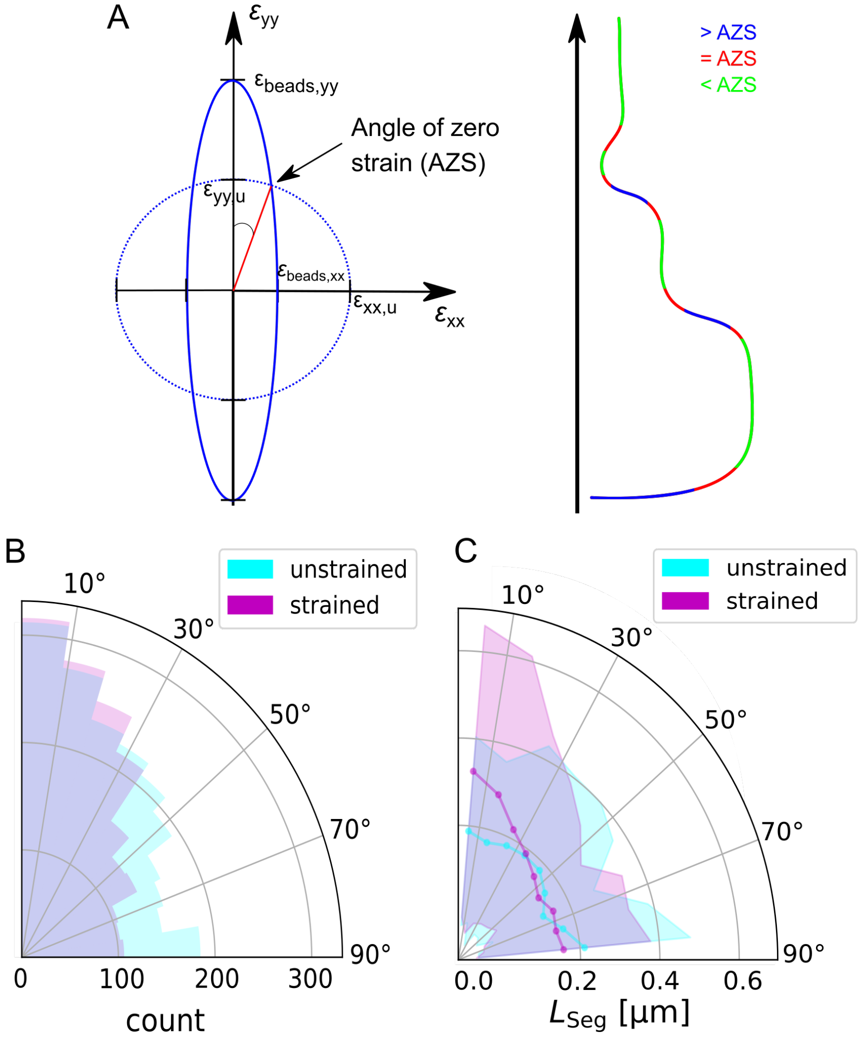

Fig. 4.13: Analysis of the reorientation of membrane-bound vimentin intermediate filaments (VIFs) upon stretching. (**A**) Schematic drawing showing a section of a polydimethylsiloxane (PDMS) sheet, represented as a circle that evolves into an ellipse by uniaxial stretching (*left*). The angle of zero strain (AZS) is defined between the y-axis and the vector pointing at the intersection of the circle and ellipse. Schematic drawing of a filament (*right*) showing the three cases: angles between 0 and AZS (blue), the AZS ± 1 (red), and angles larger than the AZS (green). (**B**) Polar diagram of filament segments as a function of the orientation of VIFs on PDMS-supported membranes ($N = 86$). In the strained state (magenta), more segments are shifted towards the stretching direction than in the unstrained state (cyan). The reduced number of segments is caused by straightening. (**C**) Polar diagram showing the distribution of the segments lengths (L_{Seg}) of the unstrained (cyan) and strained VIFs (magenta) as a function of angle ($N = 86$), showing elongation for angles lower than AZS = 35° and no elongation for angles higher than AZS.

4.4 Membrane-bound Vimentin Intermediate Filament Networks under Strain

4.4.1 Structure of Membrane-bound VIF Networks

In the cellular systems, there are no single vimentin intermediate filaments (VIFs) but rather networks of VIFs. Thus, the question arose about how the VIF network organizes on a membrane. Fluorescently labeled VIF networks anchored *via* neutravidin to the lipid bilayers attached to PDMS were prepared and analyzed with CLSM and atomic force microscopy (AFM).

A confocal fluorescence micrograph of a VIF network is depicted in Fig. 4.14 A, which shows a heterogeneous structure composed of different architectures of VIFs on the membrane. Dependent on the structure and the fluorescence intensity, following architectures were defined: aggregates (cf. Fig. 4.14 A, green box), bundles (cf. Fig. 4.14 A, cyan box), networks (cf. Fig. 4.14 A, magenta box), and single filaments (cf. Fig. 4.14 A, purple box). Bright accumulated or clustered filaments were defined as aggregates, while brighter structures that appeared as filaments were assigned to bundled filaments. Less bright entangled filaments were classified as network structures. In less bright and less dense regions, filaments were identifiable that were not entangled.

To resolve the VIF network structures on the membrane surface in more detail, atomic force micrographs were taken. As PDMS is an elastic material, which is prone to vibrations, the PDMS chamber was placed on a glycerol bed to reduce external vibrations (cf. Fig. 3.5, chapter 3.1.2). AFM micrographs (cf. Fig. 4.14 B) clearly resolved the filamentous structures in the VIF network. The pixel-wise height distribution was obtained from topographic images (cf. Fig. 4.14 C) by applying the tube filter algorithm and thresholding to remove background and subsequently extracting the filament heights pixel by pixel (cf. Fig. 3.23, chapter 3.5.6). This showed a height distribution maximum height of 10 nm, which agrees with the expected height of single filaments (8-12 nm).[48,85]

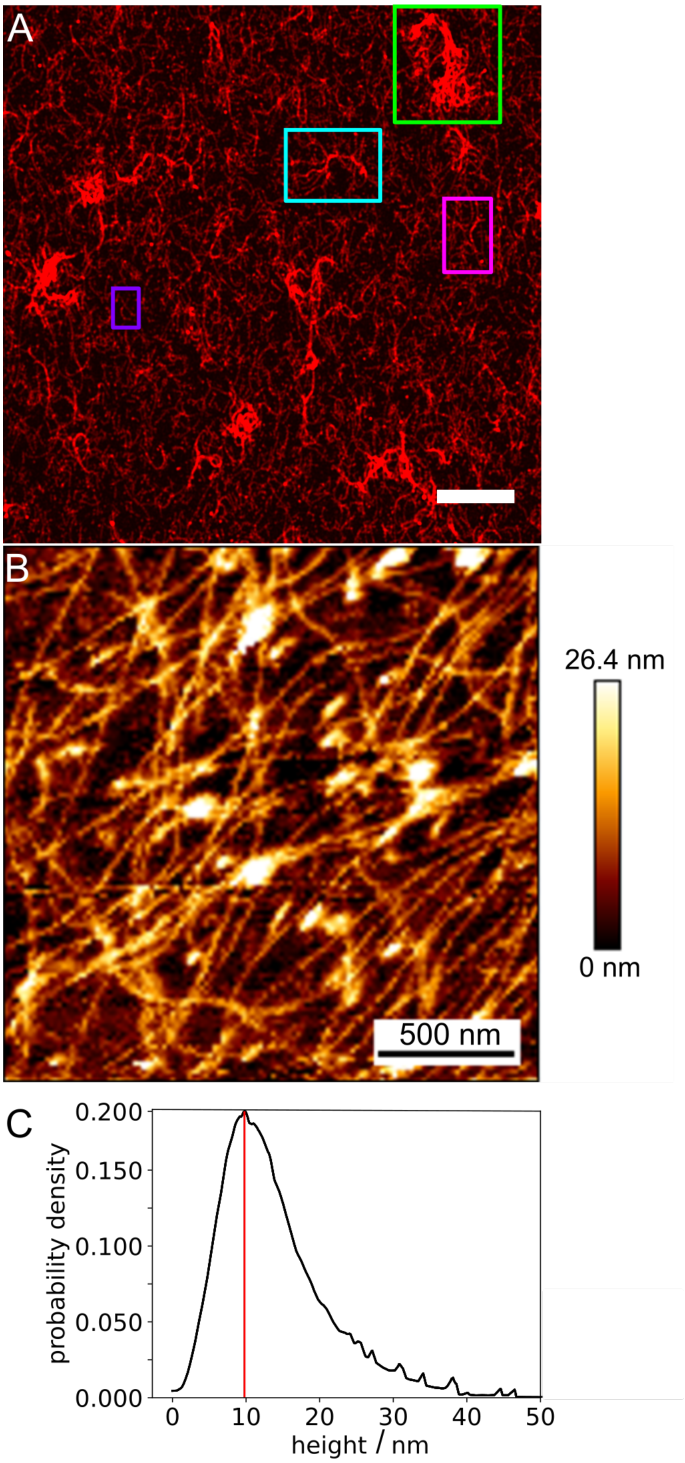
A
B
26.4 nm
0 nm
500 nm
C
probability density
0.200
0.150
0.100
0.050
0.000
0
10
20
30
40
50
height / nm

Fig. 4.14: Structure of membrane-bound vimentin intermediate filament (VIF) networks. Lipid composition: POPC:biotinyl cap-DOPE:ATTO488 (96:3:1, *n*/*n*). Biotinylated VIFs (10 wt% ATTO647N, 5 wt% biotin) were attached to the lipid bilayer *via* neutravidin. (**A**) Confocal fluorescence micrograph of a membrane-bound VIF network. Different morphologies were found within a VIF network. Aggregated filament structures (green), bundled filaments (cyan), network structures (magenta), and single filaments (purple); scale bar: 10 µm. (**B**) Atomic force micrograph of membrane-bound VIF networks showing resolved filamentous structures; scale bar: 500 nm. (**C**) The pixel-wise distribution of the filaments within the networks. A filament height with maximum probability density was determined as 10 nm (red line) ($N = 19$).

4.4.2 Orientational Changes of Membrane-bound VIF Networks under Strain

Stretching experiments of membrane-bound VIF networks on PDMS under strain to study the orientational changes were carried out by* JULIANE HAIPETER *as part of her Bachelor thesis.

Membrane-bound VIFs have been characterized in terms of their orientation during stretching. Therefore, the orientation properties of membrane-bound VIF networks and their differences compared to individual membrane-bound VIFs were carefully studied. By means of CLSM, membrane-bound VIF network in the unstrained (Fig. 4.15 A) and strained state (Fig. 4.15 B) were visualized, with the orientation being colored according to HUE color-coding by making use of a *ImageJ* plugin *OrientationJ*. According to HUE color-coding, different colors are assigned to certain angles, like red corresponds to 0°.

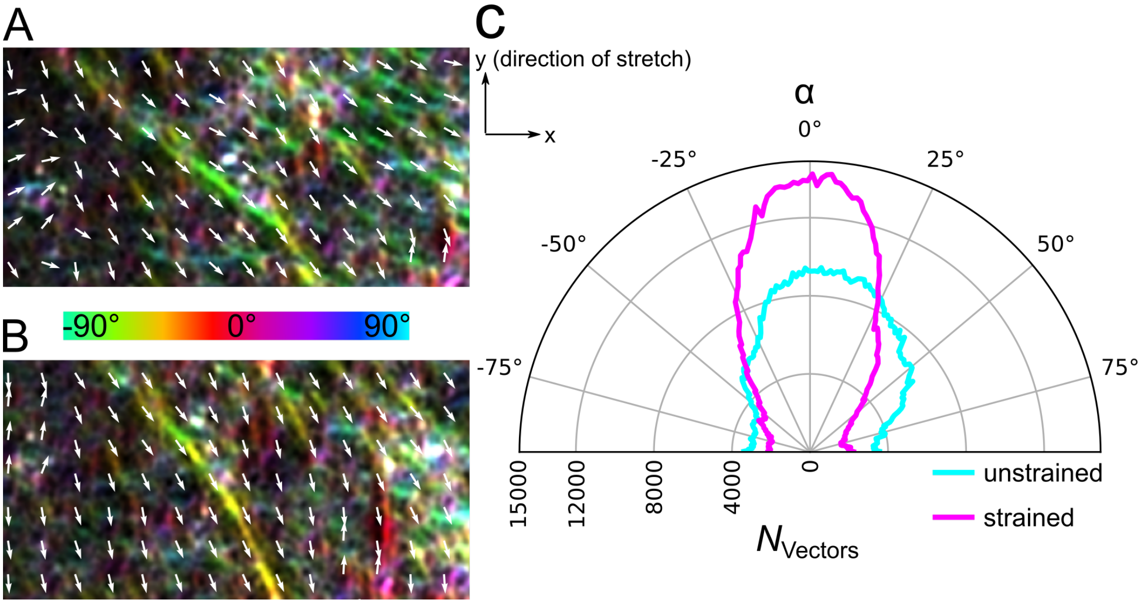

Fig. 4.15: Orientation analysis of membrane-bound vimentin intermediate filament (VIF) networks under strain. Lipid composition: POPC:biotinyl cap-DOPE:ATTO488 (96:3:1, n/n). Biotinylated VIFs (10 wt% ATTO647N, 5 wt% biotin) were attached to the lipid bilayer *via* neutravidin. **(A)** Local orientation of the network encoded in color together with the vector field in the unstretched state ($\epsilon_{\text{beads}} = 0\%$). **(B)** Local orientation of the network encoded in color together with the vector field in the stretched state ($\epsilon_{\text{beads}} = 9.6\%$). **(C)** Distribution of the vector orientations of an unstretched and stretched membrane-bound VIF network ($N = 50$). Upon stretching more vectors are counted toward the stretching direction.

As Fig. 4.15 A/B overlaid with the respective vector fields depicts, in the unstretched state ($\epsilon_{\text{beads}} = 0\%$), the VIFs within the network are mostly oriented in 90° (greenish), changing to an angle range towards 0° (yellowish) upon uniaxial stretching. This result clearly demonstrates that the entire network is aligned toward the stretching direction. This finding is supported by the angle analysis (cf. Fig. 4.15 C) generated by the vector fields considering several pixels (cf. Fig. 4.15 A/B) by using a *ImageJ* plugin *OrientationJ*. In comparison, upon uniaxial stretching, an increased number of vectors are counted in the stretching direction and a decreased number of vectors orthogonal to the direction of stretching. The angle of zero strain (AZS) was found as 25° (-33°) and by determining the intersection between the orientation distribution of unstrained and strained membrane-bound VIF networks.

4.5 Influence of Vimentin Intermediate Filaments and Networks on Lipid Bilayer

As described in chapter 4.2.2, lipid bilayers on hydrophilic PDMS can be expanded with a stretching speed of 20 µm · s^{-1} up to 35 % laterallongitudinal strain when additional lipid material is present. But VIFs, VIF networks, or even only a higher stretching speed might change their integrity. Thus, the behavior of supported lipid bilayer at a stretching speed (750 µm · s^{-1}) and with attached VIFs and VIF networks at the same stretching speed were studied (cf. Fig.4.16)

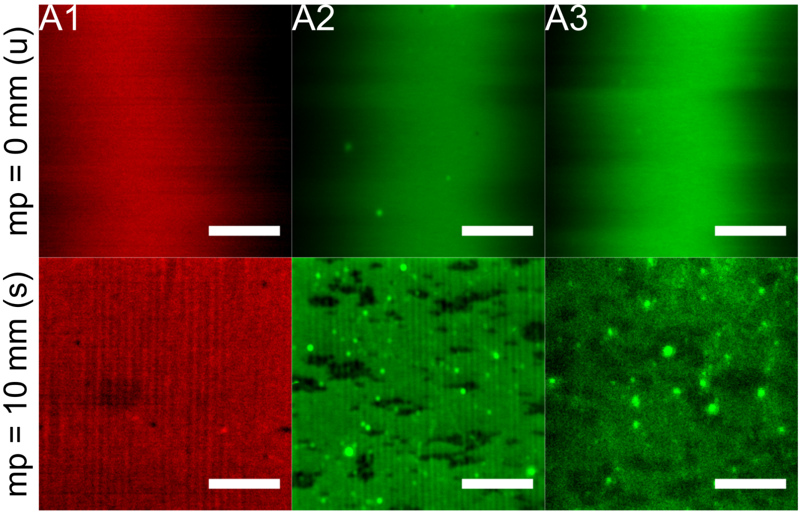

Fig. 4.16: (**A**) Exemplary confocal fluorescence micrographs of unstrained (mp = 0 mm) and strained (motor position: mp = 10 mm) supported lipid bilayers (**A1**), with attached vimentin intermediate filaments (VIFs) (**A2**), and with bound VIF networks (**A3**), at high strain rate (750 µm · s^{-1}). Lipid composition POPC:biotin cap DOPE:ATTO647 (96:3:1, *n*/*n*) in case of (**A1**) and POPC:biotin cap DOPE:ATTO488 (96:3:1, *n*/*n*) in case of (**A2**) and (**A3**), scale bars: 5 µm. In the unstretched state (mp = 0 mm), the fluorescence is homogeneously distributed, however the polydimethylsiloxane sheet is wavy, resulting in a limited focal plane. Upon stretching up to 10 mm, several defects were formed, that showed no fluorescence. That are even more for lipid bilayers attached to VIFs and VIF networks.

All lipid bilayers formed on PDMS showed a homogeneous distribution of the fluorescence intensity in the unstrained state at mp = 0 mm (cf. Fig. 4.16 A1-A3, *top*). When a lipid bilayer (cf. Fig. 4.16 A1) was stretched with a high stretching speed up to mp = 10 mm ($\epsilon_{\text{beads}} = 9.6$ %), it could be observed that a few small defects were formed. However, if VIFs or VIF networks were attached to the lipid bilayers (cf. Fig. 4.16 A2/A3), the number and size of the defects were significantly increased. The defects within the lipid bilayers appear darker with no fluorescence. Compared to the circular defect shape in lipid bilayers without attachment of VIFs or VIF networks, the shape of the defects in VIF-bound lipid bilayers appears elliptic.

Due to the increased number of defects in the case of lipid bilayers attached to VIFs or VIF networks, one could assume the SUVs did not serve as lipid reservoirs at all. However, proof for SUVs being fused with the planar lipid bilayer was given by relaxation experiments. They were performed instead of conducting FRAP of the SUV fluorescence as described in chapter 4.2.2. This method was chosen because the use of three different fluorophores limited the choices for labeling the SUVs with a suitable fluorophore that would exclude cross-talk with the other dyes; ATTO647-labeled DOPE, as used in chapter 4.2.2, could not be implemented because VIFs are doped with ATTO647N, and ATTO405 is not suitable for FRAP experiments due to high affinity to bleaching. Thus, relaxation experiments were the method of choice in this case. After stretching up to mp = 10 mm, the strain was relieved by compressing the strained PDMS chamber back to mp = 0 mm. While reducing the membrane area, protrusions are pushed out of the lipid bilayer with them being adhered to the lipid bilayer or floating around in the aqueous solution (cf. Fig. 4.17).

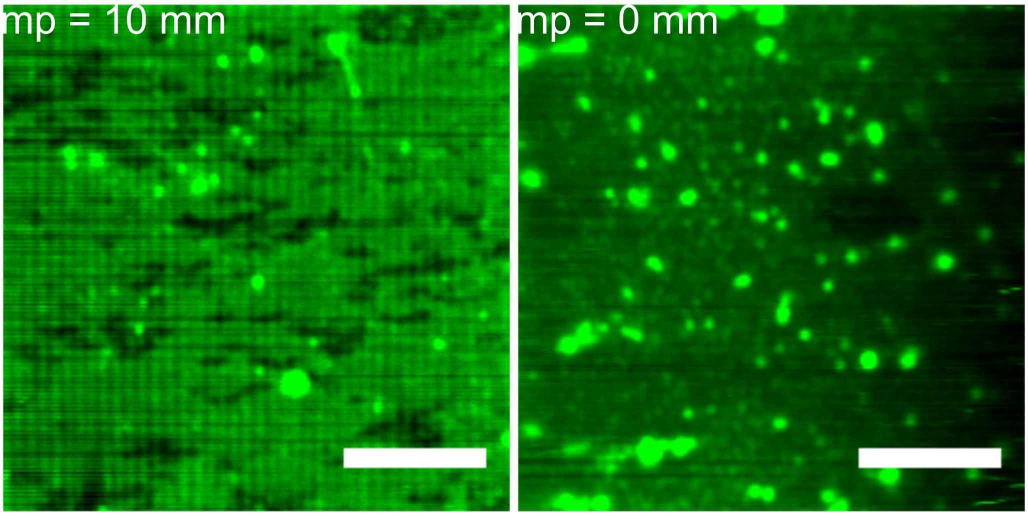

Fig. 4.17: Relaxation of strained supported lipid bilayer (POPC:biotin cap DOPE:ATTO488-DOPE, 96:3:1, *n*/*n*) with vimentin filaments from mp = 10 mm (*left*) to mp = 0 mm (*right*), scale bars: 5 µm. Dark spots (*left*) are defects in the lipid bilayer that close upon relaxation and protrusions of lipid material are expelled out that can be seen as bright spots (*right*).

The information, whether the lipid bilayer is continuous or not, was provided by FRAP experiments. The determined diffusion coefficients and mobile fractions for the individual systems are graphically shown in Fig. 4.18, and the mean values with standard deviation are listed in Tab. 4.2. Independent of the different systems, both the diffusion constant and the mobile fraction in the unstretched (u) state are higher than in the stretched (s) state, which was also mentioned before in chapter 4.2.2. The increased diffusion coefficient for pure lipid bilayer stretched at a higher strain velocity might be explainable by low statistics ($N = 3$).

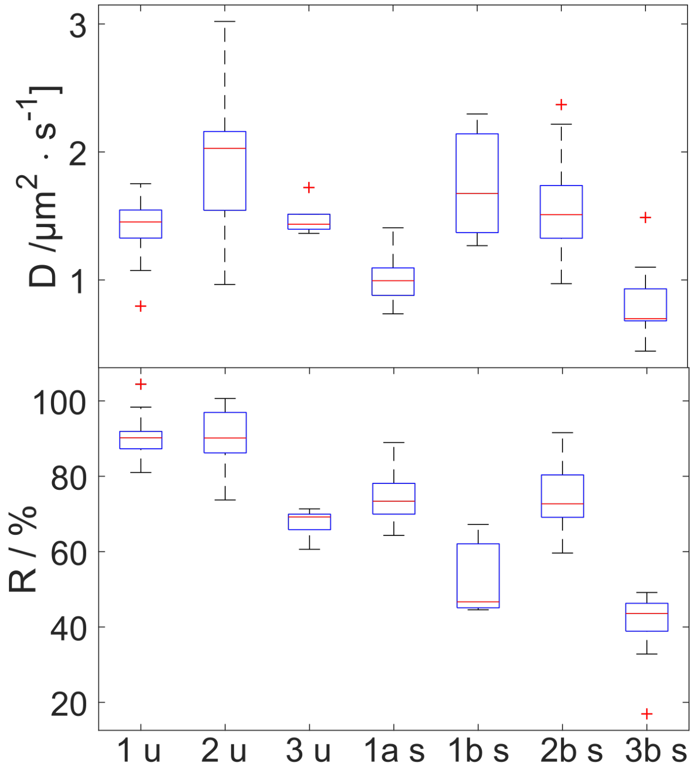

1: lipid bilayer; **2**: lipid bilayer with VIFs,
3: lipid bilayer with VIF networks
a: low speed, **b**: high speed
u: unstretched, **s**: stretched

Fig. 4.18: The diffusion coefficient and mobile fraction determined by performing fluorescence recovery after photobleaching experiments. They were plotted as a boxplot. The central line (red) on each box represents the median, while the bottom and top edges of the box indicate the 25th and 75th percentiles, respectively. The whiskers are the data points that are not considered outliers marked with '+'. The systems that were studied were the lipid bilayer at low and high stretching speed (ls, hs), and lipid bilayers attached to vimentin intermediate filaments (VIFs) and VIF networks. A decrease in both the diffusion coefficient and mobile fraction was observed when the system was stretched. Lipid bilayers with VIFs showed higher values, while those with VIF networks showed lower values compared to pure lipid bilayers.

In the unstretched state (u), the PDMS-bound lipid bilayer showed a mean diffusion coefficient of $D = 1.4 \pm 0.2$ µm^2· s^{-1}, while the diffusion coefficient of the supported lipid bilayer with bound VIFs was higher ($D = 1.9 \pm 0.5$ µm^2· s^{-1}) and with attached VIF networks it exhibited no significant change ($D = 1.5 \pm 0.1$ µm^2· s^{-1}). The mobile fraction was decreased for lipid bilayers with VIF networks, and no significant change was found for lipid bilayers with VIFs. In comparison, in the stretched state (s), the lipid bilayer at low stretching speed (ls) diffused with $D = 1.0 \pm 0.2$ µm^2· s^{-1}. The mobility of lipid bilayer at high stretching speed (hs) and with attached VIFs was increased, showing the mobility of $D = 1.7 \pm 0.5\,\mu\mathrm{m}^2\cdot\mathrm{s}^{-1}$ and $D = 1.5 \pm 0.3\,\mu\mathrm{m}^2\cdot\mathrm{s}^{-1}$, respectively, while for bilayers with VIF networks, a diffusion coefficient $D = 0.8 \pm 0.3\,\mu\mathrm{m}^2\cdot\mathrm{s}^{-1}$ was found. The mobile fraction followed the same trend as in the unstretched state. While lipid bilayers were stretched with a high stretching speed, they showed a significantly lower mobile fraction than those stretched at the lower speed. The found values showed that the mobility of the lipid bilayer is dependent on the applied stretching speed and the degree of attachment of VIFs.

Tab. 4.2: Mean diffusion coefficients and mobile fractions determined by FRAP experiments. The systems that were studied were the lipid bilayer at low and high stretching speed (ls, hs) and lipid bilayers attached to VIFs and VIF networks. A decrease in the diffusion coefficient and mobile fraction was observed when the system was stretched. Lipid bilayers with VIFs showed higher values, while those with VIF networks showed lower values compared to pure lipid bilayers.

	N	$D\,/\,\mu\mathrm{m}^2\cdot\mathrm{s}^{-1}$	$R\,/\,\%$
Lipid bilayer (1 u)	15	1.4± 0.2	91 ± 6
Lipid bilayer with VIFs (2 u)	37	1.9± 0.5	90 ± 8
Lipid bilayer with VIF networks (3 u)	5	1.5± 0.1	68 ± 4
Lipid bilayer ls (1a s)	15	1.0± 0.2	74 ± 7
Lipid bilayer hs (1b s)	3	1.7± 0.5	53 ± 13
Lipid bilayer with VIFs (2b s)	33	1.5± 0.3	74 ± 8
Lipid bilayer with VIF networks (3b s)	5	0.8± 0.3	41 ± 10

5 Discussion

Several findings in the literature suggest a layer-like arrangement of intermediate filaments (IF) parallel to and in proximity to the plasma membrane. For example, the very first *de novo* keratin IF structures that develop in mouse blastocysts during early embryogenesis are located near desmosomes[163] forming a layer close to the membrane rather than spanning the whole cytoplasm. SCHWARZ *et al.* hypothesized that this "IF-cortex" forming a rim of filaments interconnecting the desmosomes in a circumferential network is part of a rim-and-spoke arrangement of IFs in epithelia.[39] They attribute a functional role to the subplasmalemmal rim of IFs to any cell in which plasma membrane support is required, provided these filaments connect directly or indirectly to the plasma membrane. This hypothesis implies that IFs do not only act as mechanical regulators in the cytoplasm but also function directly at the plasma membrane.[39] To investigate the impact of a lipid bilayer on the stretching behavior of IF, namely vimentin, an *in vitro* membrane system with attached vimentin filaments was established that could be laterally stretched (cf. Fig. 4.1, chapter 4) and imaged by confocal laser scanning microscopy (CLSM) and atomic force microscopy (AFM). This system allowed the uniaxial stretching of vimentin intermediate filaments (VIFs) directly attached to the bilayer *via* biotin-neutravidin linkages to address the questions of how stretching alters single membrane-bound VIFs and how an entire network of VIFs attached to the bilayer ("VIF-cortex") is altered upon fast, uniaxial stretching.

5.1 Anisotropic Stretching

To investigate the mechanical response of membrane-bound VIF networks to external uniaxial strain, the artificial model system was prepared on polydimethylsiloxane (PDMS), which was then stretched uniaxially. In cells, the applied mechanical stress during cellular processes (*e.g.*, cell migration or mitosis) is mostly anisotropic rather than isotropic[164], which is simulated by the uniaxial stretch of the PDMS. The obtained displacement field (cf. Fig. 4.2 B, chapter 4.1) is characteristic for a uniaxial stretcher with stretching in y-direction, *i.e.*, in the direction parallel to the pulling direction, and compression in x-direction due to the POISSON's ratio.[164–166] An average longitudinal strain ($\epsilon_{\text{beads},yy}$) of 35 ± 10 % (4 µm sized beads) was determined by beads tracking (cf. Fig. 4.2 C, chapter 4.1) and approximately 44 % (100 nm sized beads) was obtained by Digital Image Correlation (DIC, cf. Fig. 4.4, chapter 4.1), respectively. By using a uniaxial stretching device with a rectangular PDMS sample of 30 mm in length and 20 mm in width, AYIDIN *et al.* tracked the embedded fluorescent beads (5 µm in size) by means of single-particle tracking. They found a strain of 48 %. The higher strain found by AYIDIN is, on the one hand, explainable by the design of the PDMS chamber. In this work, the PDMS chamber consisted of a rectangular sheet (20 mm x 20 mm) that was supported by a thicker frame (cf. Fig. 3.10, chapter 3.2.1). Thus, the thicker frame would absorb some strain before it reaches the PDMS sheet, implying higher strain could be measured when only the sheet was stretched. On the other hand, applying different strain definitions lead to deviations. AYIDIN *et al.* applied the GREEN-SAINT-VENANT definition (ϵ_{GSV}, cf. Eq. 5.1)[165]:

$$\epsilon_{\text{GSV}} = \frac{1}{2}\left[\left(\frac{L}{L_0}\right)^2 - 1\right] \tag{5.1}$$

with L_0 and L being the initial and stretched lengths, respectively.

Thus, the magnitude of the longitudinal strain (ϵ_{yy}) increases slightly in a non-linear manner due to the quadratic term.[165] This results in a higher strain than found in this work using the simple strain definition, the so-called CAUCHY strain definition (cf. Eq. 3.16, chapter 3.5.1). Inserting exemplary random lengths ($L = 1.35\ \mu$m, $L_0 = 1.00\ \mu$m) in the CAUCHY strain definition and Eq. 5.1 give 35 % and 40 %, respectively. This shows that inserting the same parameters into the two equations above results in different values, but only with a small deviation (5 %). Considering the experimental data, the deviation is in the range of the errors (±10 %).

Since strain is a immeasurable physical parameter, it can be defined in a variety of ways. STARKOVA *et al.* have dealt with different strain definitions. In addition to the already mentioned strain definitions, they reported definitions by ALMANSI (ϵ_A) and SWAINGER (ϵ_S) (cf. Eq. 5.2 and Eq. 5.3).[167]

$$\epsilon_\mathrm{A} = \frac{1}{2}\left[1-\left(\frac{L}{L_0}\right)^{-2}\right] \tag{5.2}$$

$$\epsilon_\mathrm{S} = 1-\left(\frac{L}{L_0}\right)^{-1} \tag{5.3}$$

Independent of the used strain definition, the strains are the same for very small deformations ($\frac{L}{L_0} \rightarrow 1$). Only for large deformations, the different strain definition deviate (cf. Fig. 5.1). When dealing with small to moderate deformations, it is reasonable to make use of the CAUCHY definition, while for large deformations GREEN-SAINT-VENANT and ALAMANSI are better suited.

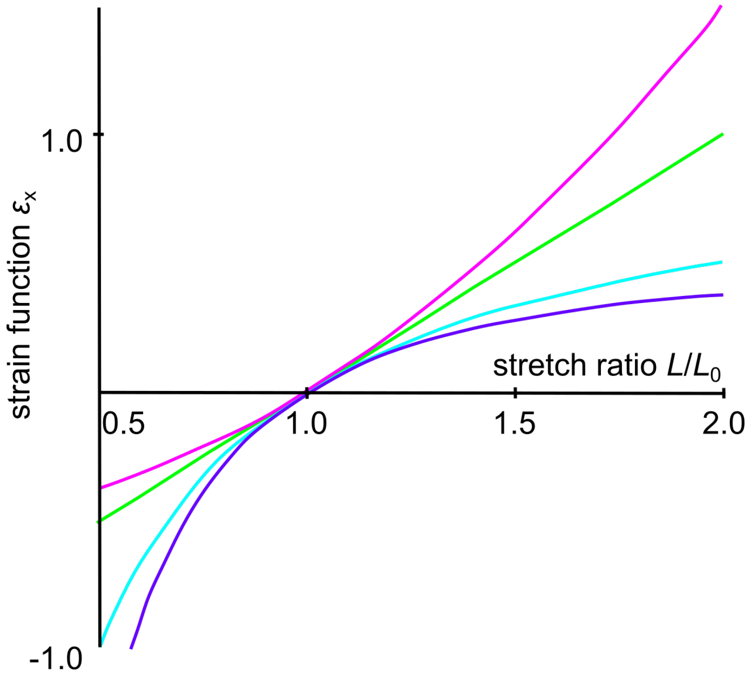

Fig. 5.1: Different strain definitions. The different strain functions (ϵ_x; x = CAUCHY, GSV, A, S, cf. Eq 3.16, Eq. 5.1-Eq. 5.3) are plotted against the strain ratio $\frac{L}{L_0}$. Depending on the strain definition, different curves are obtained. CAUCHY definition is shown in green, GREEN-SAINT-VENANT definition in magenta, ALMANSI definition in purple, and SWAINGER defintion is highlighted in cyan. For very small deformation, all definitions give the same strains, however for large deformations, they deviate from each other to a certain extent. Adapted from STARKOVA *et al.*[167]

Several groups have reported that the strain across the PDMS sample is uniformly distributed[164–166,168]. This contradicts the heterogeneity in the local strain distribution found in this work by DIC (cf. Fig. 4.4, chapter 4.1), which is due to the non-uniform polymerization of the PDMS. However, it could also be due to different scales considered. A smaller scale, *i.e.*, a higher resolution, could show the heterogeneity as found in this work. In contrast, larger scales cannot resolve smaller structures leading to homogeneous strain distributions noted in the literature, which would also show heterogeneous distributions when smaller scales are considered.

Summary: In the scope of this work, the uniaxial stretching of PDMS by tracking beads was characterized. A longitudinal strain of 35 % was achievable by applying a motor strain of 50 % (mp = 10 mm). The here obtained strain by CAUCHY strain definition varied from the strains obtained by using, for example, the GREEN-SAINT-VENANT, which is supposed to be well-suited for uniaxial stretch.[165] Considering small deformations, nonetheless, it is independent of the choice of the strain definition.[167] Since no large deformation was applicable in this case, there would be only small deviations. Thus it was reasonable to use the CAUCHY definition.

5.2 Lipid Bilayers under Strain

5.2.1 Diffusive Reorganization of Lipids in the Lipid Bilayer

The PDMS support allows the stretching of the artificial "VIF-cortex". Several requirements, however, need to be met. According to the results reported by STAYKOVA *et al.*[161], the lipid bilayer needs to stick to the PDMS surface, *i.e.*, it must not fully slide on the surface, to transfer the strain into the membrane. The membrane stickiness is controlled by the hydrophilization protocol using oxygen plasma (cf. Tab. 4.1, chapter 4.2.1), providing a heterogeneous density of hydroxyl groups which results in a tightly bound, thin, and highly structured water layer between the oxide layer of the PDMS surface and the lipid bilayer. This water layer hampers the movement of lipids across the substrate on a small scale.[161,169]. Thus, stretching results in defect formation because the membrane follows the areal changes of the PDMS substrate.

Another important aspect that needs consideration is unwanted crack formation. It was also reported in several previous studies.[170–172] MAYER *et al.* reported in their study that a modification of the PDMS surface using plasma exposure usually creates cracks as a side-effect, thus proposing another method toward crack-free PDMS.[171] By contrast, in this work, it was found that crack formation can be simply regulated by variation of the plasma exposure. (cf. Tab. 4.1, chapter 4.2.1, 0.2 mbar and 0.3 mbar). The cracks appear orthogonal to the stretching direction when the oxide layer is too thick, therefore, making it brittle and fragile, which is increased with increasing plasma treatment time. Increasing the plasma pressure results in quenching of the plasma leading to a thin elastic oxide layer that does not form cracks upon stretching. This is a wanted phenomenon since cracks in the oxide layer would manipulate the strain transfer to the bilayer.

The high roughness of the PDMS compared to glass and silicon substrates yields irregular nano-structuring, which cannot be resolved by fluorescence microscopy. The nano-structuring is enhanced by plasma treatment of the surface. An increase in surface roughness reduces the mobility of a lipid bilayer, as the mobility is slowed down in regions with high curvature.[169,173,174] This induces stickiness between the PDMS surface and lipid bilayer, which would also be reflected in a reduced diffusion coefficient. Hence, the found diffusion coefficient of the ATTO647-DOPE lipids as $1.4 \pm 0.2\ \mu m^2 \cdot s^{-1}$ (cf. Fig. 4.6, chapter 4.2.2) is decreased compared to diffusion coefficients found for supported bilayers on glass and silicon substrates, which range between 2.0-5.5 $\mu m^2 \cdot s^{-1}$, using different experimental techniques (*e.g.*, pulsed-field gradient nuclear magnetic resonance spectroscopy, fluorescence correlation spectroscopy).[169,175–177] In living cells (HeLa cells), a molecular diffusion coefficient for lipids in the plasma membrane is typically more than one order faster than 0.024 ± 0.005 $\mu m^2 \cdot s^{-1}$ [178,179], which means the molecular diffusion coefficient is at least 0.24 $\mu m^2 \cdot s^{-1}$. This broad range is due to the complexity of the plasma membrane involving not only lipids but also slower transmembrane proteins and anchor proteins connecting to the cytoskeleton. Thus, the molecular diffusion in the plasma membrane depends on its composition. The diffusion coefficients found in this work are in the range of more than an order of magnitude higher than 0.024 ± 0.005 $\mu m^2 \cdot s^{-1}$ [179,180], which shows that the diffusion of solid supported lipids in artificial lipid bilayers is in good agreement with cellular diffusion. Upon PDMS stretching, the strain is transferred to the bilayer indicated by a further reduced diffusion coefficient of 1.0 ± 0.2 $\mu m^2 \cdot s^{-1}$ of ATTO647-DOPE (cf. Fig. 4.6, chapter 4.2.2). Not only the strain in the lipid bilayer reduces the mobility of the lipids, but also the stretch-induced formation of further nanoscopic defects and enlargement of the already existing defects are responsible for the reduced mobility.[174,181] This assumption is supported by the observation that the mobile fraction of ATTO647-DOPE is reduced after stretching.

The stretched bilayer at a stretching speed of $v = 750\ \mu m \cdot s^{-1}$ showed an increased mobility with a diffusion coefficient of $D = 1.7 \pm 0.5\ \mu m^2 \cdot s^{-1}$ (cf. Tab. 4.2, chapter 4.5). It has been reported in the literature that the defect formation of a bilayer is a process that is time-dependent. Thus, it was predicted that high stretching speeds retard the rupture process, which results in higher rupture tensions.[182,183] Even though it was stated that the critical areal strain that is required to rupture the bilayers only increases at higher ranges of the stretching speed ($v > 1\ m \cdot s^{-1}$)[183], the results found by an increase from $v = 20\ \mu m \cdot s^{-1}$ to $v = 750\ \mu m \cdot s^{-1}$ show the contrary. Implying a factor of ~38, even for low stretching speeds, significantly affects mobility by reducing nanoscopic defects due to retarded defect formation. However, the diffusion coefficients in the stretched situation are higher than in the unstretched state, the reason of which might be the sudden application of strain with a high velocity. Hence, the lipids could reorganize with a faster diffusion rate in such a manner that the viscous drag force counteracts to equilibrate the applied force.[178] Since the small sample size ($N = 3$) (cf. Tab. 4.2 in chapter 4.5) was low, the aforementioned reasons are speculations.

5.2.2 Excess of Membrane Area

In literature, it has been reported that lipid bilayers cannot be stretched beyond 4-6 % without rupturing.[159,160,162] Thus, an additional lipid reservoir had to be provided, which was achieved by adding SUVs to the aqueous solution.[162]. The fluorescence images and fluorescence recovery experiments (cf. Fig. 4.7, chapter 4.2.2) clearly revealed that the SUVs integrate into the PDMS-supported bilayer upon stretching, hence, significantly reducing the number of defects in the membrane. According to the results of STAYKOVA *et al.*, vesicles that adhere to a PDMS-supported membrane burst when a critical rupture strain is reached, and thus, the vesicles fuse with the lipid bilayer.[162] The exact fusion mechanism is not known however, based on the observations, several possible mechanisms can be proposed (cf. Fig. 5.2): (1) fusion, (2) integration of lipids in the upper leaflet, (3/4) adhered vesicles to bilayer or defect, (5) aggregated lipid material in the defects, and (6) non-filled defects. For all of the mentioned mechanisms to happen, the applied strain must exceed the critical rupture strain of the bilayer ($\epsilon_{\text{bilayer, rupture}}$). If the critical vesicle rupture strain ($\epsilon_{\text{vesicle, rupture}}$) is reached, it is conceivable that the SUV lipids are probably preferentially found in the upper leaflet of the bilayer (2) because of the larger diffusion constants of ATTO488-DOPE ($D = 2.2 \pm 0.7\ \mu\text{m}^2 \cdot \text{s}^{-1}$, cf. Fig. 4.7 in chapter 4.2.2) compared to ATTO647-DOPE diffusion of the spread bilayer on PDMS in the stretched state ($D = 1.0 \pm 0.2\ \mu\text{m}^2 \cdot \text{s}^{-1}$). An integration of lipid material in the lower leaflet (1) would have reduced the mobility due to stronger interactions between the head groups of the lipid and the surface. Thus, mechanism (1) could be possible, but in comparison to mechanism (2), a less likely process based on the found diffusion coefficient. Another mechanism is that vesicles could adhere or remain adhered to the lipid bilayer (3) if the rupture strain for vesicle bursting is not reached. Furthermore, if the surface adhesion energy ($E_{\text{ad.}}$) is insufficient to induce spontaneous vesicle spreading[169], formed defects are instead filled with lipid material that remains in there (5), and if the defects are of sufficient size, there is a possibility of vesicle adhesion in the formed defects (4). In case no vesicles are in proximity to the lipid bilayer, the formed defect remains unfilled (6).

In addition, it can be speculated based on the observation that the diffusion constant in the stretched state is larger for ATTO488-DOPE ($D = 2.2 \pm 0.7\ \mu\text{m}^2 \cdot \text{s}^{-1}$) than for ATTO647-DOPE ($D = 1.0 \pm 0.2\ \mu\text{m}^2 \cdot \text{s}^{-1}$). Differences might be found in the dye itself, even though it appears to be negligible. Both fluorophores used in this study are hydrophilic and do not interact with the hydrophobic core of the bilayer, which would slow down the mobility.[176,184] The small unilamellar vesicles (SUVs) acting as lipid reservoirs do not contain biotinylated lipids, and hence, they change the overall lipid composition upon integrating into the bilayer. Thus, the found differences cannot be of this nature as the lipid composition is the same after vesicle fusion. Therefore, the larger diffusion coefficient of ATTO488-DOPE cannot be explained by the used different dyes or overall lipid composition, which is the same.

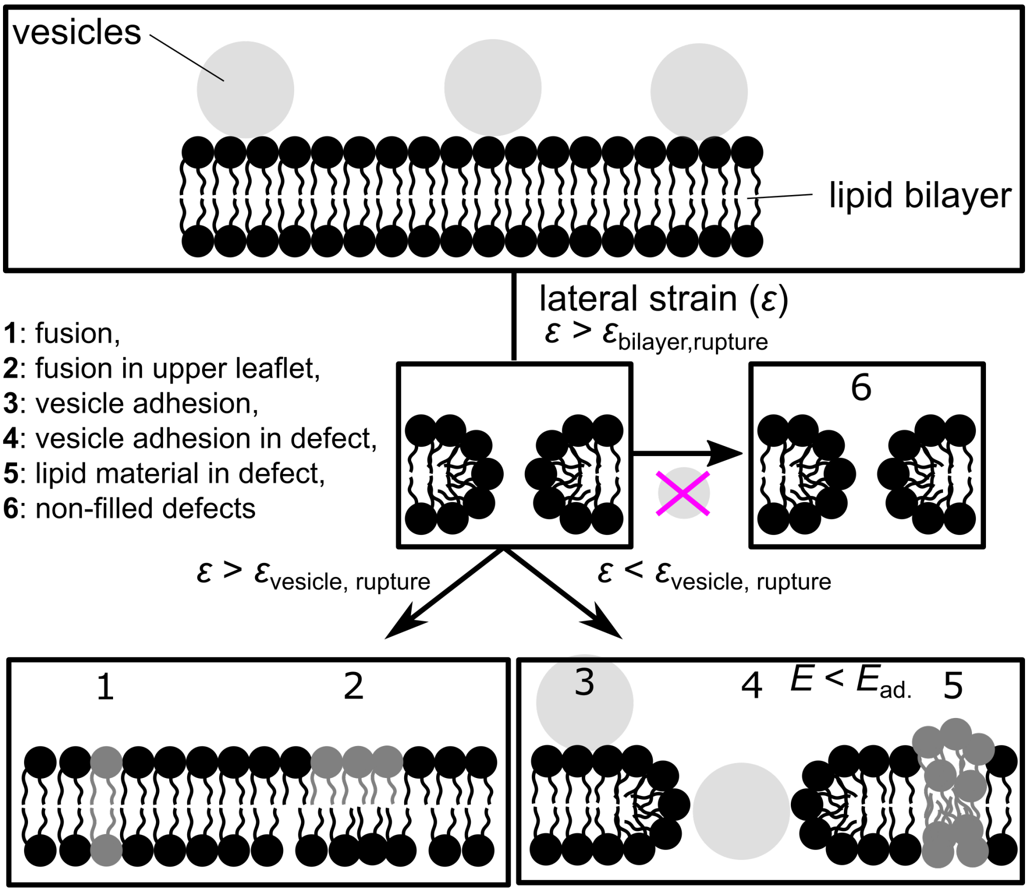
vesicles
lipid bilayer
lateral strain (ε)
ε > ε_bilayer,rupture
1: fusion,
2: fusion in upper leaflet,
3: vesicle adhesion,
4: vesicle adhesion in defect,
5: lipid material in defect,
6: non-filled defects
6
ε > ε_vesicle, rupture
ε < ε_vesicle, rupture
1
2
3
4
E < E_ad.
5

Fig. 5.2: Proposed fusion mechanism. If a lipid bilayer is stretched in the presence of a lipid reservoir (illustrated as a grey circle), lipids can be integrated into the bilayer when the critical rupture strain of a vesicle is reached by fusion (1) or integrating lipids in the upper leaflet (2). If the critical rupture strain is not reached, the vesicles remain adhered to the bilayer (3), or they can also adhere to the defect (4) if a defect of sufficient size is formed. Insufficient surface adhesion energy to induce spreading results in the aggregation of lipid material in the formed defects (5). Defects are formed and are not filled with lipid material if no vesicles are in proximity (6).

Nonetheless, the lipid bilayer beneath the VIF networks ruptures, even in the presence of a lipid reservoir (cf. Fig. 4.16, chapter 4.5). This can be attributed to the lack of excess lipid material because the membrane is shielded by the dense VIF networks. Still, vesicle fusion can occur in areas without or with less dense VIF networks, from where the lipid bilayer is provided with an excess lipid reservoir. Relaxation experiments (cf. Fig. 4.17, chapter 4.5) showed that lipid material is expelled out of the lipid bilayer with area reduction, which clearly shows that lipids were integrated upon stretching. This is in good agreement with the results found by STAYKOVA *et al.* by compression experiments.[162] These fusion processes of vesicles might be similar to exocytosis of cellular vesicles during surface area regulation in expanding cells (*e.g.*, during growth, imposed stretch, or osmotic inflation). Tube-like structures or lipid material formed by releasing the tension could be equivalent to microtubular invaginations of the membrane.[185–188] Both biological processes are active and selective and require membranes that are not coupled to the cytoskeleton.[185,186,189] However, it needs to be taken into account that the above-mentioned processes are complex systems. Thus the observations as found in the work is compared to a simplified version of the biological processes. The diffusion coefficient of the lipids in the bilayer with and without attached VIF networks showed no significant differences. NÖDING *et al.* reported similar results with the addition of minimal actin cortex (MAC) to a POPC bilayer on silicon substrate. The diffusion coefficients with and without MAC were found to be nearly the same.[190] However, upon stretching, the mobility is restricted by the formation of defects and the connection to the VIF networks reacting to the applied strain.

Summary: In the scope of this work, the stretching of lipid bilayers was investigated. A longitudinal strain of 35 % led to defect formation in the bilayer, while in the presence of SUVs serving as a lipid reservoir, stretching became feasible up to 35 % of longitudinal strain, with a minimal impact on membrane integrity. Several mechanisms of integrating lipids into the deforming lipid bilayer were proposed: fusion, adhesion of vesicles, filling of defects with lipid material or vesicles, and non-filled defects. If VIFs were attached, there remained a larger number of defects because the lipid bilayer is shielded by VIFs, hindering the vesicles from reaching the bilayer.

5.3 Vimentin Intermediate Filaments under Strain

5.3.1 Properties and Interactions of the Membrane-bound VIF Networks

The architecture of membrane-bound VIFs in the unstrained situation was investigated by high-resolution techniques (CLSM and AFM, cf. Fig. 4.14, chapter 4.4.1). From the height distribution obtained by AFM measurements (cf. Fig. 4.14 C, chapter 4.4.1), a height distribution maximum of membrane-bound VIFs was determined as 10 nm. This is in good agreement with the diameter of vimentin filaments in cells (8-12 nm).[48,85] Heights lower than 10 nm can be assigned to tetramers. It has been reported that tetramers have a diameter of around 5 nm.[191] The obtained confocal fluorescence micrographs (cf. Fig. 4.14 A, chapter 4.4.1) visualized, besides single filaments, structures like aggregated and bundled filaments, showing higher fluorescence intensities. Several *in vitro* studies have shown that bundling can be induced by electrostatic cross-links, *i.e.*, divalent cations such as Mg^{2+} and Ca^{2+}.[103,108,192] Since in this artificial system no divalent cations are present, bundling is presumably induced *via* specific permanent neutravidin-biotin linkers ($K_A = 10^{-15}$ M^{-1} [193]) and by transient hydrophobic and ionic cross-links.[36,106,192] In particular, the aggregated large structures can be attributed to aggregated filaments and accumulated unit-length filaments (ULFs) that were unable to form matured filaments by longitudinal annealing. ULFs have a different architecture and a 15 nm large diameter.[30,194]

If VIFs are directly adsorbed onto a surface such as glass[194], the height of the filaments is greatly reduced (3-5 nm[195]) as a result of strong, attractive interactions between the support and the filament leading to a significant flattening of the circular cross-section.[195–197] It has been reported that VIFs with their negatively charged head domain can interact with specific, positively charged lipids.[198] If such interactions would lead to flattening remains open to question. However, it can be assumed that there might be no flattening effect by the interaction between membrane and VIFs, as no flattening in cells has been mentioned in the literature, according to the current state of knowledge. The findings in this work support this assumption. Since, in this work, neutral matrix lipids were used, there might be no significant direct interaction between VIFs and the neutrally charged POPC, which would lead to flattening. In addition, interactions between VIFs and the membrane surface are controlled by the biotin-neutravidin linkages. Therefore, they might act as a spacer between the filament and the polar lipids preserving the structure of VIFs. In cells, many anchor molecules or cross-linkers (*e.g.*, plectin and ankyrin) connect VIFs to the plasma membrane, indicating that these linkers could be the reason for maintaining the structural integrity.[198–200]

5.3.2 Mechanical Response of VIF Networks to External Strain

In this work, membrane-bound VIF networks and their response to external mechanical strain were investigated by CLSM. The applied longitudinal strain of around 35 % resulted in the reorientation of the filaments in the networks towards the stretching direction (cf. Fig. 4.15, chapter 4.4.2). This observation of reorientation is consistent with migrating cells and VIFs within such cells reorienting along the migration direction with respect to the cell shape.[201] Migration can be seen as stretching of the front layer of the cell in one direction and compression of the opposite layer in the same direction. In wound closing cells, VIF networks enhance directional cell migration by increasing the persistence of microtubules and serving as a template for their orientation towards the direction of the wound.[202–204] Reorientation of VIF networks also occurs in mitosis, where they interact closely with the other cytoskeletal subsystems, affecting the distribution of vimentin.[199] The alignment of a VIF network along the stretching direction shows that it acts to preserve the cell shape and polarity by counteracting the applied strain. Thus, the structural organization of VIF network plays an essential role in many cell processes. According to BLUNDELL *et al.*, the VIF networks are characterized by mainly reorientation at low strains. At larger strains, contributions of straightened filaments within the networks would lead to a response of the network in the form of mechanical stretching.[205] Even though no information about mechanical stretching of VIF networks could be gathered within this scope of the presented stretching experiments, it can be speculated that, due to losses in transmission of strain from PDMS to VIFs, the here applied moderate strain of 35 % longitudinal strain can be associated to the low strain range, where no mechanical stretching can be observed.

The confocal fluorescence micrographs showed that the networks remain intact upon stretching. These results of stretching VIF networks indicate that VIF networks could support and protect the lipid bilayer under strain by absorbing the strain applied to and sensed by the membrane through reorientation and stretching of the network without rupturing.

5.3.3 Mechanical and Entropic Contributions of Single VIFs to VIF Networks upon Stretching

To disentangle the contributions of single VIFs to the network properties, the membrane-bound VIFs under strain were analyzed. Two behaviors upon uniaxial stretching were observed: (i) reorientation of the filament along the stretch direction, which means entropic stretching by ironing out thermal fluctuations, and (ii) mechanical stretching of the filament leading to elongation of its contour length.[205,206] Both parts contribute to the observed behavior and clearly demonstrate that stretching of the lipid bilayer is transferred to the VIFs *via* biotin-neutravidin linkages. These pinning points are statistically spread across the filament. Assuming 32 vimentin monomers per ULFs and a length of the ULFs of 43 nm[191,206], a biotin-labeled VIF would contain 23 biotinylated monomers per µm (for 5 wt% biotin). A 43 nm repeat in a filament is below the resolution limit, and thus, it is not resolvable with CLSM (cf. Fig 4.9, chapter 4.3.2). Between two pinning points, mechanical and entropic stretching compete with each other in different proportions leading to the broad distribution of the observed vimentin strain ϵ_{VIF} (cf. Fig. 4.8, chapter 4.3.1). This broad distribution is consistent with the results found by BIANCHI *et al.* studying cells adhered to a substrate under strain. The external strain is transferred between individual cell components *in vivo*. The plasma membrane is adhered through "focal adhesions", which deforms because of applied strain and transfers the applied strain through focal adhesions to the cytoskeleton, which transports some of the remaining strain to the nucleus.[166] Since, in this work, the VIFs are coupled to the membrane spread on PDMS, and they are not further connected to another component, VIFs could store a certain part of the transferred strain in case it is needed for relaxation or transmission. Thus, it can be hypothesized that not all of the transferred energy is used for reorientation and stretching. Energy storage in the stretched state and energy dissipation of VIFs upon stress relief has been addressed in the literature, reporting that in the filament, the energy is stored as potential energy in case monomers do not return to the α-helical state when relaxed.[31]

Furthermore, it can be hypothesized that, within a filament, it can be controlled whether reorientation or stretching dominates the mechanical response by varying the concentration of biotin monomers: the higher the biotin concentration, the higher the strains. However, an increase leads to saturation of the transmission strain, meaning stretching is more dominant than reorientation. Thus, it can be assumed that 5 wt% is already at the edge of saturation. (cf. Fig. 4.10, chapter 4.3.2) To prove the hypothesis, lower biotin concentrations need to be studied. If the hypothesis is correct, it is expected that the transfer strain decreases probably linearly with decreasing biotin concentration.

On the single filament level, BLOCK *et al.* identified three different regimes during straining[30]: (1) elastic stretching of α-helical domains at low strains below 10 % strain, (2) unfolding of α-helices to form β-sheets in the plateau-like regime above 10 % and (3) strain stiffening at high strain. With a maximum determined ϵ_{VIF} of 9.0 % on average, it can be assumed to be in regime (1) with a maximum at the transition between regime (1) and (2). In regime (1), the elastic stretching is provided by stretching of the hydrogen bonds in the α-helices, but they do not rupture. However, in regime (2), they begin to rupture in a sequential manner, starting from where the strain is applied.[207] For better comparison, the force f required for VIF stretching was calculated considering their strains (ϵ_{VIF}), which is given in Eq. 5.4.

$$f = \epsilon_{\mathrm{VIF}} \cdot A_0 \cdot E_{\mathrm{Y}} \tag{5.4}$$

Here, A_0 is the cross-sectional area of VIFs, which can be derived from $\pi \cdot (\frac{d}{2})^2$ with d being 10 nm (cf. Fig. 4.14 in chapter 4.4.1). A cross-sectional area was calculated as 78.5 nm^2. The YOUNG's modulus of VIFs (E_{Y}) was reported to be 27 MPa.[30]

Thus, the so-called force-strain curves were obtained when plotting the calculated force against the strains of VIFs (cf. Fig. 5.3), which demonstrates a linear dependency. This implies that the stretching of membrane-bound VIFs does not reach the plateau-like regime with a maximum force of 190 pN found for a 9 % strain at 750 μm · s^{-1}, which is significantly lower than the force reported by BLOCK *et al.* requisite to unfold α-helices with a stretching speed of 5 μm · s^{-1} (~350 pN[30]). The steep increase of the force at strains of around 1 % could mean that forces up to around 60 pN do not lead to any response from VIFs in the form of mechanical stretching. This could imply that at these forces, the strain of VIFs might be undetectable.

However, the broad strain distribution found in this study suggests that unfolding of α-helices (regime (2)) can occur, in particular, also because pinning points are present. If the filament segment is straight between two pinning points, the variety of strains observed for segments can contribute to the overall filament strain leading to the low strains found in this work when averaging.

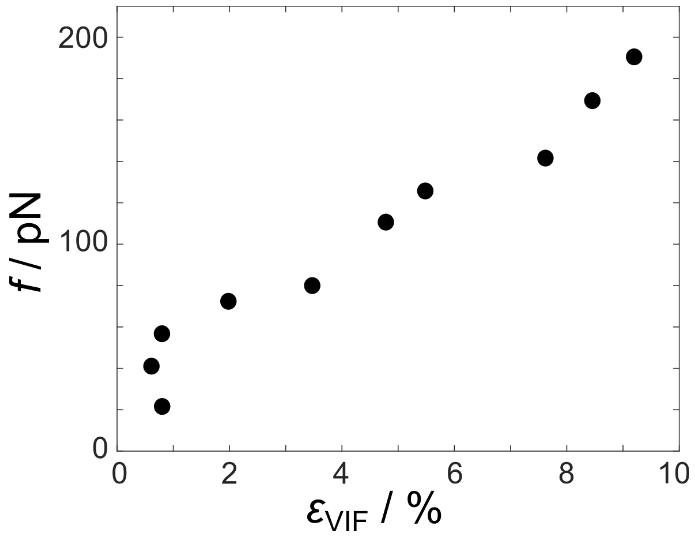

Fig. 5.3: Force-Strain curves of membrane-bound vimentin intermediate filaments (VIFs). Force f in pN is plotted against the average strain of membrane-bound VIFs (ϵ_{VIF}, $N = 86$), which shows a linear dependency, implying the VIFs being in the elastic regime. At low strains, the forces appear to be undetectable.

VINCENTE *et al.* applied a uniaxial stretching step of 30 % amplitude on VIFs attached to the PDMS using anti-vimentin antibodies, which increased the contour length of the filaments by ~18 % ($v = 500\ \mu\mathrm{m} \cdot \mathrm{s}^{-1}$).[206] The results obtained in this study at a stretching speed of $v = 750\ \mu\mathrm{m} \cdot \mathrm{s}^{-1}$ are significantly lower (5.2 %) at 30 % amplitude, which correspond to $\epsilon_{\mathrm{beads}} = 5.6$ % (cf. Fig. 4.8 C2, chapter 4.3.1). This shows that the mobile lipid bilayer with its partially sticky behavior on the PDMS support affects the transfer of the applied strain to the VIFs. Thus, the formed lipid bilayer is not completely sticky by employing the plasma settings (100 % O_2, 0.4 mbar, 20 %, 20 s). Sliding regions and defect formation would also absorb strain, which leads to further loss of transferred strain, resulting in lower strains on average. This effect of partially sticky membranes is also observed in cells as adhesion contacts.[162,166]

The change in ϵ_{VIF}, which is dependent on applied strain, is a function of the . The maximum ϵ_{VIF} of 9.0 % (on average) at $\epsilon_{\mathrm{beads}} = 9.6$ % was obtained at large ($v = 750\ \mu\mathrm{m} \cdot \mathrm{s}^{-1}$). The found dependency shows that at a lower strain rate, more thermal fluctuations (entropic stretching) by diffusive reorganization processes of lipids are present, as they can react to the applied strain. At higher rates, more strain is transferred. Thus mechanical stretching dominates since the diffusive reorganization of the lipids could be restricted on the one hand due to the sudden change[178] and on the other hand due to VIFs that respond to that by elongation of their contour lengths. This demonstrates clearly that the mobility of the lipid needs to be lower than strain velocity to observe the characteristic mechanical stretching of the VIFs. Otherwise, more entropic and less mechanical stretching will be monitored due to the larger reorganization of the lipids. If the is lower than the diffusion coefficient, no mechanical stretching is expected because diffusion of lipids superimposes the response of VIFs to external strain (cf. Fig. 5.4), as the VIFs are not stretched directly.

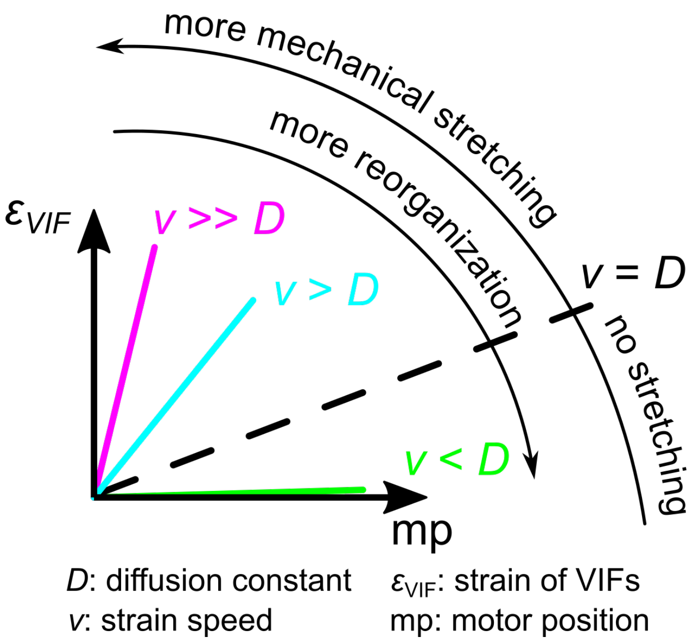
more mechanical stretching
more reorganization
ε_{VIF}
$v >> D$
$v > D$
$v = D$
no stretching
$v < D$
mp
D: diffusion constant
v: strain speed
ε_{VIF}: strain of VIFs
mp: motor position

Fig. 5.4: Reorientation of vimentin intermediate filaments (VIFs) by diffusive reorganization of lipids. To what degree reorganization of lipids has an impact on mechanical and entropic stretching of VIFs depends on the strain rate. At a higher stretching speed than the diffusion coefficient of the lipids, less reorganization of the lipids is observed, leading to mechanical stretching of VIFs being dominant. If the stretching speed is lower than the diffusion coefficient, mechanical stretching of VIFs cannot be detected, as diffusive lipid reorganization allows increased reorientation of VIFs.

This stretching speed dependency can be described by the BELL model, which enables the calculation of the unfolding force in dependence of the pulling speed (v, cf. Eq. 5.5).[207]

$$f(v) = \frac{k_B \cdot T}{x_b} \cdot \ln v - \frac{k_B \cdot T}{x_b} \cdot \ln v_0 \tag{5.5}$$

Here, f is the applied force, k_B the BOLTZMANN constant, T the temperature, v_0 the bond breaking speed if no strain is applied, and x_b is the distance between the equilibrium and transition state of breaking events. Eq. 5.5 states that the unfolding force increases logarithmically with the strain rate, *i.e.*, the strain velocity increases the probability of breaking hydrogen bonds in a filament.[207]

ACKBAROW *et al.* studied the pulling rate dependency of coiled-coil α-helices of VIFs by computational modelling using the above-mentioned equation (cf. Eq. 5.5). Applying increasing stretching speeds in the $m \cdot s^{-1}$ range, they revealed that the unfolding of the helices (plateau-like regime) occurred at decreasing strains. At the same time, higher forces were needed to reach the plateau. Furthermore, they reported that for stretching speeds lower than $5\ m \cdot s^{-1}$, the regime changes were similar to the results found in experiments.[30,50,207] For example, BLOCK *et al.* have documented similar rate dependency of single VIFs in the significantly lower speed range ($\mu m \cdot s^{-1}$), however, stating that the strain, at which regime change to the plateau-like regime occurs does not vary much with different stretching speed. The maximum strain rate, which they studied, was $5\ \mu m \cdot s^{-1}$, showing a plateau-like regime above 10 %.[30] In this work, the applied strain rate was higher by a factor of 4 or even 150 ($20\ \mu m \cdot s^{-1}$ and $750\ \mu m \cdot s^{-1}$). However, the above-calculated force of approximately 190 pN for 9 % on average is too low to reach the regime where unfolding occurs, with respect to the stretching speed of $750\ \mu m \cdot s^{-1}$ (around 114 pN for $20\ \mu m \cdot s^{-1}$). With this, it can be speculated that, in this work, increasing the stretching speed by a factor $\sim$ 38 is not sufficient for the segment-wise unfolding of α-helices. However, the broad distribution with an average strain of 5.4 ± 7.1 % for low stretching speed and 9.0 ± 13.3 % for high stretching speed (cf. Fig 4.8 C1/C2) could suggest the contrary. The rate dependency explains the function of the VIFs as a "security belt".[30–32]: VIFs in cells are soft, easily deformable material whose mechanics are undetectable under slow deformation, while they stiffen under fast deformation, where other cytoskeletal components break.[24,33] This allows the cell to maintain its strength and shape.

Besides mechanical stretching, the VIFs reoriented in the direction of strain (cf. Fig. 4.13 in chapter 4.3.3). As VIFs are randomly oriented on the membrane surface, each segment experiences different strains leading to a favored orientation of the filaments in the stretch direction. Thus, the individual VIFs in the networks could contribute to the mechanical response to the here applied strain by reorientation and stretching of single VIFs in the networks, as the schematic drawing Fig. 5.5 summarizes. Reorientation of VIFs is not only mediated by thermal fluctuations but also by the underlying lipid bilayer, which plays a part in counteracting the applied strain with diffusive reorganization (cf. Fig. 5.5).

Summary: In the scope of this work, a longitudinal strain of 35 % was applied to study the mechanical response of membrane-bound VIFs and VIF networks to externally applied strain. Membrane-bound VIFs counteracted with mechanical and entropic stretching. To what extent which behavior dominates depends on the be-

havior of the underlying lipid bilayer, stretching speed, and pinning point density. Membrane-bound VIF networks reoriented when the strain was applied. Since no information about mechanical stretching could be obtained, it can be assumed that straightened VIFs within the networks could contribute to the mechanical response with stretching, which could be reduced or even undetectable at the current applied strain due to entanglement *via* permanent and transient cross-linkers.

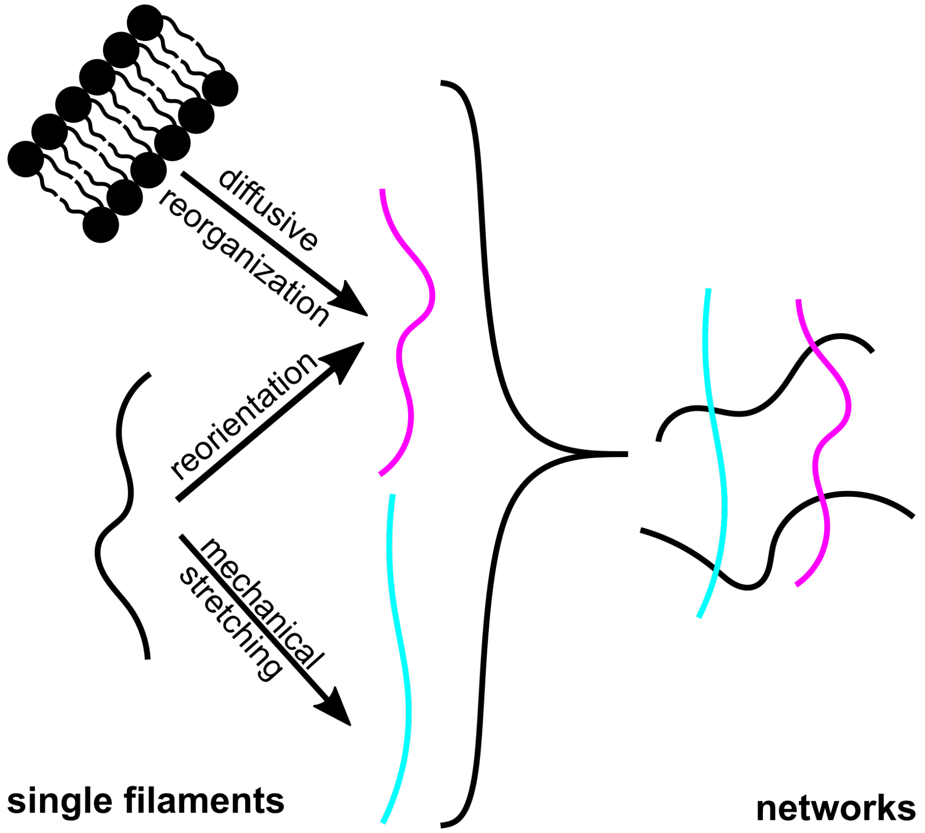

Fig. 5.5: Schematic drawing of the contribution of vimentin intermediate filaments (VIFs) to the mechanical response of VIF networks. Single filaments respond to external strain by reorientation and mechanical stretching, while the lipid bilayer beneath the VIFs contributes to their reorientation by diffusive reorganization. Mechanical stretching occurs when a filament or a segment is straightened. Individual membrane-bound VIFs could be involved in the mechanics of networks, especially at larger strains, by showing mechanical and entropic stretching, as mentioned above.

5.4 Comparison to IF Networks in Cells

In vitro experiments are performed to reduce the complexity found in cells and to unravel their properties in a minimal artificial system with the components needed. To better understand these findings, they need to be compared to the situation in cells. In literature, it has been reported that the strain of VIF networks in cells cannot be detected at low strain [30]. Compared to the model system used by *Vincent et al.*, who prepared VIFs on antibody-decorated PDMS and only detected minor strains (< 6 %) by applying 50 % strain amplitude [206], the model system established in this work consists of VIFs bound to the lipid bilayer on PDMS. Thus, it can be assumed that it might not be possible to observe mechanical stretching and thereby could only be detected at higher than the strain applied in this work. The applied strain can be regarded as a low strain regime because only a portion of 35 % is reached to the single or entangled VIFs. One main reason is the underlying membrane that absorbs some of the applied strain and thus, contributes to the mechanical response of the VIF networks, as the mechanical changes result in diffusive reorganization of the lipids in the bilayer to establish the mechanical equilibrium. The VIF network then absorbs the remaining strain through the resistance between the membrane fluidity and the anchor proteins. Even though single membrane-bound VIFs responded to 35 % of applied longitudinal strain by altering their contour lengths by around 9 % on average (cf. Fig. 4.8, chapter 4.3.1), it can be postulated that it can be different for VIF networks due to entanglement and cross-linking by specific and transient cross-links. This entanglement might reduce the strain absorbed by the VIF networks, which means that only minor strains could be observed when stretching the networks.

An overview of the findings within the scope of this work (cf. Fig. 5.6 A) and a comparison to the composition in a cell (cf. Fig. 5.6 B) can be seen in Fig. 5.6. In this work, a planar lipid bilayer with attached VIF networks was used. It was found that VIFs might contribute to the overall mechanical response of VIF networks by reorientation and stretching in the direction of the applied strain. However, the here applied strain could be too low to observe high straining and stiffening of the networks due to entanglement. However, it can be speculated that at the given strains, VIF networks, *i.e.*, VIFs within the networks, might support the underlying bilayer by reorientation, resulting in a different defect shape compared to the defect shapes in the lipid bilayer that is not associated with VIFs. The shape of the defect of lipid bilayers under strain is well-defined "eye-shaped" (cf. Tab. 1.2, chapter 4.2.1), while the defects in the bilayers if VIFs were attached appear as an ellipse with a shorter semi-minor axis (y-axis) and larger semi-major axis in x-direction (cf. Fig. 4.16, chapter 4.5). Therefore, they function as a “stress absorber” that would protect the lipid bilayer from rupturing at higher strains, as its physical state and structural integrity are crucial for the survival of the cell. In comparison, plasma membranes in a cell are a ruffled 3D surface capable of forming a planar membrane upon stretching. Therefore, they can be expanded 7-8 times, depending on the cell and membrane type [208–210], so that deformation would not result in bilayer stretching. Thus, the "IF cortex" would experience significantly higher strains by unfolding the membrane, which the IFs can withstand by reorientation and stretching. Only if the membrane is completely unfolded the membrane gets stretched and ruptured, which might lead to IF strain stiffening. Nothing but the strain stiffened IF networks would protect the plasma membrane from further rupture. If strains are reached that IFs cannot resist anymore, it will cause cell death.

The reorientation of VIFs within the networks found in this work is also consistent with the directional alignment of cytoskeletal components in cell upon cell stretching. Several groups studied the reorientation of cytoskeletal components in cells by applying cyclic uniaxial stretch. [211–215] Generally, it was found that all cytoskeletal filament classes reorient perpendicular to the direction of stretch. For VIFs, it was found that the perpendicular reorientation is less pronounced than for actin filaments (AF) and microtubules (MT). This shows that AT and MTs tend to reorient in the direction of least strain compared to IFs, which additionally aligns parallel to the stretching direction. This can be due to the fact that AF and MT tend to break at rather low strains, and to avoid this, they do not realign in the direction of stretch. Furthermore, cyclic uniaxial stretching leads to adaptation to the repetitively applied relatively low strains. The perpendicular orientation of VIFs in cells found by performing cyclic uniaxial cell stretching does not agree well with the parallel alignment of VIFs upon uniaxial stretching obtained in this work. This demonstrates two different behaviors depending on the type of mechanical strain. Cyclic stretching can be associated with cells in the lungs and blood vessels experiencing iterative expansion and relaxation cycles. Non-cyclic stretching correlates with cells involved in mitosis and migration [199,201], and all cells exposed to one-off external mechanical load. Parallel alignment of VIFs in migrating cells has been reported. Thus, based on the findings in the literature and in this work, it can be suggested that VIFs in cells that are subjected to large external mechanical forces reorient in such a way that they can support and protect the cell from damage. In contrast, the other subsystems would align perpendicular for support in that direction. This is due to the notable extensibility of VIFs compared to AF and MT.

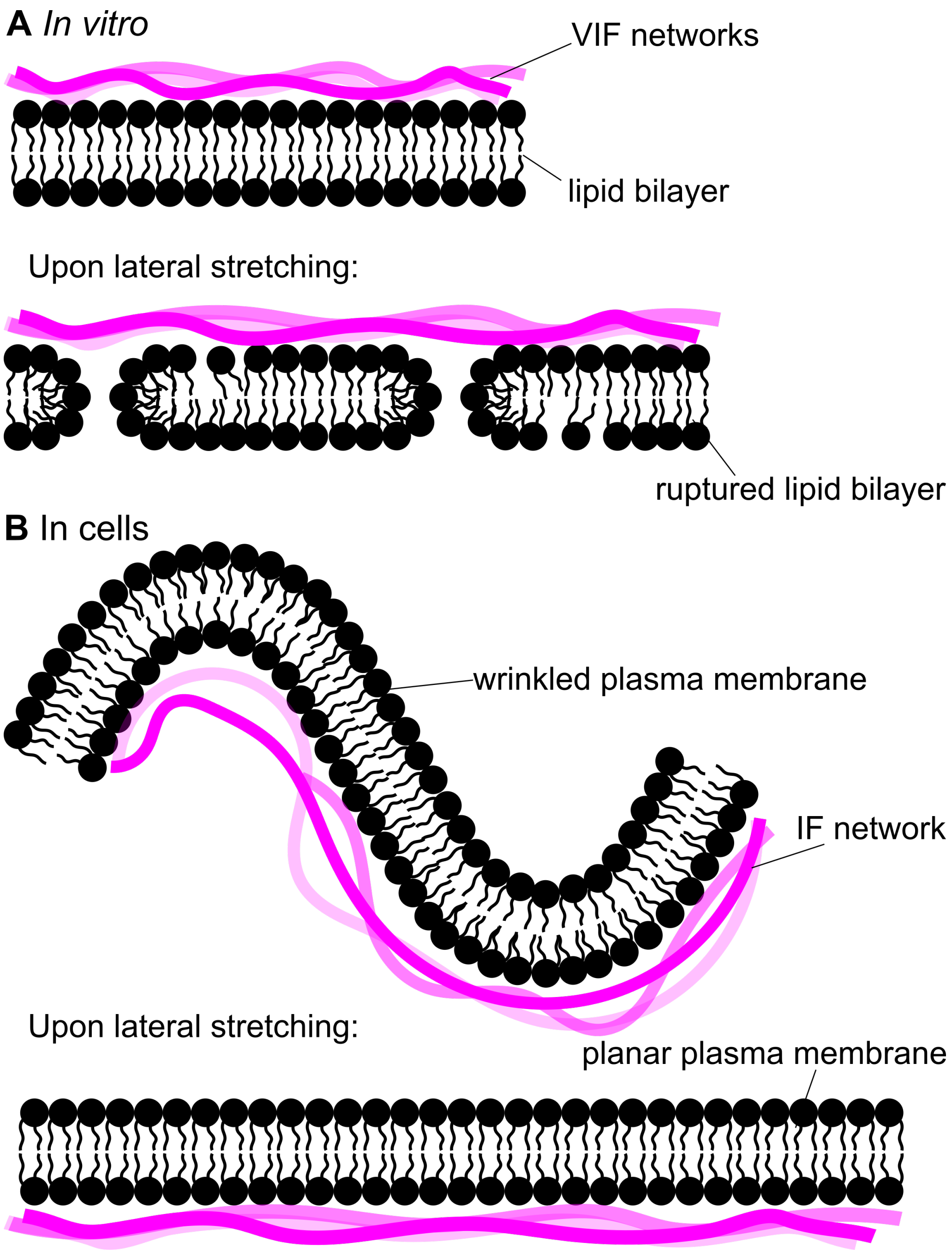
A *In vitro*
VIF networks
lipid bilayer
Upon lateral stretching:
ruptured lipid bilayer
B In cells
wrinkled plasma membrane
IF network
Upon lateral stretching:
planar plasma membrane

Fig. 5.6: Membrane-bound vimentin intermediate filament (VIF) networks under strain. VIFs and the membrane are represented in magenta and black, respectively. (**A**) In this work, it was found that the networks might support the underlying planar lipid bilayer by reorientation, which, however, ruptures due to a lack of lipid reservoir. As the VIF network shields the membrane, it cannot be provided with sufficient excess lipid material. Still, the shape of the defects serves as an indicator for VIFs supporting the lipid bilayer. (**B**) In cells, the plasma membrane is wrinkled and folded. Thus, it possesses sufficient excess membrane area to expand. The IF networks can withstand the expansion by reorientation and straining. Only if the membrane is unfolded does it experience stretching and rupturing, which would lead to strain stiffening and even rupturing of the IF network. This would imply cell death.

Summary: In the scope of this work, it can be assumed that the applied longitudinal strain of 35 % might not be sufficient enough to observe the straining of VIF networks still they support the underlying lipid bilayer by reorientation. The VIFs align parallel to the stretching direction to be able to support the underlying bilayer. Only strain-stiffened VIF networks would protect the lipid bilayer from further rupture. Therefore higher external strains would be required.

6 Summary and Outlook

Intermediate filaments (IFs) are characterized by their remarkable extensibility. Thus they are the primary determinant of cell architecture and mechanics, especially at large deformations. In particular, they do not only act as a mechanical regulator of the cytoplasm, but also contribute to the mechanical stability of the plasma membrane.

The goal of this work was to establish an *in vitro* model system, which is capable of mimicking the intracellular IFs directly at the plasma membrane and giving insights into their structural and mechanical alteration under strain. To achieve this, an artificial model system composed of vimentin intermediate filaments (VIFs) attached to a lipid bilayer *via* a non-physiological linker, namely neutravidin, was prepared on polydimethylsiloxane (PDMS), containing fluorescent beads. Its mechanical properties make PDMS suitable for stretching experiments due to its molecular flexibility, such as bendability and stretchability. By utilizing a uniaxial motor-driven stretching device, the PDMS-supported composite system in the presence of small unilamellar vesicles (SUVs) was laterally stretched and imaged by confocal laser scanning microscopy (CLSM) and atomic force microscopy (AFM). Before studying the composite system as a whole, the lipid bilayer on PDMS was characterized since several requirements had to be fulfilled: (1) stickiness of the PDMS surface and (2) expansion of lipid bilayer beyond an areal strain of 4-6 % without rupturing. The stickiness of the PDMS surface was achieved by using oxygen plasma, which rendered the surface hydrophilic with a thin, elastic oxide layer showing a certain degree of roughness. The found diffusion constant of the lipid bilayer of $1.4 \pm 0.2\ \mu\text{m}^2 \cdot \text{s}^{-1}$ clearly reflects the stickiness, which is even more reduced when strain is applied ($1.0 \pm 0.2\ \mu\text{m}^2 \cdot \text{s}^{-1}$). This shows diffusive reorganization of the lipids to counteract the applied strain, however, hindered by stretch-induced nanoscopic defects. Defect formation was significantly reduced by SUVs serving as a lipid reservoir, providing the lipid bilayer with excess membrane area, implying 35 % lateral strain (strain in stretching direction) applied in this work does not disturb its integrity. With a lipid bilayer in hand that does not rupture at strains of 4-6 %, structural and mechanical properties of VIFs and VIF networks attached to the bilayer were studied under strain. When an external strain of 35 % was applied, stretching of single membrane-bound VIFs revealed mechanical stretching (a strain of 9.0 % on average) and entropic stretching (reorientation towards stretching direction), while stretching of VIF networks mainly showed entropic stretching. This leads to the assumption that VIFs in the networks could also react with straining. However, the strains might be reduced as the VIFs were entangled due to permanent and transient cross-linkers. It cannot be raked out that the applied strain is not large enough due to strain losses. This notable loss of strain is a result of its transmission from PDMS to VIFs, while the partially sticky but mobile lipid bilayer plays an essential role. The lipid bilayer beneath the VIFs and VIF networks still formed certain defects because the VIFs shielded the bilayer preventing the SUVs from reaching the planar membrane. However, the VIF networks remained intact under these conditions, thus might provide support to the lipid bilayer by absorbing the shock of the applied strain, which is reflected in the different shapes of the formed defects with and without VIFs. This scenario would not occur in nature because of the enormous excess membrane area provided to resist large deformations. The results of this work clearly demonstrated that membrane-bound VIFs and VIF networks did respond to 35 % lateral strain after the lipid bilayer sensed and counteracted the applied strain by diffusive reorganization of lipids to maintain the mechanical equilibrium. The remaining strain was then absorbed by the VIF network supporting the underlying bilayer.

Overall, the established model system provides the foundation for further investigation of "VIF cortex". To better resemble the native system and increase the lipid reservoir, one possibility could be the usage of a PDMS chamber with pillars to imitate the wrinkled plasma membrane. Substitution of the solid supported membrane by pore-spanning membranes (PSMs) would allow for higher stretching. This is because PSMs consist of a solid supported part and a free-standing part, thus, higher strains by *e.g.*, osmotic pressure can be applied to the free-standing membrane without rupturing since lipids on the solid supported part are mobile and can serve as lipid reservoir by diffusion into the free-standing membrane. This artificial model system allows stepwise increasing the complexity towards the cell. The complex cell cortex could be imitated by binding the actin network to the lipid bilayer *via* biotin-neutravidin or $\mathrm{PIP_2}$/ezrin linkages. A minimal artificial model system with minimal actin filaments using $\mathrm{PIP_2}$/ezrin as linker system has been established in the working group of PROF. DR. CLAUDIA STEINEM (Institute for Organic and Biomolecular Chemistry, Georg-August University Göttingen). Making use of that and cross-linking the VIF network to the actin cortex through biotin-neutravidin linkages or physiological linker systems, such as plectin or ankyrin, further increases the complexity. The behavior under strain *in vitro* could be compared to the natural system for a better understanding of the cellular cytoskeletal cortex.

Bibliography

[1] D. H. Boal, S. Fraser, *Mechanics of the cell*, Cambridge University Press, Cambridge, **2002**.

[2] B. Alberts, A. Johnson, J. Lewis, *Molecular Biology of the Cell*, W. W. Norton & Company, New York, **2014**.

[3] K. Munk, C. Abröll, *Biochemie, Zellbiologie: [fit für den Bachelor]*, Thieme, Stuttgart, **2008**.

[4] A. Lehninger, M. Cox, D. Nelson, *Lehninger Principles of Biochemistry*, Springer, Berlin, **2009**.

[5] H. I. Ingolfsson, M. N. Melo, S. J. Marrink, Lipid Organization of the Plasma Membrane, *J. Am. Chem. Soc.* **2014**, *136*, 14554–14559.

[6] R. Winter, Struktur und Dynamik von Modell-Biomembranen, *Chem. Unserer Zeit* **1990**, *24*, 71–81.

[7] P. A. Janmey, P. K. J. Kinnunen, Biophysical Properties of Lipids and Dynamic Membranes, *Trends Cell Biol.* **2006**, *16*(10), 538–546.

[8] J. M. Berg, J. L. Tymoczko, L. Stryer, *Biochemie*, Spektrum Akad. Verl., Heidelberg, **2011**.

[9] F. de Meyer, B. Smith, Effect of Cholesterol on the Structure of a Phospholipid Bilayer, *Proc. Natl. Acad. Sci.* **2009**, *106*(10), 3654–3658.

[10] M. S. Bretscher, M. C. Raff, Mammalian Plasma Membranes, *Nature* **1975**, *258*, 43–49.

[11] S. J. Singer, G. L. Nicolson, The Fluid Mosaic Model of the Structure of Cell Membranes, *Science* **1972**, *175*, 720–731.

[12] G. Vereb, J. Szöllösi, S. Damjanovich, Dynamic, yet Structured: The Cell Membrane three Decades after the Singer–Nicolson Model, *Proc. Natl. Acad. Sci.* **2003**, *100*, 8053–8058.

[13] L. A. Bagatolli, O. G. Mouritsen, Is the Fluid Mosaic (and the Accompanying Raft Hypothesis) a Suitable Model to Describe Fundamental Features of Biological Membranes? What May be Missing?, *Font. Plant Sci.* **2013**, *4*(457), 1–6.

[14] G. L. Nicolson, G. F. de Mattos, A Brief Introduction to Some Aspects of the Fluid–Mosaic Model of Cell Membrane Structure and Its Importance in Membrane Lipid Replacement, *Membranes* **2021**, *11*(947), 1–19.

[15] H. J. Risselada, S. J. Marrink, The Molecular Face of Lipid Rafts in Model Membranes, *Proc. Natl. Acad. Sci.* **2008**, *105*(45), 17367–17372.

[16] B. Martinac, Y. A. Nikolaev, C. D. Cox, Cell Membrane Mechanics and Mechanosensory Transduction, *Curr. Top. Membr.* **2020**, *86*, 83–141.

[17] S. Fulda, A. M. Gorman, A. Samali, Cellular Stress Responses: Cell Survival and Cell Death, *Int. J. Cell Biol.* **2010**, *2010*, 1–23.

[18] B. D. Hoffman, J. C. Crocker, Cell Mechanics: Dissecting the Physical Responses of Cells to Force, *Annu. Rev. Biomed. Eng.* **2009**, *11*, 259–288.

[19] S. Huang, D. E. Ingber, The Structural and Mechanical Complexity of Cell-Growth Control, *Nat. Cell Biol.* **1999**, *1*, E131–E138.

[20] A. J. Kosmalska, L. Casares, P. Roca-Cusachs, Physical Principles of Membrane Remodelling during Cell Mechanoadaptation, *Nat. Commun.* **2015**, *6*(7292), 1–11.

[21] N. E. Vlahakis, M. A. Schroeder, R. D. Hubmayr, Role of Deformation-induced Lipid Trafficking in the Prevention of Plasma Membrane Stress Failure, *Am. J. Respir. Crit. Care Med.* **2002**, *166*, 1282–1289.

[22] J. Dai, M. P. Sheetz, Cell Membrane Mechanics, *Methods Cell Biol.* **1997**, *35*, 157–171.

[23] J. W. Valentine, A. G. Collins, C. P. Meyer, Morphological Complexity Increase in Metazoans, *Paleobiology* **1994**, *20*(2), 131–142.

[24] F. Huber, A. Boire, G. H. Koenderink, Cytoskeletal Crosstalk: when Three Different Personalities Team up, *Curr. Opin. Cell Biol.* **2015**, *32*, 39–47.

[25] D. A. Fletcher, R. D. Mullins, Cell Mechanics and the Cytoskeleton, *Nature* **2010**, *463*, 485–492.

[26] J. Block, V. Schroeder, S. Köster, Physical Properties of Cytoplasmic Intermediate Filaments, *Biochimica et Biophysica Acta* **2015**, *1853*(11 Part B), 3053–3064.

[27] S. A. Eldirany, I. B. Lomakin, C. G. Bunick, Recent Insight into Intermediate Filament Structure, *Cur. Opin. Cell Biol.* **2021**, *68*, 131–143.

[28] E. Latorre, S. Kale, X. Trepat, Active Superelasticity in Three-Dimensional Epithelia of Controlled Shape, *Nature* **2018**, *563*(7730), 203–208.

[29] H. Wu, Y. Shen, D. A. Weitz, Vimentin Intermediate Filaments and Filamentous Actin Form Unexpected Interpenetrating Networks That Redefine the Cell Cortex, *Proc. Natl. Acad. Sci.* **2022**, *119*(10), e2115217119.

[30] J. Block, H. Witt, S. Köster, Nonlinear Loading-Rate-Dependent Force Response of Individual Vimentin Intermediate Filaments to Applied Strain, *Phys. Rev. Lett.* **2017**, *118*(4), 048101(1)–048101(5).

[31] J. Block, H. Witt, S. Koester, Viscoelastic Properties of Vimentin Originate from Nonequilibrium Conformational Changes, *Sci. Adv.* **2018**, *4*, eaat1116(1)–eaat1116(10).

[32] K. T. Sapra, O. Medalia, Bend, Push, Stretch: Remarkable Structure and Mechanics of Single Intermediate Filaments and Meshworks, *Cells* **2021**, *10*(1960), 1–18.

[33] P. A. Janmey, U. Euteneuer, M. Schliwa, Viscoelastic Properties of Vimentin Compared with Other Filamentous Biopolymer Networks, *J. Cell Biol.* **1991**, *113*(1), 155–160.

[34] S. Koester, Y.-C. Lin, D. A. Weitz, Desmin and Vimentin Intermediate Filament Networks: Their Viscoelastic Properties Investigated by Mechanical Rheometry, *J. Mol. Biol.* **2009**, *388*, 133–143.

[35] P. Pawelzyk, H. Hermann, N. Willenbacher, Attractive Interactions among Intermediate Filaments Determine Network Mechanics In Vitro, *PLoS One* **2014**, *9*(4), e93194.

[36] A. Aufderhorst-Roberts, G. H. Koenderink, Stiffening and Inelastic Fluidization in Vimentin Intermediate Filament Networks, *Soft Matter* **2019**, *15*, 7127–7136.

[37] K. T. Sapra, O. Medalia, Nonlinear Mechanics of Lamin Filaments and the Meshwork Topology Build an Emergent Nuclear Lamina, *Nat. Commun.* **2020**, *11*(6205), 1–14.

[38] I. Szeverenyi, A. J. Cassidy, E. B. Lane, The Human Intermediate Filament Database: Comprehensive Information on a Gene Family Involved in Many Human Diseases, *Hum. Mutat.* **2008**, *29*(3), 351–360.

[39] R. A. Quinlan, N. Schwarz, R. E. Leube, A Rim-and-Spoke Hypothesis to Explain the Biomechanical Roles for Cytoplasmic Intermediate Filament Networks, *J. Cell Sci.* **2017**, *130*, 3437–3445.

[40] H. Hermann, S. V. Strelkov, U. Aebi, Intermediate Filaments: Primary Determinants of Cell Architecture and Plasticity, *J. Clin. Invest.* **2009**, *119*(7), 1772–1783.

[41] H. Herrmann, U. Aebi, Intermediate Filaments: Structure and Assembly, *Cold Spring Harb. Perspect. Biol.* **2016**, *8*, a018242(1)–a018242(22).

[42] P. M. Steinert, A. C. Steven, D. R. Roop, The Molecular Biology of Intermediate Filaments, *Nature* **1983**, *302*, 794–800.

[43] E. Fuchs, K. Weber, INTERMEDIATE FILAMENTS: Structure, Dynamics, Function, and Disease, *Annu. Rev. Biochem.* **1994**, *63*, 345–382.

[44] J. E. Erikkson, H.-M. Pallari, R. D. Goldman, Introducing Intermediate Filaments: from Discovery to Disease, *J. Clin. Invest.* **2009**, *119*(7), 1763–1771.

[45] E. Fuchs, D. W. Cleveland, A Structural Scaffolding of Intermediate Filaments in Health and Disease, *Science* **1998**, *279*, 514–519.

[46] N. Geisler, K. Weber, The Amino Acid Sequence of Chicken Muscle Desmin Provides a Common Structural Model for Intermediate Filament Proteins, *EMBO J.* **1982**, *1*, 1649–1656.

[47] P. M. Steinert, D. R. Roop, A. C. Steven, Complete Amino Acid Sequence of a Mouse Epidermal Keratin Subunit and Implications for the Structure of Intermediate Filaments, *Cell* **1985**, *42*, 411–419.

[48] S. V. Strelkov, H. Hermann, U. Aebi, Molecular Architecture of Intermediate Filaments, *BioEssays* **2003**, *25*, 243–251.

[49] H. Hermann, H. Bär, U. Aebi, Intermediate Filaments: from Cell Architecture to Nanomechanics, *Nature* **2007**, *8*, 562–573.

[50] H. Hermann, L. Kreplak, U. Aebi, Isolation, Characterization, and In Vitro Assembly of Intermediate Filaments, *Methods Cell Biol.* **2004**, *78*, 3–24.

[51] A. A. Chernyatina, D. Guzenko, S. V. Strelkov, Intermediate Filament Structure: the Bottom-up Approach, *Curr. Opin. Cell Biol.* **2015**, *32*, 65–72.

[52] R. A. Quinlan, M. Hatzfeld, W. W. Franke, Characterization of Dimer Subunits of Intermediate Filament Proteins, *J. Mol. Biol.* **1986**, *192*, 337–349.

[53] H. Herrmann, M. Häner, U. Aebi, Structure and Assembly Properties of the Intermediate Filament Protein Vimentin: The Role of its Head, Rod and Tail Domains, *J. Mol. Biol.* **1996**, *264*, 933–953.

[54] A. Aziz, J. F. Hess, P. G. FitzGerald, Site-Directed Spin Labeling and Electron Paramagnetic Resonance Determination of Vimentin Head Domain Structure, *J. Biol. Chem.* **2010**, *285*(20), 15278–15285.

[55] N. Muecke, T. Wedig, H. Hermann, Molecular and Biophysical Characterization of Assembly-Starter Units of Human Vimentin, *J. Mol. Biol.* **2004**, *340*, 97–114.

[56] R. Kirmse, S. Portet, J. Langowski, Characterization of Distinct Early Assembly Units of Different Intermediate Filament Proteins, *J. Mol. Biol.* **1999**, *286*(25), 18563–18572.

[57] S. Winheim, A. R. Hieb, N. Muecke, Deconstructing the Late Phase of Vimentin Assembly by Total Internal Reflection Fluorescence Microscopy (TIRFM), *PLoS One* **2011**, *6*(4), e19202.

[58] B. Noeding, H. Hermann, S. Koester, Direct Observation of Subunit Exchange along Mature Vimentin Intermediate Filaments, *Biophys. J.* **2014**, *107*, 2923–2931.

[59] D. Henderson, N. Geisler, K. Weber, A Periodic Ultrastructure in Intermediate Filaments, *J. Mol. Biol.* **1982**, *155*, 173–176.

[60] H. Hermann, M. Häner, U. Aebi, A Quantitative Kinetic Model for the in Vitro Assembly of Intermediate Filaments from Tetrameric Vimentin, *J. Mol. Biol.* **2007**, *282*, 1403–1420.

[61] M. S. Weber, M. Eibauer, O. Medalia, Structural Heterogeneity of Cellular K5/K14 Filaments as Revealed by Cryo-electron Microscopy, *eLife* **2021**, *10*, e70307.

[62] J. E. Eriksson, T. He, R. D. Goldman, Specific In Vivo Phosphorylation Sites Determine the Assembly Dynamics of Vimentin Intermediate Filaments, *J. Cell Sci.* **2004**, *117*, 919–932.

[63] N. Muecke, L. Kaemmerer, H. Hermann, Assembly Kinetics of Vimentin Tetramers to Unit-Length Filaments: A Stopped-Flow Study, *Biophys. J.* **2018**, *114*, 2408–2418.

[64] X. Zhou, Y. Lin, S. L. McKnight, Transiently Structured Head Domains Control Intermediate Filament Assembly, *Proc. Natl. Acad. Sci.* **2021**, *118*, e2022121118.

[65] H. Hermann, I. Hofmann, W. W. Franke, Identification of a Nonapeptide Motif in the Vimentin Head Domain Involved in Intermediate Filament Assembly, *J. Mol. Biol.* **1992**, *223*, 637–650.

[66] P. Traub, C. E. Vorgias, Involvement of the N-terminal Polypeptide of Vimentin in the Formation of Intermediate Filaments, *J. Cell Sci.* **1983**, *63*, 43–67.

[67] W. H. Goldmann, Intermediate Filaments and Cellular Mechanics, *Cell Biol. Int.* **2018**, *42*, 132–138.

[68] Z. Qin, L. Kreplak, M. J. Buehler, Hierarchical Structure Controls Nanomechanical Properties of Vimentin Intermediate Filaments, *PLoS One* **2009**, *4*(10), e7294.

[69] L. Kreplak, H. Baer, U. Aebi, Exploring the Mechanical Behavior of Single Intermediate Filaments, *J. Mol. Biol.* **2005**, *354*, 569–577.

[70] L. Kreplak, H. Hermann, U. Aebi, Tensile Properties of Single Desmin Intermediate Filaments, *Biophy. J.* **2008**, *94*, 2790–2799.

[71] J. Forsting, J. Kraxner, S. Koester, Vimentin Intermediate Filaments Undergo Irreversible Conformational Changes during Cyclic Loading, *Nano Lett.* **2019**, *19*, 7349–7356.

[72] Y. Gruenbaum, U. Aebi, Intermediate Filaments: a Dynamic Network that Controls Cell Mechanics, *F1000Prime Rep.* **2014**, *6*(54), 1–7.

[73] E. E. Charrier, P. A. Janmey, Mechanical Properties of Intermediate Filament Proteins, *Mol. Enzymol.* **2016**, *568*, 35–57.

[74] R. Sanghvi-Shah, G. F. Weber, Intermediate Filaments at the Junction of Mechanotransduction, Migration, and Development, *Front. Cell Dev. Biol.* **2017**, *5*(81), 1–19.

[75] G. Dutour-Provenzano, S. Etienne-Manneville, Intermediate Filaments, *Curr. Biol.* **2021**, *31*, R522–R529.

[76] S. Karsch, F. Buechau, A. Janshoff, An Intact Keratin Network is Crucial for Mechanical Integrity and Barrier Function in Keratinocyte Cell Sheets, *Cell. Mol. Life Sci.* **2020**, *77*, 4397–4411.

[77] A. E. Patterson, R. J. Carroll, P. A. Janmey, The vimentin Cytoskeleton: when Polymer Physics Meets Cell Biology, *Phys. Biol.* **2021**, *18*(011001), 1–16.

[78] F. Danielsson, M. K. Peterson, A. K. B. Gad, Vimentin Diversity in Health and Disease, *Cells* **2018**, *7*(147), 1–38.

[79] A. A. Chernyatina, H. Herrmann, S. V. Strelkov, Atomic Structure of the Vimentin Central α-helical Domain and its Implications for Intermediate Filament Assembly, *Proc. Natl. Acad. Sci.* **2012**, *109*(34), 13620–13625.

[80] A. Premchandar, N. Muecke, M. Dadlez, Structural Dynamics of the Vimentin Coiled-Coil Contact Regions Involved in Filament Assembly as Revealed by Hydrogendeuterium Exchange, *J. Biol. Chem.* **2016**, *291*(48), 24931–24950.

[81] S. V. Strelkov, H. Herrmann, P. Burkhard, Conserved Segments 1A and 2B of the Intermediate filament Dimer: their Atomic Structures and Role in filament Assembly, *EMBO J.* **2002**, *21*(6), 1255–1266.

[82] M. Meier, G. P. Padilla, P. Burkhard, Vimentin Coil 1A-A Molecular Switch Involved in the Initiation of Filament Elongation, *J. Biol. Chem.* **2009**, *390*, 245–261.

[83] A. V. Sokolova, L. Kreplak, S. V. Strelko, Monitoring Intermediate Filament Assembly by Small-Angle X-Ray Scattering Reveals the Molecular Architecture of Assembly Intermediates, *Proc. Natl. Acad. Sci.* **2006**, *103*(44), 16206–16211.

[84] P. M. Steinert, L. N. Marekov, D. A. D. Parry, Diversity of Intermediate Filament Structure. Evidence that the Alignment of Coiled-Coil Molecules in Vimentin is Different from that in Keratin Intermediate Filaments, *J. Biol. Chem.* **1993**, *268*(33), 24916–24925.

[85] H. Hermann, U. Aebi, Intermediate Filament Assembly: Fibrillogenesis is Driven by Decisive Dimer-Dimer Interactions, *Curr. Opin. Struc. Biol.* **1998**, *8*, 177–185.

[86] B. Eckes, D. Dogic, T. Krieg, Impaired Mechanical Stability, Migration and Contractile Capacity in Vimentin-Deficient Fibroblasts, *J. Cell Sci.* **1998**, *111*, 1897–1907.

[87] N. Wang, D. Stamenovic, Contribution of Intermediate Filaments to Cell Stiffness, Stiffening, and Growth, *Am. J. Physiol. Cell Physiolog.* **2000**, *279*, C188–C194.

[88] M. Guo, A. J. Ehrlicher, D. A. Weitz, The Role of Vimentin Intermediate Filaments in Cortical and Cytoplasmic Mechanics, *Biophy. J.* **2013**, *105*, 1562–1568.

[89] A. Vahabikashi, C. Y. Park, M. Johnson, Probe Sensitivity to Cortical versus Intracellular Cytoskeletal Network Stiffness, *Biophys. J.* **2019**, *116*, 518–529.

[90] A. E. Patterson, K. Pogoda, P. A. Janmey, Loss of Vimentin Enhances Cell Motility through Small Confining Spaces, *Small* **2019**, *15*, 903180(1)–903180(10).

[91] A. E. Patterson, A. Vahabikashi, P. A. Janmey, Mechanical and Non-Mechanical Functions of Filamentous and Non-Filamentous Vimentin, *BioEssays* **2020**, *42*, 2000078(1)–2000078(12).

[92] M. Ketema, M. Kreft, A. Sonnenberg, Nesprin-3 Connects Plectin and Vimentin to the Nuclear Envelope of sertoli Cells but Is not Required for sertoli Cell Function in Spermatogenesis, *Mol. Biol. Cell* **2013**, *24*, 2454–2466.

[93] C. M. Denais, R. M. Gilbert, J. Lammerding, Nuclear Envelope Rupture and Repair during Cancer Cell Migration, *Science* **2016**, *352*(6283), 353–358.

[94] A. E. Patterson, A. Vahabikashi, P. A. Janmey, Vimentin Protects Cells against Nuclear Rupture and DNA Damage during Migration, *J. Cell Biol.* **2019**, *118*(12), 4079–4092.

[95] J. Hu, Y. Li, M. Guo, High Stretchability, Strength, and Toughness of Living Cells Enabled by Hyperelastic Vimentin Intermediate Filaments, *Proc. Natl. Acad. Sci.* **2019**, *116*(35), 17175–17180.

[96] L. D. C. Stankevicins, M. Urbanska, F. Lautenschläger, Vimentin Provides the Mechanical Resilience Required for Amoeboid Migration and Protection of the Nucleus, *bioRXiv* **2019**.

[97] Y. Messica, A. Laser-Azogui, R. Beck, The Role of Vimentin in Regulating Cell Invasive Migration in Dense Cultures of Breast Carcinoma Cells, *Nano Lett.* **2017**, *17*, 6941–6948.

[98] N. Pinto, F.-C. Yang, D. S. Fudge, Self-Assembly Enhances the Strength of Fibers Made from Vimentin Intermediate Filament Proteins, *Biomacromolecules* **2014**, *15*, 574–581.

[99] F. Fleissner, S. Kumar, S. H. Parekh, Tension Causes Unfolding of Intracellular Vimentin Intermediate Filaments, *Adv. Biosyst.* **2020**, *4*, 2000111(1)–2000111(12).

[100] Z. Qin, L. Kreplak, M. J. Buehler, Nanomechanical Properties of Vimentin Intermediate Filament Dimers, *PLoS One* **2009**, *4*, e7249.

[101] C. Guzman, S. Jeney, L. Forro, Exploring the Mechanical Properties of Single Vimentin Intermediate Filaments by Atomic Force Microscopy, *J. Mol. Biol.* **2006**, *360*, 623–630.

[102] L. Kreplak, P. D. J. Doucet, F. Briki, New Aspects of the α-Helix to β-Sheet Transition in Stretched Hard α-Keratin Fibers, *Biophys. J.* **2004**, *87*(1), 640–647.

[103] S. Koester, Y.-C. Lin, D. A. Weitz, Nanomechanics of Vimentin Intermediate Filament Networks, *Soft Matter* **2010**, *6*, 1910–1914.

[104] Y.-C. Lin, C. P. Broedersz, D. A. Weitz, Divalent Cations Crosslink Vimentin Intermediate Filament Tail Domains to Regulate Network Mechanics, *J. Mol. Biol.* **2010**, *399*, 637–644.

[105] Y.-C. Lin, N. Y. Yao, D. A. Weitz, Origins of Elasticity in Intermediate Filament Networks, *Phys. Rev. Lett.* **2010**, *104*, 058101.

[106] H. Wu, Y. Shen, D. A. Weitz, Effect of Divalent Cations on the Structure and Mechanics of Vimentin Intermediate Filaments, *Biophys. J.* **2020**, *109*, 55–64.

[107] T. Golde, C. Huster, , J. Schnauß, Glassy Dynamics in Composite Biopolymer Networks, *Soft Matter* **2018**, *14*, 7970–7978.

[108] C. Dammann, B. Noeding, S. Koester, Vimentin Networks at Tunable Ion-Concentration in Microfluidic Drops, *Biomicrofluidics* **2012**, *6*, 022009(1)–022009(10).

[109] C. Dammann, S. Koester, Dynamics of Counterion-Induced Attraction between Vimentin Filaments Followed in Microfluidic Drops, *Lab Chip* **2014**, *14*, 2681–2687.

[110] C. Dammann, H. Hermann, S. Koester, Competitive Counterion Binding Regulates the Aggregation Onset of Vimentin Intermediate Filaments, *Isr. J. Chem* **2016**, *56*, 614–621.

[111] Z. Wu, K. Hjort, S. H. Jeong, Microfluidic Stretchable Radio-Frequency Devices, *Proceedings of the IEEE* **2015**, *103*(7), 1211–1225.

[112] Y. Xia, G. M. Whitesides, Soft Lithography, *Annu. Rev. Mater. Sci.* **1998**, *28*, 153–184.

[113] J. C. McDonald, D. C. Duffy, J. R. Anderson, Fabrication of Microfluidic Systems in Poly(dimethylsiloxane), *Electrophoresis* **2000**, *21*, 27–40.

[114] D. Ortiz-Acosta, C. Densmore, Sylgard Cure Inhibition Characterization, **2012**.

[115] A. J. Chalk, J. F. Harrod, Homogeneous Catalysis. II. The Mechanism of the Hydrosilation of Olefins Catalyzed by Group VIII Metal Complexes, *J. Am. Chem. Soc.* **1965**, *87*(1), 16–21.

[116] A. D. Delman, M. Landy, B. B. Simms, Photodecomposition of Polymethylsiloxane, *J. Polym. Sci. A Polym. Chem.* **1969**, *7*, 3375–3386.

[117] J. Roth, V. Albrecht, M. Nitschke, Surface Functionalization of Silicone Rubber for Permanent Adhesion Improvement, *Langmuir* **2008**, *24*, 12603–12611.

[118] J. F. E. Bodenschatz, K. Ajmail, A. Janshoff, Epithelial cells sacrifice excess area to preserve fluidity in response to external mechanical stress, *Commun. Biol.* **2022**, *5*(855), 1–11.

[119] J. Chen, X. Jiang, J. Wang, Theoretical and Experimental Investigation of Thermodynamics and Kinetics of Thiol-Michael Addition Reactions: A Case Study of Reversible Fluorescent Probes for Glutathione Imaging in Single Cells, *Org. Lett.* **2015**, *17*, 5978–5981.

[120] B. H. Northrop, S. H. Frayne, U. Choudhary, Thiol–Maleimide “Click” Chemistry: Evaluating the Influence of Solvent, Initiator, and Thiol on the Reaction Mechanism, Kinetics, and Selectivity, *Polym. Chem.* **2015**, *6*(18), 3415–3430.

[121] C. D. Caro, C. Haller, *UV/VIS Spectrophotometry - Fundamentals and Applications*, Mettler-Toledo AG, Analytical, Schwerzenbach, **2015**, 1–51.

[122] F. S. Rocha, A. J. Gomes, G. S. Patience, Experimental Methods in Chemical Engineering: Ultraviolet Visible Spectroscopy—UV-Vis, *Can. J. Chem. Eng.* **2018**, *96*, 2512–2517.

[123] F.-X. Schmid, *Biological Macromolecules: UV-visible Spectrophotometry*, Macmillan Publishers Ltd, Bayreuth, **2001**, 1–4.

[124] M. Grabolle, R. Brehm, U. Resch-Genger, Determination of the Labeling Density of Fluorophore-Biomolecule Conjugates with Absorption Spectroscopy, *Bioconjugate Chem.* **2012**, *23*, 287–292.

[125] Product Information: ATTO 647N, `https://www.atto-tec.com/fileadmin/user_upload/Katalog_Flyer_Support/ATTO_647N.pdf`, accessed 2022/01/18.

[126] R. H. Batchelor, A. Sarkez, I. Johnson, Fluorometric Assay for Quantitation of Biotin Covalently Attached to Proteins and Nucleic Acids, *BioTechniques* **2007**, *43*(4), 503–507.

[127] J. W. Lichtman, J.-A. Conchello, Fluorescence Microscopy, *Nat. Methods* **2005**, *2*(12), 910–919.

[128] M. Minsky, Microscopy Apparatus, U.S. Patent 3013467A, **Nov., 7, 1957**.

[129] J.-A. Conchello, J. W. Lichtman, Optical Sectioning Microscopy, *Nat. Methods* **2005**, *2*(12), 920–931.

[130] R. W. Cole, T. Jinadasa, C. M. Brown, Measuring and Interpreting Point Spread Functions to Determine Confocal Microscope Resolution and Ensure Quality Control, *Nat. Methods* **2011**, *6*(12), 1929–1941.

[131] The Airyscan Detector from ZEISS: Confocal Imaging with Improved Signal-to-Noise Ratio and Super-Resolution, `https://www.nature.com/articles/nmeth.f.388.pdf`, accessed 2022/01/24.

[132] K. Korobchevskaya, B. C. Lagerholm, M. Fritzsche, Exploring the Potential of Airyscan Microscopy for Live Cell Imaging, *Photonics* **2017**, *4*(41), 1–19.

[133] The Airyscan Detector from ZEISS: Confocal Imaging with Improved Signal-to-Noise Ratio and Superresolution, `https://www.gattaquant.com/files/en_wp_airyscan-detector.pdf`, accessed 2022/01/25.

[134] C. J. R. Sheppard, S. B. Mehta, R. Heintzmann, Superresolution by Image Scanning Microscopy Using Pixel Reassignment, *Photonics* **2013**, *38*(15), 2889–2892.

[135] L. Loren, J. Hagman, K. Braeckmans, Fluorescence Recovery after Photobleaching in Material and Life Sciences: Putting Theory into Practice, *Q. Rev. Biophys.* **2015**, *48*, 323–387.

[136] M. Kang, C. A. Day, E. DiBenedetto, Simplified Equation to Extract Diffusion Coefficients from Confocal FRAP Data, *Traffic* **2012**, *13*, 1589–1600.

[137] D. Axelrod, D. E. Koppel, W. W. Webb, Mobility Measurement by Analysis of Fluorescence Photobleaching Recovery Kinetics, *Biophys. J.* **1976**, *16*, 1055–1069.

[138] D. M. Soumpasis, Theoretical Analysis of Fluorescence Photobleaching Recovery Experiments, *Biophys. J.* **1983**, *41*, 95–97.

[139] G. Binning, C. F. Quate, C. Gerber, Atomic Force Microscope, *Phys. Rev. Lett.* **1986**, *56*(9), 930–933.

[140] Y. F. Dufrêne, T. Ando, D. J. Müller, Imaging Modes of Atomic Force Microscopy for Application in Molecular and Cell Biology, *Nat. Nanotechnol.* **2017**, *12*, 295–307.

[141] N. Jalili, K. Laxminarayana, A Review of Atomic Force Microscopy Imaging Systems: Application to Molecular Metrology and Biological Sciences, *Mechatronics* **2004**, *14*, 907–945.

[142] H.-J. Butt, B. Cappella, M. Kappl, Force Measurements with the Atomic Force Microscope: Technique, Interpretation and Applications, *Surf. Sci. Rep.* **2005**, *59*, 1–125.

[143] I. P. Mey, PhD thesis, Johannes Gutenberg-Universität Mainz, **2009**.

[144] J. L. Hutter, J. Bechhoefer, Calibration of Atomic-Force Microscope Tips, *Rev. Sci. Instrum.* **1993**, *64*(7), 1868–1873.

[145] J. E. Sader, J. W. M. Chon, P. Mulvaney, Calibration of Rectangular Atomic Force Microscope Cantilevers, *Rev. Sci. Instrum.* **1999**, *70*(10), 3967–3969.

[146] QI™ mode - Quantitative Imaging with the NanoWizard® 3 AFM, `https://www.jpk.com/app-technotes-img/AFM/pdf/jpk-tech-quantitative-imaging.14-1.pdf`, accessed 2022/02/04.

[147] H. Hertz, Ueber die Beruehrung Fester Elastischer Körper (On the Contact of Elastic Solids), *J. Reine Angew. Math.* **1881**, *92*, 156–171.

[148] AFM Probes, `https://www.brukerafmprobes.com/c-15-probes.aspx`, accessed 2022/02/06.

[149] C. Stringer, T. Wang, M. Pachitariu, Cellpose: a Generalist Algorithm for Cellular Segmentation, *Nat. Methods* **2021**, *18*(10), 100–106.

[150] M. Jerabek, Z. Major, R. Lang, Strain Determination of Polymeric Materials Using Digital Image Correlation, *Polym. Test.* **2010**, *29*(3), 407–416.

[151] H. Bruck, S. McNeill, W. PetersIII, Digital Image Correlation Using Newton–Raphson Method of Partial Differential Correction, *Exp. Mech.* **1989**, *29*, 261–267.

[152] A. D. Kammers, S. Daly, Small-Scale Patterning Methods for Digital Image Correlation under Scanning Electron Microscopy, *Meas. Sci. Technol.* **2011**, *22*, 125501(1)–125501(12).

[153] V. Rubino, N. Lapusta, J. Avouac, Static Laboratory Earthquake Measurements with the Digital Image Correlation Method, *Exp. Mech.* **2014**, 1–18.

[154] J. Blaber, B. Adair, A. Antoniou, Ncorr: Open-Source 2D Digital Image Correlation Matlab Software, *Exp. Mech.* **2015**, *55*, 1105–1122.

[155] B. Pan, A. Asundi, J. Gao, Digital Image Correlation Using Iterative Least Squares and Pointwise Least Squares for Displacement Field and Strain Field Measurements, *Opt. Lasers Eng.* **2009**, *47*(7), 865–874.

[156] G. Lamour, J. B. Kirkegaard, J. Gsponer, Easyworm: an Open-Source Software Tool to Determine the Mechanical Properties of Worm-like Chains, *Source Code Biol. Med.* **2014**, *9*(16), 1–6.

[157] J. M. Berg, J. L. Tymoczko, L. Stryer, *Stryer Biochemie*, Springer Spektrum, Berlin, Heidelberg, **2018**.

[158] A. Janshoff, C. Steinem, Mechanics of Lipid Bilayers: What do We Learn from Pore-Spanning Membranes?, *Biochim. Biophys. Acta* **2015**, *1853*, 2977–2983.

[159] M. D. Tomasini, C. Rinaldi, M. S. Tomassone, Molecular Dynamics Simulations of Rupture in Lipid Bilayers, *Exp. Biol. Med.* **2010**, *235*, 181–188.

[160] J. Gullingsrud, K. Schulten, Lipid Bilayer Pressure Profiles and Mechanosensitive Channel Gating, *Biophys. J.* **2004**, *86*, 3496–3509.

[161] L. Stubbington, M. Arroyo, M. Staykova, Sticking and Sliding of Lipid Bilayers on Deformable Substrates, *Soft Matter* **2016**, *13*, 181–186.

[162] M. Staykova, C. Read, H. A. Stone, Mechanics of Surface Area Regulation in Cells Examined with Confined Lipid Membranes, *Proc. Natl. Acad. Sci.* **2011**, *108*(22), 9084–9088.

[163] N. Schwarz, R. Windoffer, R. E. Leube, Dissection of Keratin Network Formation, Turnover and Reorganization in Living Murine Embryos, *Sci. Rep.* **2015**, *5*(9007), 1–8.

[164] L. Huang, P. S. Matthieu, B. P. Helmke, A Stretching Device for High-Resolution Live-Cell Imaging, *Ann. Biomed. Eng.* **2010**, *38*(5), 1728–1740.

[165] O. Aydin, B. Aksoy, B. E. Alaca, Time-Resolved Local Strain Tracking Microscopy for Cell Mechanics, *Rev. Sci. Instrum.* **2016**, *87*, 023905(1)–023905(10).

[166] F. Bianchi, J. H. George, H. Ye, Engineering a Uniaxial Substrate-Stretching Device for Simultaneous Electrophysiological Measurements and Imaging of Strained Peripheral Neurons, *Med. Eng. Phys.* **2019**, *67*, 1–10.

[167] O. Starkova, A. Aniskevich, Poisson's Ratio and the Incompressibility Relation for Various Strain Measures with the Example of a Silica-Filled SBR Rubber in Uniaxial Tension Tests, *Polym. Test.* **2010**, *29*, 310–318.

[168] Y. Morita, T. Sato, Y. Ju, The Optimal Mechanical Condition in Stem Cell-to-Tenocyte Differentiation Determined with the Homogeneous Strain Distributions and the Cellular Orientation Control, *Biol. Open* **2019**, *8*, bio039164.

[169] M. D. Mager, B. Almquist, N. A. Melosh, Formation and Characterization of Fluid Lipid Bilayers on Alumina, *Langmuir* **2008**, *24*, 12734–12737.

[170] Z. Peng, K. Shimba, T. Yagi, A Study of the Effects of Plasma Surface Treatment on Lipid Bilayers Self-Spreading on a Polydimethylsiloxane Substrate under Different Treatment Times, *Langmuir* **2021**, *XXXX*(XXX), XXX–XXX.

[171] N. Y. Adly, H. Hassani, B. Wolfrum, Observation of Chemically Protected Polydimethylsiloxane: towards Crack-Free PDMS, *Soft Matter* **2017**, *13*, 6297–6303.

[172] T. Ohishi, H. Noda, S. Deguchi, Tensile Strength of Oxygen Plasma-Created Surface Layer of PDMS, *J. Micromech. Microeng.* **2017**, *27*(015015), 1–9.

[173] D. Bodas, C. Khan-Malek, Hydrophilization and Hydrophobic Recovery of PDMS by Oxygen Plasma and Chemical Treatment—An SEM Investigation, *Sens. Actuators B* **2007**, *123*, 368–373.

[174] F. Blachon, F. Ha, J.-P. Rieu, Nanoroughness Strongly Impacts Lipid Mobility in Supported Membranes, *Langmuir* **2017**, *33*, 2444–2453.

[175] A. Filippov, G. Orädd, G. Lindblom, The Effect of Cholesterol on the Lateral Diffusion of Phospholipids in Oriented Bilayers, *Biophy. J.* **2003**, *84*, 3079–3086.

[176] N. Kahya, P. Schwille, How Phospholipid-Cholesterol Interactions Modulate Lipid Lateral Diffusion, as Revealed by Fluorescence Correlation Spectroscopy, *J. Fluoresc.* **2006**, *16*, 671–678.

[177] L. Guo, J. Y. Har, T. Wohland, Molecular Diffusion Measurement in Lipid Bilayers over Wide Concentration Ranges: A Comparative Study, *Chem. Phys. Chem.* **2008**, *9*, 721–728.

[178] J. T. Groves, Membrane Mechanics in Living Cells, *Dev. Cell* **2019**, *48*, 15–16.

[179] Z. Shi, Z. T. Graber, A. E. Cohen, Cell Membranes Resist Flow, *Cell* **2018**, *175*, 1769–1779.

[180] K. Jacobson, Y. Hou, D. Organisciak, Lipid lateral diffusion in the surface membrane of cells and in multibilayers formed from plasma membrane lipids, *Biochemistry* **1981**, *20*(18), 5268–5275.

[181] V. Roucoules, A. Ponche, J. Hemmerle, Changes in Silicon Elastomeric Surface Properties under Stretching Induced by Three Surface Treatments, *Langmuir* **2007**, *23*, 13136–13145.

[182] E. Evans, V. Heinrich, W. Rawicz, Dynamic Tension Spectroscopy and Strength of Biomembranes, *Biophys. J.* **2003**, *85*, 2342–2350.

[183] T. Shigematsu, K. Koshiyama, S. Wada, Effects of Stretching Speed on Mechanical Rupture of Phospholipid/Cholesterol Bilayers: Molecular Dynamics Simulation, *Sci. Rep.* **2015**, *5*(15369), 1–10.

[184] E. Mobaraka, M. Javanainena, I. Vattulainena, How to Minimize Dye-induced Perturbations while Studying Biomembrane Structure and Dynamics: PEG Linkers as a Rational Alternative, *Biochim. Biophys. Acta - Biomembr.* **2018**, *1860*, 2436–2445.

[185] G. Apodaca, Modulation of Membrane Traffic by Mechanical Stimuli, *Am. J. Physiol. Renal. Physiol.* **2002**, *282*, F179–F190.

[186] C. Morris, U. Homann, Cell Surface Area Regulation and Membrane Tension, *J. Membrane Biol.* **2001**, *179*, 79–102.

[187] J. L. Fisher, I. Levitan, S. S. Margulies, Plasma Membrane Surface Increases with Tonic Stretch of Alveolar Epithelial Cells, *Am. J. Respir. Cell Mol. Biol.* **2004**, *31*, 200–208.

[188] B. Li, G. Liu, W. Jia, Excretion and Folding of Plasmalemma Function to Accommodate Alterations in Guard Cell Volume during Stomatal Closure in Vicia Faba L., *J. Exp. Bot.* **2010**, *61*(13), 3749–3749.

[189] P. Sens, J. Plastino, Membrane Tension and Cytoskeleton Organization in Cell Motility, *J. Phys.: Condens. Matter* **2015**, *27*, 273103(1)–(13).

[190] H. Nöding, M. Schön, C. Steinem, Rheology of Membrane-Attached Minimal Actin Cortices, *J. Phys. Chem. B* **2018**, *122*, 4537–4545.

[191] M. Denz, H. Herrmann, S. Köster, Ion Type and Valency Differentially Drive Vimentin Tetramers into Intermediate Filaments or Higher Order Assemblies, *Soft Matter* **2021**, *17*, 870–878.

[192] A. V. Schepers, C. Lorenz, S. Köster, Multiscale Mechanics and Temporal Evolution of Vimentin Intermediate Filament Networks, *Proc. Natl. Acad. Sci.* **2021**, *118*(27), e2102026118.

[193] T. T. Nguyen, K. L. Sly, J. C. Conboy, Comparison of the Energetics of Avidin, Streptavidin, NeutrAvidin, and Anti-Biotin Antibody Binding to Biotinylated Lipid Bilayer Examined by Second-Harmonic Generation, *Anal. Chem.* **2012**, *84*, 201–208.

[194] N. Mücke, R. Kirmse, L. Kreplak, Investigation of the Morphology of Intermediate Filaments Adsorbed to Different Solid Supports, *J. Struct. Biol.* **2005**, *150*, 268–276.

[195] N. Muecke, L. Kreplak, J. Langowski, Assessing the Flexibility of Intermediate Filaments by Atomic Force Microscopy, *J. Mol. Biol.* **2004**, *335*, 1241–1250.

[196] C. Lorenz, J. Forsting, S. Köster, Lateral Subunit Coupling Determines Intermediate Filament Mechanics, *J. Struct. Biol.* **2019**, *123*(18), 188102(1)–188102(6).

[197] S. Ando, K. Nakao, Y. Oishi, Morphological Analysis of Glutaraldehyde-Fixed Vimentin Intermediate Filaments and assembly-Intermediates by Atomic Force Microscopy, *Biochim. Biophys. Acta* **2004**, *1702*, 53–65.

[198] T. T. Nguyen, K. L. Sly, J. C. Conboy, Intermediate Filament-Plasma Membrane Interactions, *Curr. Opin. Cell Biol.* **1991**, *3*, 127–132.

[199] S. Duarte, Álvaro Viedma-Poyatos, D. Pérez-Sala, Vimentin Filaments Interact with the Actin Cortex in Mitosis Allowing Normal Cell Division, *Nat. Commun.* **2019**, *10*(4200), 1–19.

[200] M. P. Serres, M. Samwer, E. K. Paluch, F-Actin Interactome Reveals Vimentin as a Key Regulator of Actin Organization and Cell Mechanics in Mitosis, *Dev. Cell* **2020**, *52*(5), 210–222.

[201] N. Costigliola, L. Dinga, G. Danuser, Vimentin Fibers Orient Traction Stress, *Proc. Natl. Acad. Sci.* **2017**, *114*(20), 5195–5200.

[202] Z. Gan, L. Ding, G. Danuser, Vimentin Intermediate Filaments Template Microtubule Networks to Enhance Persistence in Cell Polarity and Directed Migration, *Cell Syst.* **2016**, *3*, 252–263.

[203] A. Margiotta, C. Progida, C. Bucci, Rab7a Regulates Cell Migration through Rac1 and Vimentin, *Biochim. Biophys. Acta* **2017**, *1864*, 367–381.

[204] Y. Sakamoto, B. Boëda, S. Etienne-Manneville, APC Binds Intermediate Filaments and Is Required for Their Reorganization During Cell Migration, *J. Cell Biol.* **2013**, *200*(3), 249–258.

[205] J. R. Blundell, E. M. Terentjev, Stretching Semiflexible Filaments and Their Networks, *Macromolecules* **2009**, *42*, 5388–5394.

[206] F. N. Vicente, M. Lelek, C. Leduc, Molecular Organization and Mechanics of Single Vimentin Filaments Revealed by Super-Resolution Imaging, *Sci. Adv.* **2022**, *8*, eabm2696(1)–eabm2696(15).

[207] T. Ackbarow, M. J. Buehler, Superelasticity, Energy Dissipation and Strain Hardening of Vimentin Coiled-Coil Intermediate Filaments: Atomistic and Continuum Studies, *J. Mater. Sci.* **2007**, *42*, 8771–8787.

[208] D. Stamenovic, N. Wang, Stress Transmission within the Cell, *Compr. Physiol.* **2011**, *1*, 499–524.

[209] C. Butor, J. Davousi, Apical to Basolateral Surface Area Ratio and Polarity of MDCK Cells Grown on Different Supports, *Exp. Cell Res.* **1992**, *203*, 115–127.

[210] N. C. Gauthier, O. M. Rossier, M. P. Sheetz, Plasma Membrane Area Increases with Spread Area by Exocytosis of a GPI-anchored Protein Compartment, *Mol. Biol. Cell* **2009**, *20*, 3261–3372.

[211] J. Kang, R. L. Steward, K. M. Puskar, Response of an actin filament network model under cyclic stretching through a coarse grained Monte Carlo approach, *J. Theor. Biol.* **2011**, *274*, 109–119.

[212] A. Zielinski, C. Linnartz, B. Hoffmann, Reorientation dynamics and structural interdependencies of actin, microtubules and intermediate filaments upon cyclic stretch application, *Cytoskeleton* **2018**, *75*, 385–394.

[213] P. C. Dartsch, E. Betz, Response of cultured endothelial cells to mechanical stimulation, *Basic Res. Cardiol.* **1989**, *84*, 268–281.

[214] A. W. Holle, M. Kalafat, J. P. Spatz, Intermediate filament reorganization dynamically influences cancer cell alignment and migration, *Sci. Rep.* **2017**, *7*(45152), 1–14.

[215] M. Yoshigi, L. M. Hoffman, M. C. Beckerle, Mechanical force mobilizes zyxin from focal adhesions to actin filaments and regulates cytoskeletal reinforcement, *J. Cell Biol.* **2005**, *171*(2), 209–215.

A Appendix

A.1 Amino Acid Sequence of the Cysteine Mutant of Vimentin Monomer

The human vimentin mutant Vimentin C328NGGC was used in this work. The cystein at position 328 was replaced by an asparagine. At the *N*-terminal domain two glycines and a cysteine were added.

				CGG	
MSTRSVSSSS	YRRMFGGPGT	ASRPSSSPSY	VTTSTRTYSL	GSALRPSTSP	50
SLYASSPGGV	YATRSSAVRL	RSSVPGVRLL	QDSVDFSLAD	AINTEFKNTR	100
TNEKVELQEL	NDRFANYIDK	VRFLEQQNKI	LLAELEQLKG	QGKSRLGDLY	150
EEEMRELRRQ	VDQLTNDKAR	VEVERDNLAE	DIMRLREKLQ	EEMLQREEAE	200
NTLQSFRQDV	DNASLARLDL	ERKVESLQEE	IAFLKKLHEE	EIQELQAQIQ	250
EQHVQIDVDV	SKPDLTAALR	DVRQQYESVA	AKNLQEAEEW	YKSKFADLSE	300
AANRNNDALR	QAKQESTEYR	RQVQSLTNEV	DALKGTNESL	ERQMREMEEN	350
FAVEAANYQD	TIGRLQDEIQ	NMKEEMARHL	REYQDLLNVK	MALDIEIATY	400
RKLLEGEESR	ISLPLPNFSS	LNLRETNLDS	LPLVDTHSKR	TLLIKTVETR	450
DGQVINETSQ	HHDDLE				466

A.2 List of Symbols and Abbreviation

2D	two dimensional
3D	three dimensional
Å	Angstrom
A_0	cross-sectional area
A_{280}	absorbance, at wavelength 280 nm
$A_{\text{max, dye}}$	absorbance, fluorophore maximum
A_{vertical}	vertical deflection
aa	amino acids
AFM	atomic force microscopy
AFs	actin filaments
ATP	adenosine triphosphate
a.u.	arbitrary unit
AU	airy unit
AZS	angle of zero strain
C	cysteine
°C	degree Celcius
Cys SS	cysteine disulfide
c_{dye}	concentration, dye
c_{prot}	concentration, protein, at wavelength 280 nm
cf.	*conferre*
CLSM	confocal laser scanning microscopy
cm	centimeter
d	diameter
d (UV/vis)	optical path length
D	diffusion coefficient
D_{eff}	effective diffusion coefficient
D_{n}	nominal diffusion coefficient
D_{TS}	tip-sample distance
DIC	Digital image correlation
DMSO	dimethyl sulfoxide
DOL	degree of labeling
DOPE biotin cap	1,2-dioleoyl-*sn*-glycero-3-phosphoethanolamine-N-(biotinyl cap)
E	YOUNG's modulus
E_{Y}	YOUNG's modulus of VIFs

$E_{\text{ad.}}$	adhesion energy
$E_x x$	lateral Green-Langranian strain
$E_y y$	longitudinal Green-Langranian strain
ϵ	extinction coefficient
ϵ_{280}	extinction coefficient, at wavelength 280 nm
ϵ_{A}	strain according to Almansi
ϵ_{beads}	strain, beads
$\epsilon_{\text{beads},xx}$	longitudinal strain, beads
$\epsilon_{\text{beads},yy}$	lateral strain, beads
$\epsilon_{\text{bilayer, rupture}}$	rupture strain, bilayer
ϵ_{dye}	extinction coefficient, dye
ϵ_{GSV}	strain according to Green-Saint-Venant
$\epsilon_{\text{membrane}}$	strain, membrane
ϵ_{S}	strain according to Swaiger
$\epsilon_{\text{vesicle, rupture}}$	rupture strain, vesicle
ϵ_{VIF}	strain, Vimentin intermediate filaments
ϵ_{xx}, u	radius of unstretched circular PDMS
e.g.	*exempli gratia*
et al.	*et alia*
f (UV/vis)	correction factor
f	force
F_0	initial postbleach fluorescence intensity
F_∞	post-bleach steady state fluorescence intensity
F_{bk}	background fluorescence intensity
F_{fade}	photofading fluorescence intensity
F_{i}	pre-bleach fluorescence intensity
F_{raw}	raw fluorescence intensity
F_{corr}	corrected fluorescence intensity
FD	force distance
Fig.	figure
FRAP	fluorescence recovery after photobleaching
FWHM	full width at half maximum
G	glycine
g	gram
GaAsP-PMT	gallium arsenide phosphide photomultiplier
h	hour

HOMO	highest occupied molecular orbital
hs	high speed
I	intensity, light
i.e	*id est*
IFs	intermediate filaments
k_B	BOLTZMANN constant
k_C	spring constant
KCl	potassium chloride
kDa	Kilodalton
kHz	Kilohertz
l	length
L	liter
$L_\mathrm{Beads,0}$	initial distance between two beads
$L_\mathrm{Beads,i}$	distance between two beads at a certain motor position
L_ij	distance between two neighboring coordinates
L_C	contour length
L_C (AFM)	length of cantilever
L_P	persistence length
L_Seg	segment length
ls	low speed
LUMO	lowest unoccupied molecular orbital
M	molar
m	slope
m	meter
µL	microliter
µm	micrometer
mbar	milibar
mg	miligram
mL	mililiter
mm	milimeter
MAC	minimal actin cortex
mM	milimolar
min	minutes
MLV	multilamellar vesicles
mol	mole
mol%	mole percentage

mp	motor position
mp_{max}	maximal motor position
MPa	Megapascal
ms	miliseconds
MSD	mean squared displacement
MTs	microtubules
MW	molecular weight, molecular weight marker
MWCO	molecular weight cut-off
N (amino acid)	asparagine
N (unit)	Newton
N	number
n	refractive index
n/n	amount of substance per amount of substance
NA	numerical aperture
NCC	normalized cross-correlation
nN	nano Newton
nm	nanometer
PB A	Phosphate Buffer Solution A
PB B	Phosphate Buffer Solution B
PDMS	polydimethylsiloxane
%	percentage
pH	potential of hydrogen
PMT	photomultiplier
pN	pico Newton
PSF	point spread function
POPC	1-palmitoyl-2-oleoyl-*sn*-glycero-3-phosphocholine
Pt	platinum
px	pixel
Q	quality factor
QI	quantitative imaging
R_{mob}	mobile fraction
r_{eff}	effective radius
r_{n}	nominal radius
ρ_{f} (AFM)	density of the medium
ROI	region of interest
rpm	revolutions per minute

RT	room temperature
s (unit)	seconds
s	stretched
Si	silicon
SNR	signal to noise ratio
STED	Stimulated Emission Depletion
SUV	small unilamallar vesicles
T	temperature
t	time
t_C (AFM)	thickness of cantilever
Tab.	table
$\tau_{1/2}$	half-life of recovery
θ	angle between two segments
TIRF	total internal refelction fluorescence
Trp	tryptophan
Tyr	tyrosine
u (displacement)	horizontal displacement
u	unstretched
ULFs	unit-length filaments
UV	ultraviolet
V	Volt
v (displacement)	vertical displacement
v	strain speed
v_0	bond breaking speed without applied strain
vis	visible
VIF	Vimentin intermediate filaments
WAXS	wide-angle x-ray scattering
w_C (AFM)	width of cantilever
ω_0 (AFM)	resonance frequency
w/w	weight per weight
wt%	weight percentage
x_b	distance between equilibrium and transition state of breaking events
λ	wavelength
λ_abs	absorption wavelength
λ_em	emission wavelength
λ_ex	excitation wavelength

$\lambda_{\mathrm{biotin}}$	absorption wavelength biotin
λ_{dye}	absorption wavelength dye
$\lambda_{\mathrm{protein}}$	absorption wavelength protein
Z_{C}	deflection of cantilever

A.3 List of Chemicals and Consumables

ATTO647N-Maleimide	Atto-tec (Siegen, Germany)
ATTO488-DOPE	Atto-tec (Siegen, Germany)
ATTO647-DOPE	Atto-tec (Siegen, Germany)
BioGel P-30 media	Bio-Rad Laboratories (Hercules, USA)
Biotin Maleimide	
DOPE biotin cap	Avanti Polar Lipids (Alabaster, USA)
Chloroform	Merck (Darmstadt, Germany)
DMSO	Fisher Scientific UK (Loughborough, UK)
glass slides	
Glycerin	Grüssing GmbH (Filsum, Germany)
isopropanol	Merck (Darmstadt, Germany)
KCl	Fisher Scientific GmbH (Schwerte, Germany)
L-cysteine	
MSNL-10 cantilever	Bruker AFM Probes, Camarillo, USA
Mucasol®	Merck (Darmstadt, Germany)
Na_2HPO_4	Carl Roth (Karlsruhe, Germany)
NaH_2PO_4	Merck (Darmstadt, Germany)
NeutrAvidin	Thermo Fisher Scientific (Waltham, USA)
NeutrAvidin-Dylight405	
nitrogen	Air Liquide Deutschland GmbH (Düsseldorf, Germany)
oxygen	Air Liquide Deutschland GmbH (Düsseldorf, Germany)
PD midi Trap G.25	GE Healthcare Bio-Sciences AB (Uppsala, Sweden)
PDMS	Farnell GmbH (Oberhaching, Germany)
POPC	Avanti Polar Lipids (Alabaster, USA)
Psi B4.0 (beads)	AttendBio Research (Barcelona, Spain)
silicon wafer	Active Business Company GmbH (Brunnthal, Germany)
Urea	Merck KGaA (Darmstadt, Germany)

A.4 List of Devices and Softwares

AFM

Nanowizard 3 & 4 Ultra Seed	JPK Instruments (Berlin, Germany)

CLSM

LSM 880 Examiner	Carl Zeiss Microscopy GmbH (Oberkochen, Germany)
40X A Plan Apochromat, NA 1.0	Carl Zeiss Microscopy GmbH (Oberkochen, Germany)

PDMS preparation

SpinCoater	Specialty Coating Systems (Indianapolis, USA)
Ultrasonic bath	Elma Schmidbauer GmbH (Singen, Germany)

Protein

Nanodrop 2000c	Thermo Fisher Scientfic (Waltham, USA)
ThermoMix Compact	Eppendorf AG (Hamburg, Germany)

Preparation of vesicles

Tip sonifier Sonoplus HD2070	Bandelin (Berlin, Germany)

Stretching Device

PI Motor	Physik Instrumente GmbH & Co. KG (Karlsruhe, Germany)
PI Motor Controller	Physik Instrumente GmbH & Co. KG (Karlsruhe, Germany)

Surface coating

Zepto plasma cleaner	Diener Electronics (Ebbhausen, Germany)

Miscelanous

pH meter Calimatic 766	Knick (Berlin, Germany)
Ultrapure Water System, MilliQ Gradient A10	Merck Millipore (Darmstadt, Germany)
Vacuum drying oven VD23	Binder GmbH (Tuttlingen, Germany)

Software

ChemBioDraw Ultra	PerkinElmer (Watham, USA)
Fiji	https://fiji.sc/
Gwyddion 2.45	http://gwyddion.net
ImageJ 1.52t	http://imagej.nih.gov/ij
JPK Data Processing	Instruments AG (Berlin, Germany)
Matlab R2017b	Math Works (Natick, USA)
OriginPro 2020	OriginLAb Coorperation (Northhampton, USA)
PI Motion/Positionung	CD C-663.CD1 V3.0.0.0 (Karlsruhe, Germany)
Python™	http://www.python.org
Zen 2.3	Carl Zeiss Microscopy GmbH (Oberkochen, Germany)